Site C0011[1]

Expedition 333 Scientists[2]

Chapter contents

Background and objectives

Integrated Ocean Drilling Program (IODP) Expeditions 322 and 333 were designed to document characteristics of incoming sedimentary strata and uppermost igneous basement prior to their arrival at the subduction front (Saito, Underwood, Kubo, and the Expedition 322 Scientists, 2010). To accomplish those objectives, coring was conducted at two sites on the subducting Philippine Sea plate. IODP Site C0011 is located on the northwest flank of a prominent bathymetric high (the Kashinosaki Knoll) (Ike et al., 2008), whereas IODP Site C0012 is located near the crest of the knoll (Fig. F1). Data acquired during Expedition 322 and logging-while-drilling (LWD) data at Site C0011 acquired during IODP Expedition 319 provide information on presubduction equivalents of the seismogenic zone (Underwood et al., 2010). Core samples at Site C0011 were obtained by rotary core barrel (RCB) drilling from 340 to 876 meters below seafloor (mbsf), where the hole was abandoned because of drill bit failure. Merging lithofacies and age-depth models shows how correlative units change from an expanded section at Site C0011 to a condensed section at Site C0012 (Fig. F2). Geochemical analyses of interstitial water at Site C0011, where chlorinity decreases with depth, suggested an effect of focused flow and/or in situ dehydration reactions associated with rapid burial beneath the trench wedge and frontal accretionary prism. By contrast, Site C0012 displayed increasing chlorinity with depth and evidence of upward diffusion of sulfate and other dissolved chemical species from the basement (Underwood et al., 2010). Site C0012 is thought to represent a geochemical reference site unaffected by subduction processes.

The specific questions addressed by additional drilling at Site C0011 are

- Is fluid circulation in basement and permeable sedimentary layers influencing heat flow and diagenesis at Sites C0011 and C0012?
- How does contrasting interstitial fluid chemistry at Sites C0011 and C0012 relate with in situ diagenesis and fluid flow?
- Can a change of physical properties between 200 and 250 mbsf at Site C0011 be related to lithologic variation or silica diagenesis?

The main objectives for returning to Site C0011 were to perform temperature measurements for heat flow determination and ex-

[1] Expedition 333 Scientists, 2012. Site C0011. *In* Henry, P., Kanamatsu, T., Moe, K., and the Expedition 333 Scientists, *Proc. IODP,* 333: Tokyo (Integrated Ocean Drilling Program Management International, Inc.). doi:10.2204/iodp.proc.333.104.2012
[2] **Expedition 333 Scientists' addresses.**

doi:10.2204/iodp.proc.333.104.2012

pand the age-depth models into the Pliocene and Quaternary. This was necessary because the upper stratigraphic intervals of the Shikoku Basin were not adequately sampled during Expedition 322. Additional coring provided complete profiles of organic and interstitial water geochemistry and sampled across prominent discontinuities in physical properties identified from LWD data (Saito, Underwood, Kubo, and the Expedition 322 Scientists, 2010).

Operations

Transponders were retrieved from 0600 to 1530 h on 17 December 2010. The D/V *Chikyu* then moved to the first transponder location at Site C0011 over a 22 nmi distance at an average speed of 5.5 kt. The ship began setting transponders at 1930 h and finished at 0700 h on 18 December.

The hydraulic piston coring system (HPCS)/extended punch coring system (EPCS)/extended shoe coring system (ESCS) coring assembly was made up, run into Hole C0011C, and tagged the seafloor at 1700 h; coring began at 1800 h on 18 December. After oil leakage from the HPCS was found, the decision was made to pull out to 13 m above the seafloor, and coring in Hole C0011C ended at 22.5 mbsf (Table **T1**). From 0015 h on 19 December, the bottom-hole assembly was jetted in Hole C0011D to 6 mbsf and drilled to 21 mbsf before starting HPCS coring again at 0245 h. Coring continued to 184.5 m drilling depth below seafloor (DSF) where the decision was made to switch to EPCS because of continuous partial penetrations.

EPCS coring did not bring good quality and recovery of cores, and we switched to the ESCS after three cores at 1200 h on 21 December. After reaching 380 mbsf, which is 30 m deeper than the target depth, coring was stopped at 0900 h on 24 December, and we spotted kill mud and displaced the same with seawater before pulling out. The core bit and all of the assembly were on rig floor at 2000 h.

Coring operations were smooth except for oil leakage from the HPCS, which forced us to end Hole C0011C at a very shallow depth. Core recovery was good with an overall average of 101.7% in Hole C0011C and 102.2% in Hole C0011D. HPCS cores were the best of the three core types in terms of both recovery and quality, with an average recovery of 102.4%, ranging from 117.3% to 82.8%. EPCS did not get good core recovery, ranging from 77.2% to 38.6%. ESCS cores were good in recovery with an average of 103.3%, ranging from 158.6% to 9.3%, and remarkably good cores with mild biscuiting (length of coherent pieces >10 cm) were obtained in the weakly cemented tuffaceous sandstone (e.g., Cores 333-C0011D-48X and 51X), an improvement over Expedition 322 RCB coring. The core liner was broken twice and core jammed once.

Lithology

In Hole C0011B, five lithologic units were identified during Expedition 322 on the basis of sediment composition, sediment texture, and sedimentary structures (see fig. F2 and table T3 in Expedition 322 Scientists, 2010).

Lithologic Unit I was not cored during Expedition 322 (see Expedition 322 Scientists, 2010); however, based on LWD (Hole C0011A) and core-log-seismic integration, Unit I was assigned to cover the interval from 0 to 340 mbsf (see fig. F2 and table T3 in Expedition 322 Scientists, 2010) and has an estimated age of Holocene to late Miocene (Expedition 322 Scientists, 2010).

Lithologic Unit I and the uppermost part of Unit II was the drilling target for Expedition 333. A total of 380 m of strata was drilled in Holes C0011C and C0011D. The cored succession recovered sediments belonging to Unit I and the upper part of Unit II with very good recovery (Fig. **F3;** Table **T2**). The new coring also rectified the low recovery rates achieved when drilling the upper part of Unit II during Expedition 322 (Expedition 322 Scientists, 2010). Two lithologic subunits were interpreted within Unit I during the examination of cores.

Cored lithologies in Holes C00011C and C0011D include silty clay, clayey silt, and clay interbedded with volcanic ash (Figs. **F3, F4**). Below 347.82 mbsf the observed lithologies shift abruptly into coarse-grained tuffaceous sandstone and heterolithic gravel and sand. The uppermost sandstone bed represents the top of Unit II. The silty clay, clayey silt, and clay consist mainly of clay minerals with quartz, feldspar, abundant calcareous nannofossils, and some diatoms. *Discoaster* sp. is common below 130 mbsf. Sponge spicules, radiolarians, and silicoflagellates are relatively rare and are nearly absent in the 243.7–349 mbsf interval (see Site C0011 smear slides in **"Core descriptions"**). Opaque minerals are generally rare (see Site C0011 smear slides in **"Core descriptions"**). However, biotite, orthopyroxene, and hornblende are common below 250 m (see Site C0011 smear slides in **"Core descriptions"**).

A likely equivalent to the onland Azuki volcanic ash bed (0.85 Ma; Hayashida et al., 1996) occurs at 21.18 mbsf (Section 333-C011C-3H-10, 10–27 cm), and a probable correlative to the onland Pink volcanic ash bed (1.05 Ma; Hayashida et al., 1996) occurs at 31.30 mbsf (Section 333-C0011D-2H-1, 84–86 cm). Both

events are tentatively recognized in the cores from Holes C0011C and C0011D as thin discrete accumulations of ash and by characteristic microscopic features in smear slides, which are distinct from all other ash layers. The Azuki volcanic ash is composed of abundant bubble wall type glass shards with a few obsidian fragments and orthopyroxene and clinopyroxene crystals. The Pink volcanic ash contains fibrous bubble wall type glass shards and abundant hornblende minerals. In addition, a probable correlative to the onland Ohta volcanic ash bed (4.0 Ma; Satoguchi et al., 2005) is present in Core 333-C0011D-17H-9, 2–5 cm, at 157.26 mbsf (Fig. F3), and a possible match to the Habutaki I volcanic ash bed (2.8–2.9 Ma; Nagahashi and Satoguchi, 2007) is located at 80.56 mbsf (Section 333-C0011D-8H-2, 80 cm, through 8H-CC, 8.5 cm). This interpreted correlation is based on positive identification of characteristic microscopic features for these volcanic ashes in smear slides: the Ohta volcanic ash is characterized by bubble junction type glass shards and biotite; the Habutaki I volcanic ash is characterized by bubble wall type glass shards and beta quartz.

Lithologic Unit I (hemipelagic/pyroclastic facies)

Interval: Sections 333-C0011C/C0011D-1H-1, 0.0 cm, through 333-C0011D-46X-4, 78.4 cm
Depth: Hole C0011C/C0011D = 0.00–347.82 mbsf
Age: Holocene–upper Miocene

Two depositional subunits are distinguished within Unit I based on the degree of bioturbation, the degree of induration, and the prevalence and thickness of ash layers. Subunit IA is composed of soft greenish gray to grayish silty clay, clayey silt, and clay with abundant thin (<50 cm) intercalations of volcanic ash (Fig. F5) and common thin, few-millimeter thick green bands showing higher Fe content in X-ray fluorescence (XRF) scan data (Fig. F6). At 251.52 mbsf, the mud becomes stiffer (designated as mudstone), bioturbation intensifies, and ash layers are comparatively scarce (Fig. F7). This change marks the top of Subunit IB. It correlates to the shift in LWD response in Hole C0011B at 251.5 m LWD depth below seafloor (LSF) (Expedition 322 Scientists, 2010) and in physical properties (see "Physical properties"). A more complete description of these subunits is presented as follows.

Subunit IA

Interval: Sections 333-C0011C/C0011D-1H-1, 0.0 cm, through 333-C0011D-34X-1, 3.0 cm
Depth: Hole C0011C/C0011D = 0.00–251.52 mbsf
Age: Holocene–Pliocene

Subunit IA comprises a 251 m thick succession of greenish gray silty clay, clayey silt, and clay with minor amounts of grayish silty clay and <50 cm intercalations of volcanic ash layers. Bioturbation is particularly observed in the upper part of the unit. *Zoophycos* and *Chondrites* burrows are abundant. Patches of ash and pumice are observed throughout the succession as <1 cm silt-sized intervals with mottled color and as scattered grains or clasts (see Site C0011 smear slides in "Core descriptions"). Silt- and sand-sized ash layers are more common in the uppermost half of the subunit to ~100 mbsf (Figs. F3, F4). Notable is also a marked increase in sedimentation rate below 80 mbsf (see "Biostratigraphy").

Deposition in Subunit IA was dominated by hemipelagic settling. However, several sand-sized ash layers display turbidite characteristics (basal lamination and upward fining) (Fig. F5) and contain significant amounts of reworked volcaniclastic grains as observed in smear slides (Fig. F7; see also Site C0011 smear slides in "Core descriptions"), suggesting these were remobilized. The occurrence of fresh volcanic ash is important throughout the succession, gradually decreasing toward the Subunit IB boundary (Fig. F3). A small mass transport deposit (MTD) characterized by mixed sediments containing mud clasts is observed in the uppermost few meters of Hole C0011C, between 0.85 and 2.77 mbsf (Core 333-C0011C-1H).

Subunit IB

Interval: Sections 333-C0011D-34X-1, 3.0 cm, through 46X-4, 78.4 cm
Depth: Hole C0011D = 251.52–347.82 mbsf
Age: latest Pliocene–upper Miocene

The Subunit IA/IB boundary is marked by the abrupt appearance of abundantly burrowed and moderately consolidated mudstone (Section 333-C0011D-34X-1, 3 cm) (Fig. F3). In addition, a sharp gradient of ash alteration is observed on smear slides from discrete ash layers (Fig. F8; see also Site C0011 smear slides in "Core descriptions"). In an ash layer at Section 333-C0011D-35X-1, 72 cm, glass shards have no sharp edges and present dissolution pits. In an ash layer at Section 333-C0011D-35X-CC, 12 cm, glass appears almost entirely replaced by clay. From this level down to near the transition to lithologic Unit II, all ash layers observed on smear slides are altered with no or very little remaining glass. The dominant lithology of Subunit IB is a heavily bioturbated greenish brown to dark gray mudstone with only minor occurrence of altered volcanic ash layers (Figs. F3, F7). Clay minerals and altered volcanic glass are the most abundant particles on smear slides, with accessory percentages of nannofossils, quartz, and opaque

minerals (Figs. F8, F9; see Site C0011 smear slides in "Core descriptions"). Heavy minerals appear as trace percentages in most of the subunit.

Deposition of Subunit IB was dominated by hemipelagic settling with minor contribution of volcanic ash and low-energy volcaniclastic turbidity currents that become more abundant toward the base of the subunit. Other than the differences in the degree of bioturbation (higher in Subunit IB) and occurrence of volcanic ash layers (lower in Subunit IB), there is no obvious primary lithology-based observation that could be related to the level of induration and volcanic ash alteration within Unit I. The sudden change in physical properties and correlated change in ash alteration state may thus be related to postdepositional diagenetic processes.

Lithologic Unit II (volcanic turbidite facies)

Interval: Sections 333-C0011D-46X-4, 78.4 cm, through 52X-CC, 0.35 cm
Depth: Hole C0011D = 347.82–379.93 mbsf (total depth)
Age: late Miocene

Expedition 322 Scientists (2010) defined the top of Unit II at 340 mbsf (i.e., starting depth of RCB coring in Hole C0011B), referring to LWD data that show the first occurrence of sand layers at 337 m LSF and define the top of logging Subunit 2B. Detailed comparison between correlated lithology, natural gamma measured on whole-round multisensor core logger (MSCL-W) from the two expeditions, and LWD data (Fig. F10), however, reveals that this sand layer at 337 m LSF is not one of the characteristic coarse-grained tuffaceous sandstones that define the volcanic turbidite facies (see Expedition 322 Scientists [2010] and detailed description below). Instead, almost complete recovery over the critical interval during Expedition 333 allows for confident identification of the first occurrence of a coarse-grained tuffaceous sandstone and thus the top of Unit II at 347.82 mbsf (Section 333-C0011D-46X-4, 78.4 cm). The base of Unit II was not cored during Expedition 333 but extends to 479.06 mbsf as defined in Hole C0011B (Expedition 322 Scientists 2010) (Table T2).

Below the Unit I/II boundary, mudstone (silty claystone to clayey siltstone) is less indurated than in Subunit IB and fresh volcanic glass is abundant (Fig. F8). The upper part of Unit II is dominated by coarser grained tuffaceous sandstone, heterolithic gravel, gravelly sand, and sand beds with sharp and well-defined upper and lower boundaries (Figs. F11, F12). These beds are separated by mud very similar to that of Subunit IB with respect to mineralogy, texture, and bioturbation intensity. The upper sandstone beds show normal grading with some scattered pumice. The beds in the middle part of the unit are also normally graded, and intervals of heterolithic gravel are dominated by pumice and mudstone clasts. In some cases, the upper and lower boundaries of these gravelly intervals are gradational. In other cases, there are sharp upper boundaries (Fig. F11). The lowermost bed cored in Hole C0011D shows normal grading and comprises some scattered pumice. Biotite, orthopyroxene, and hornblende are common in the tuffaceous sandstones (Fig. F12; see Site C0011 smear slides in "Core descriptions").

Throughout the deposition of Unit II, the paleoenvironment was dominated by sediment transport within a sandy turbidite system. Miocene sandy turbidites have previously been identified in the Shikoku Basin; the Miocene siliciclastic turbidites at Ocean Drilling Program (ODP) Site 1177 were derived from a relatively large land mass, most likely southern Japan, and the dispersal system spread terrigenous sediment over a broad area of the Shikoku Basin (Shipboard Scientific Party, 2001a; Fergusson, 2003). However, the deposits of Unit II were derived from a different source. See Expedition 322 Scientists (2010) for more detailed description of sandstone and inferred interpretation of provenance and of the channel system through which the turbidity currents moved.

X-ray diffraction data

According to the X-ray diffraction (XRD) data (Fig. F13; Table T3), the relative abundance of total clay minerals for the entire drilled succession averages 63 wt%. There is a general trend of increasing relative abundance of clay minerals with depth: an average of 57 wt% at the top of the hole, increasing to an average of 67 wt% (ranging between 74 and 46 wt%) in Subunit IB and in background mudstones within Unit II. The relative clay mineral abundance in Unit II, however, drops within (tuffaceous) sandstone beds.

Quartz is relatively stable in its relative abundance throughout Holes C0011C and C0011D (Fig. F13; Table T3), with only a slight decreasing trend occurring between ~200 and 250 mbsf (~2 wt% relative change), marking a slight but detectable difference in mineralogical composition between Subunit IA (average = 19 wt%) and Subunit IB (average = 17 wt%) and Unit II (average = 16 wt%). Similarly, feldspar abundance at the top of Unit I reaches an average of 18 wt% compared to an average of 12 wt% in Subunit IB. The relative amount of feldspar then increases downhole and reaches a maximum of 46 wt% within (tuffaceous) sandstone layers in Unit II.

Calcite is only a trace constituent between 150 and 215 mbsf and again below 318 mbsf (Fig. F13; Table

T3). However, calcite maxima are recorded close to the seafloor, at 250 mbsf (i.e., at the top of the highly bioturbated Subunit IB), and at ~310 mbsf. Calcite abundance decreases steadily with depth below these maxima. Thick beds of tuffaceous sandstone and gravel are depleted in calcite.

X-ray fluorescence data

XRF analyses were performed on 57 samples from Holes C0011C and C0011D to estimate the bulk chemical composition of the sediments and to characterize compositional trends with depth and/or lithologic characteristics (Fig. F14; Table T4).

Lithologic Unit I (hemipelagic/pyroclastic facies)

As with the underlying units (Underwood et al., 2009), major element contents in the hemipelagic mud of Unit I span a relatively small range of values that resemble those of the upper continental crust as defined by Taylor and McLennan (1985). No significant change in major element contents can be observed over the Subunit IA/IB boundary (Fig. F14). The bulk composition of the MTD occurring next to the surface is similar to that of mud, whereas sand and volcanic ash layers show significantly different compositions.

With the exception of few outlying samples, SiO_2, Fe_2O_3, MgO, and TiO_2 contents of mud appear fairly uniform throughout the entire unit (Fig. F14), with average values of 62.1 wt% for SiO_2, 6.52 wt% for Fe_2O_3, 2.46 wt% for MgO, and 0.690 wt% for TiO_2. Above ~80 mbsf, Al_2O_3 content shows slightly lower values than the underlying sediments whereas CaO content appears to be higher and more scattered. This may reflect the lower proportion of clay minerals together with the higher and more variable proportion of calcite observed by XRD in the upper part of Unit I. From the seafloor to ~80 mbsf, K_2O content in mud shows an overall decreasing trend and appears constant throughout the rest of the unit. This may reflect variations of clay mineralogy in the uppermost 80 m of sediments. With depth, Na_2O and P_2O_5 contents gently decrease throughout Unit I and MnO values increase and scatter below ~150 mbsf.

One outlying sample of hemipelagic mud at 238.44 mbsf shows very high Fe_2O_3 concentration (up to 22.6 wt%) together with high MnO and CaO contents and low SiO_2 and Al_2O_3 concentrations (Fig. F14). This high Fe_2O_3 content, associated with very high sulfur concentration (up to 11 wt%, see "Organic geochemistry"), likely accounts for the presence of pyrite (FeS_2), a mineral that is scattered in this unit (see Site C0011 smear slides in "Core descriptions").

Volcanic materials sampled in the upper part of Unit I have high SiO_2 and Na_2O concentrations together with low Al_2O_3, Fe_2O_3, MgO, P_2O_5, and TiO_2 contents compared to the background composition of the hemipelagic mud (Fig. F14). The volcanic sand and the ash layer sampled at 45.02 and 125.08 mbsf show significantly higher K_2O content than the ash layer sampled at 134.20 mbsf (4.90 wt% versus 2.15 wt%). Such a difference in composition may suggest either a change or a chemical evolution of the volcanic sources in the upper part of Unit I.

Compared to the average composition of Unit I, the sample of sand analyzed at 338.54 mbsf shows relatively high CaO, MnO, and P_2O_5 concentrations (Fig. F14). This difference is likely related to the presence of apatite ($Ca[PO_4]_3[F,Cl,OH]$), commonly observed in sandstone (see Site C0011 smear slides in "Core descriptions"), and rhodochrosite ($MnCO_3$) as suggested by Underwood et al. (2009) to explain the very high MnO content in the lime mudstones of the underlying Units II and III.

Lithologic Unit II (volcanic turbidite facies)

Major element compositions of mudstones and tuffaceous sandstones analyzed in the upper part of Unit II are consistent with the data of Underwood et al. (2009) as shown in Figure F14. When compared to the background composition of mudstone, tuffaceous sandstones show relatively high SiO_2 and Na_2O contents together with low Al_2O_3, Fe_2O_3, MgO, TiO_2, and K_2O concentrations. Around the Unit I/II boundary, the overall increasing with depth trend in Al_2O_3 concentration is followed by an abrupt downward decrease between 340 and 380 mbsf and an even more abrupt return to background values. This transition may result from a major volcanic event that dramatically changed the chemical composition of the sediment input at ~380 mbsf. Such a volcanic event constitutes a potential source for the tuffaceous material found in the overlying sandstones and may account for the increasing trend in SiO_2 content as well as the second-order decreasing Fe_2O_3, MgO, and TiO_2 values observed at the same depths.

Structural geology

Holes C0011C and C0011D provide sparse and subtle structures. Structural data measured on cores are given in C0011.XLS in STRUCTUR in "Supplementary material." Where possible, planar structures were corrected to true geographic coordinates using shipboard paleomagnetic data (see "Structural geol-

ogy" in the "Methods" chapter [Expedition 333 Scientists, 2012]). The distribution of planar structures with depth is shown in Figure F15. The main structural features encountered in Holes C0011C and C0011D are subhorizontal to moderately dipping beds, high- to moderately dipping faults, low-angle healed faults, shear zones, and vein structures in the shallow part.

Bedding

Bedding planes are recognized as boundaries between hemipelagic mud and sand or volcanic ash. In addition, a series of laminations in a turbidite sequence is measured at interval 333-C0011D-44X-6, 61–99 cm (338.68–339.06 mbsf). Dip angles of Hole C0011C and C0011D beds are mainly subhorizontal or gentle. In lithologic Subunit IA (0–251.54 mbsf), bedding strike is scattered and most dips range 0°–15° between 0 and ~100 mbsf (Fig. F16A). Below ~100 mbsf in lithologic Subunit IA to its base, bedding surfaces gently dip northwestward with dip angles of 10°–30° (Fig. F16B). Beds in lithologic Subunit IB and Unit II strike east–west and gently dip either northward or southward (Fig. F16C). These bedding dip measurements are roughly consistent with the dips deduced from LWD image analysis (Expedition 322 Scientists, 2010). Bedding below ~100 mbsf is steeper than that of present seafloor inclination. The change of bedding dip may suggest that a tilting event occurred at ~3 Ma, which is the approximate age of the sediments at 100 mbsf.

Faults

High-angle faults (mostly dipping 40°–subvertical) developed in lithologic Subunit IA (Fig. F15). They exhibit brittle deformation features without any gouge layer or X-ray computed tomography (CT) value variation (Fig. F17). The faults often contain striations inferred to be slickenlines on the fault surface that are indicative of dip-slip movement. Offsets observed on the split core surfaces range from 1 mm to 5 cm (in most cores <1 cm). Although the orientations of these faults are scattered, two conjugate sets of faults, one striking north-northeast–south-southwest and the other striking northwest–southeast, are dominant (Fig. F18). The orientation of north-northeast–south-southwest conjugate sets implies vertical loading and maximum horizontal principal stress (σ_{Hmax}) in a north-northeast–south-southwest direction, which coincides with ~N25° maximum horizontal stress direction inferred from borehole breakouts observed at 600–650 mbsf at Site C0011 (Expedition 322 Scientists, 2010). On the other hand, northwest–southeast conjugate sets suggest vertical loading and northwest–southeast σ_{Hmax}, which is consistent with the direction of present plate convergence.

Fault distribution is heterogeneous: in places, faults develop very densely at 10–20 cm intervals (e.g., Cores 333-C0011D-5H, 10H, 16H), but mainly one or two faults are observed in each section. Although these faults are commonly observed in HPCS cores, they are scarce in EPCS and ESCS cores. The difference in observed fault density may be caused by a difference in core quality. However, it is possible that some of the faults could be generated during coring. No high-angle faults are observed in lithologic Unit II.

Low-angle healed fault

Layer-parallel healed faults develop in lithologic Subunit IB and Unit II (Fig. F15). These faults have thicknesses of <5 mm and are characterized by higher bulk density in X-ray CT images (Fig. F19), which suggests shear-induced compaction. Severe biscuiting of ESCS cores only allowed paleomagnetic reorientation of three of these structures, which face eastward to southward (Fig. F20).

Low-angle healed faults formed in bioturbated hemipelagic mudstones at other Nankai Trough Seismogenic Zone Experiment (NanTroSEIZE) drilling sites such as IODP Sites C0006 and C0007 (Expedition 316 Scientists, 2009a, 2009b). The existence of low-angle healed faults at Site C0011 suggests that at least some of such low-angle healed faults at Site C0006 and Site C0007 were formed before sediments passed through the deformation front. In contrast, deformation bands with thrust-sense offsets are commonly found in nonbioturbated mudstone of Sites C0006 and C0007 (Expedition 316 Scientists, 2009a, 2009b) but are not observed in Holes C0011C and C0011D at all. This implies that deformation bands were formed at a later stage of deformation.

In Hole C0011D, several low-angle planar structures display no clear offset. In such cases, we described them as "dark zones." There are several possibilities for the origin of dark zones: sedimentary structure, bioturbation, alteration-related reaction seam, low-angle healed fault, or wood fragments.

Shear zones

Shear zones are occasionally found at this site. They are characterized as continuous planar bands, thicker than several millimeters, and with high CT numbers (Fig. F21). Shear zones show high-angle dips and strike eastward to southward (Fig. F22). Displacement on these shear zones is larger than on other localized shear structures; the counterparts of offset markers are not observed within core.

Veins

Sediment-filled veins (vein structures) are recognized as parallel sets of sigmoidal or planar seams generally less than a few millimeters wide that tend to extend perpendicular to bedding (Fig. F23). Some of them have shear displacement. In X-ray CT images, sediment-filled veins are expressed as bands with slightly higher CT numbers, suggesting concentration of relatively denser minerals or enhancement of porosity reduction within veins. They are found in the shallower part of Site C0011 (above 102 mbsf).

Only one mineral vein occurs at Section 333-C0011D-41X-6 (317.69 mbsf) (Fig. F24). The mineral vein is composed of white-colored minerals that fill a crack within a dark zone.

Biostratigraphy

Preliminary analysis of the core catcher samples from Holes C0011C (Sections 333-C0011C-1H-CC to 3H-CC) and C0011D (Sections 333-C0011D-1H-CC to 52X-CC) reveals assemblages of calcareous nannofossils. Biostratigraphic datums are derived from coccoliths. According to these datum events, the composite section of Holes C0011C and C0011D has a late Pleistocene to late Miocene age.

Calcareous nannofossils

Preliminary examination of all core catcher samples from Holes C0011C and C0011D obtained well to very poorly preserved nannofossils, which occur in common abundance in most samples, and species diversity is comparatively high. However, severe dissolution also occurred, leading to coccolith-barren or very poor occurrences in some intervals. Most of the zonal markers of Martini's zonation (1971) and Raffi et al. (2006) were identified in the sedimentary sequence. The nannofossils occurring in Holes C0011C and C0011D are listed in Tables T5 and T6.

Emiliania huxleyi and *Pseudoemiliania lacunosa* are absent in Sample 333-C0011C-1H-CC. The last occurrence (LO) of *P. lacunosa* is found in Samples 333-C0011C-1H-CC to 2H-CC. *Gephyrocapsa parallela,* which appears younger than 0.90 Ma, was found in Samples 333-C0011C-2H-CC to 3H-CC.

Reticulofenestra asanoi, which indicates the late Pleistocene (0.436~0.90 Ma), is found in Sample 333-C0011D-1H-CC. The first occurrence of medium *Gephyrocapsa* spp. (3.5~5.5 µm; 1.67 Ma) is identified in Samples 333-C0011D-3H-CC to 4H-CC. The LO of *Discoaster brouweri,* which defines the top of Zone NN18 (2.06 Ma), is recognized between Samples 333-C0011D-4H-CC and 5H-CC. The LO of *Discoaster pentaradiatus,* which indicates the top of Zone NN17 (2.50 Ma), is found below Sample 333-C0011D-7H-CC. Samples 333-C0011D-9H-CC to 14H-CC are characterized by the occurrence of *Discoaster tamalis,* which assigns this interval to Zone NN16 (between 2.87 and 3.79 Ma). The LO of *Reticulofenestra pseudoumbilicus* (3.79 Ma) is also identified between Samples 333-C0011D-16H-CC and 47X-CC. *Amaurolithus* spp., which indicates Zone NN14 (4.50 Ma), is found below Sample 333-C0011D-29X-CC. *Discoaster quinqueramus* and *Discoaster berggrenii,* which indicate upper Miocene Zone NN11 (5.59~8.52 Ma), are found in Samples 333-C0011D-36X-CC to 50X-CC. The paracme end (Raffi et al., 2006) of *R. pseudoumbilicus* (7.10 Ma) is identified in Samples 333-C0011D-47X-CC to 48X-CC.

The assemblages obtained through all the holes are characterized by the occurrence of warmer water species such as *Discoaster* spp. and high species diversity (Tables T5, T6).

Sedimentation rates based on biostratigraphy

The changes in sedimentation rates in Holes C0011C and C0011D, based on calcareous nannofossils, are shown in Figure F25 and Table T7. The sedimentation rate was 5.74 cm/k.y. between 0.436 and 0.903 Ma, which corresponds to Samples 333-C0011C-1H-CC to 2H-CC. In continuation, the slightly lower sedimentation rates of 2.21, 2.09, 4.22, and 2.21 cm/k.y. between 0.903 and 2.87 Ma correspond to the upper part of the sequence. The middle part of the sequence (upper depth limit 143–224.953 mbsf shows high sedimentation rates of 6.57 and 10.70 cm/k.y. from 2.87 to 4.5 Ma. Sedimentation rates in the lower part of the sequence are 4.04 and 5.89 cm/k.y. from 4.5 to 7.122 Ma (upper depth limit 224.953 mbsf to lower depth limit 359.421 mbsf). Ages and sedimentation rates obtained are consistent with Expedition 322 results, which situate the nannofossil Zone NN11a/NN10 boundary (8.54 ± 0.24 Ma) between 417.67 and 421.39 mbsf.

Paleomagnetism

Magnetic susceptibility and remanent magnetization of 373 specimens were measured at Site C0011 during Expedition 333. Two specimens were collected for each ordinary section (~140 cm long), and one specimen was collected from each short section. Characteristic remanent magnetization (ChRM) of the specimens was analyzed using stepwise alternating-field (AF) demagnetization in the Zijderveld diagrams (see "Paleomagnetism" in the "Methods" chapter [Expedition 333 Scientists, 2012]). Only one sample (333-C0011D-40X-3, 37–39 cm) underwent

the stepwise thermal demagnetization process (see **"Paleomagnetism"** in the "Methods" chapter [Expedition 333 Scientists, 2012]).

Drilling-induced magnetization occurs commonly during drilling operations as shown by previous Deep Sea Drilling Project/ODP/IODP expeditions. Such an induced magnetization is characterized by a high angle of natural remanent magnetization (NRM) inclination that is overwritten by strong bias of vertical (toward +90°) remagnetization. As shown in Figure **F26,** NRM inclination is steeper than remanent magnetization inclination after 30 mT AF demagnetization. This indicates that NRM is overwritten by drilling-induced magnetization. Based on stepwise AF demagnetization, such drilling-induced magnetizations are mostly removed by 20–30 mT AF demagnetization (Fig. **F27**). Therefore, we use the remanent magnetization data after 30 mT AF demagnetization as the ChRM for this site. ChRM was also characterized by the thermal demagnetization curve from 300° to 600°C thermal demagnetization at 306.69 mbsf (interval 333-C0011D-40X-3, 37–39 cm).

Characteristics of declination and inclination in HPCS cores are different from those in EPCS and ESCS samples. Declinations are random in EPCS and ESCS samples from Cores 333-C0011D-24T to 52X (Fig. **F26**), whereas declinations of remanent magnetization after 30 mT AF demagnetization are arranged in an array in each HPCS core from Cores 333-C0011C-1H to 333-C0011D-22H. In HPCS cores, the declination array is rotated (clockwise or counterclockwise) and indicates that the core has been twisted during drilling operation (e.g., Core 333-C0011D-12H) (Fig. **F26**), and the inclination of remanent magnetization after 30 mT AF demagnetization steepens downward in each core. This may indicate coring disturbances (e.g., stretch of core sediments).

The magnetic susceptibility profile is similar to the NRM intensity profile. Magnetic susceptibility is likely controlled by lithology of the sediments, which implies that the NRM intensity profile may also depend on lithology.

The inclination of remanent magnetization after 30 mT AF demagnetization clearly shows normal and reversed chrons and subchrons as shown in Figure **F28** and Table **T8.** Because we did not measure the samples successively throughout the cores, we were not able to detect certain chron and subchron boundaries. Our data indicate that polarity seems to change gradually as a transitional zone. Therefore, the transitional zone depth was calculated using an average of the top and base boundary depths.

The Brunhes Chron is identified from a sample in Section 333-C0011C-1H-1 as the first normal chron at Site C0011 (Fig. **F28;** Table **T8**). The normal chron changes to a reversed predominant interval, the Matuyama Chron, at 17.36 mbsf. This boundary corresponds to the Brunhes/Matuyama Chron boundary and indicates an age of 0.781 Ma (Lourens et al., 2004). The Gauss Chron, a predominantly normal interval, is identified at 75.72 mbsf. The age of the Matuyama/Gauss Chron boundary is 2.581 Ma (Lourens et al., 2004). The Gauss Chron transitions to a predominantly reversed interval, the Gilbert Chron, at 126.72 mbsf with an age of 3.596 Ma (Lourens et al., 2004). The base of the Gilbert Chron is located at 282.798 mbsf with an estimated age of 6.033 Ma. Magnetostratigraphy below the Gilbert Chron is not firm because frequent magnetic reversal, especially before 7.14 Ma, is beyond our sampling resolution. We leave our tentative assignment of 7.14 Ma at 333.19 mbsf as the bottom of age assignment for Hole C0011D. Although the age for the interval overlapped with Hole C0011B (340–379.93 mbsf) that was drilled during Expedition 322 is not assigned, the age-depth profile shows good continuity to the age of 7.642 Ma at 341.44 mbsf from Expedition 322 data (Fig. **F29**). Our paleomagnetostratigraphy is consistent with the onland tephrochronologic correlations (see **"Lithology"** and Table **T8**).

Based on our results, the average sedimentation rate throughout these holes is ~4.63 cm/k.y. The rate changes rapidly at ~90 mbsf (~3 Ma). Above ~90 mbsf the sedimentation rate is low (~2.86 cm/k.y.), whereas the interval between 90 and 208 mbsf is characterized by a higher sedimentation rate (~8.65 cm/k.y.) (Fig. **F29**). Projected ages of lithologic subunit/unit boundaries are 5.32 Ma for the Subunit IA/IB boundary and 7.67 Ma for the Unit I/II boundary.

Physical properties

The goal of physical property measurements in Holes C0011C and C0011D was to provide high-resolution data on the bulk physical properties and their downhole variations. All physical property measurements were made after cores had been imaged by X-ray CT and had equilibrated to room temperature (~20°C). Whole-round multisensor core logger (MSCL-W) data were collected to define natural gamma radiation, gamma ray attenuation (GRA) density, noncontact resistivity, magnetic susceptibility, and *P*-wave velocity. *P*-wave velocity data from the MSCL-W were of poor quality and will not be discussed. Thermal conductivity was measured using the full-space needle probe method on whole-round cores or the half-space line source method on working halves of

cores. The half-space method was used on sediments below 311 m core depth below seafloor (CSF) because the sediments below this depth were too hard to allow insertion of the needle probe. Penetrometer, vane shear, and electrical resistivity measurements were made shortly after the core was split, and moisture and density (MAD) analyses were performed on discrete samples collected from either the working halves of split cores or cluster samples taken adjacent to whole-round samples. Penetrometer and vane shear measurements were not conducted below 163 m CSF because the sediments became too stiff to allow measurement. Discrete resistivity and *P*-wave velocity measurements in the *x*-, *y*-, and *z*-directions were performed on sample cubes cut from working halves of cores below 215 m CSF.

MSCL-W

MSCL-W data were collected on whole-round sections to define GRA density, electrical resistivity, magnetic susceptibility, and natural gamma radiation. Figure F30 shows the results of MSCL-W measurements on cores, which are summarized and correlated with Expedition 322 logging units (dashed lines) using LWD data from Hole C0011A, and lithologic units from Expedition 333. GRA density, electrical resistivity, and natural gamma radiation all increase slightly with depth, whereas magnetic susceptibility decreases with depth. The variation patterns of GRA density, electrical resistivity, magnetic susceptibility, and natural gamma radiation generally show good agreement with each logging unit.

GRA density

GRA density was calculated by gamma ray attenuation measured using the MSCL-W. Although measurement errors exist in GRA density data because of the presence of air between core and core liner, in general, GRA density tends to reflect the characteristic of each lithologic unit (Fig. F30). Density slightly decreases from the seafloor to 250 m CSF. However, GRA density abruptly increases at 250 m CSF, coinciding with the logging Unit 1/2 boundary.

Magnetic susceptibility

Magnetic susceptibility generally and gradually decreases with depth (Fig. F30). From the seafloor to 80 m CSF, magnetic susceptibility shows little variation; however, it decreases from 80 to 200 m CSF. After a small step increase of magnetic susceptibility between 200 and 230 m CSF, magnetic susceptibility tends to decrease slightly downhole, with the exception of spikes of high magnetic susceptibility from 337 to 410 m CSF. These high-value spikes of magnetic susceptibility correlate with tuffaceous sandstones (see lithology in Fig. F3).

Natural gamma radiation

Natural gamma radiation is plotted with gamma ray data from LWD in Figure F30. Although natural gamma radiation measured by MSCL-W is systematically lower than gamma ray data from LWD, the variation patterns are similar. Natural gamma radiation gradually increases with depth to ~200 m CSF. At 250 and 480 m CSF (near the logging Unit 1/2 and 2/3 boundaries), natural gamma radiation shows large step increases. Many intervals of low natural gamma radiation are found between 337 and 440 m CSF where tuffaceous sand layers exist. This variation is also consistent with LWD data.

Electrical resistivity

Electrical resistivity generally increases with depth (Fig. F30). From the top of Site C0011 to 250 m CSF, a low-resistivity section is observed. Then, resistivity abruptly increases at 250 CSF where porosity decreases. From 337 m CSF, where tuffaceous sand layers were cored, resistivity gradually increases downhole with strong local variation.

Moisture and density measurements

MAD measurements on discrete samples from Site C0011 provide a detailed characterization of bulk density and porosity. All MAD data from Expedition 333 are provided in Table T9, and results from Expeditions 322 and 333 are summarized below.

From the surface to ~50 m CSF, bulk density generally increases and porosity decreases downhole as expected for progressive burial (Fig. F31). This trend reverses between ~50 and ~80 m CSF, and then porosity remains relatively constant until ~240 m CSF. A sharp increase in bulk density (decrease in porosity) occurs between ~240 and 270 m CSF, after which a steady compaction trend continues to the base of the drilled interval.

The absence of bulk density and porosity variation between 80 and 240 m CSF is anomalous. Similar behavior was observed at ODP Site 1173, the reference site for the Muroto transect, and Site 1177, the reference site for the Ashizuri transect (Shipboard Scientific Party, 2001b, 2001c) (Fig. F32). Spinelli et al. (2007) attributed the Site 1173 anomalously high porosities at shallow depths to cementation provided by opal-CT and the abrupt porosity decline to dissolution of these cements as temperature exceeded 55°C.

Below the depth of rapid porosity decline at Site C0011, the porosity depth profiles at Sites C0011, 1173, and 1177 are remarkably similar (Fig. F32).

Strength measurements

The strength of soft sediments was measured using an analog vane shear device (Wykeham Farrance, model WF23544) and a pocket penetrometer (Geotest E284B) in the working half of the core from 0 to 162 m CSF (Fig. F33). Beneath this depth, high sediment strength did not allow measurements with these devices. Both vane shear and penetrometer data sets are highly scattered, particularly below 40 m CSF.

P-wave velocity and anisotropy

P-wave velocity was measured on discrete cube samples cut from working halves. Measurements were made in three directions orthogonal to the *x*-, *y*-, and *z*-axes of the core reference. The horizontal-plane anisotropy (α_{VPhor}, α_{phor}) and vertical-plane anisotropy (α_{VPvert}, α_{pvert}) were calculated (see "Physical properties" in the "Methods" chapter [Expedition 333 Scientists, 2012]).

P-wave velocity in Hole C0011D varies from 1557 to 2333 m/s and increases with depth (Table T10). The high velocities near the base of lithologic Unit I correspond to volcaniclastic sands in this interval. The values measured in this expedition match the values measured in Expedition 322 in the zone of overlap from 340 to 380 m CSF.

Vertical-plane anisotropy of velocity (α_{VPvert}) (see "Physical properties" in the "Methods" chapter [Expedition 333 Scientists, 2012]) is slightly >0, indicating average horizontal velocity is greater than vertical velocity (Fig. F34). This is the expected trend in transversely isotropic sediments because acoustic waves propagate more slowly perpendicular to bedding. The anisotropy values match those measured during Expedition 322 (Expedition 322 Scientists, 2010) in the zone of overlap but exhibit less scatter. This is probably due to better core recovery in this interval during this expedition relative to Expedition 322.

A velocity-porosity relationship is developed with measured *P*-wave velocity and nearest neighbor (<66 cm offset) porosity data (Fig. F35). For comparison to the observations, empirical relationships for *P*-wave velocity versus porosity from (1) global compilations for "normal" and "high" consolidation sediment (Erickson and Jarrard, 1998) and (2) Shikoku Basin sediments (Hoffman and Tobin, 2004) are plotted. The global compilations provide loose upper and lower bounds for the expected relationship between velocity and porosity. The trend reported for Shikoku Basin sediments is

$$V_P = 0.746 + 0.532\phi + \{0.305/[(\phi + 0.124)2 + 0.051]\} + 0.61(v_{sh} - 1.123)X_1,$$

where

V_P = *P*-wave velocity,
ϕ = porosity,
v_{sh} = shale fraction (0.32), and
$X_1 = \tanh[40(\phi - \phi_c)] - |\tanh[40(\phi - \phi_c)]|$,

where critical porosity (ϕ_c) is 0.295 (Hoffman and Tobin, 2004). The *P*-wave velocity values measured in Hole C0011D generally fall inside the envelope defined by these trends, which matches the trend from Expedition 322. There are some outliers from Hole C0011D with anomalously high porosity. These points correspond to the lowest part of lithologic Subunit IA (see "Moisture and density measurements"), which has high velocity relative to that which would be expected from these velocity-porosity models. Some additional high-velocity points (>1800 m/s) correspond to sands near the base of lithologic Unit I, illustrating that differences in lithology may cause some points to lie outside the bounds of these velocity-porosity trends.

Electrical resistivity and anisotropy

In soft sediments, from 0 to 210 m CSF, the resistivity was measured with a four-pin, 2 kHz Wenner array. These measurements are consistent with the baseline values provided by the MSCL, with lower scatter. Resistivity generally increases with depth as a result of pore volume loss. Here, resistivity increases from 0.8 to 0.95 ± 0.15 Ωm between 0 and 20 m CSF then remains stable at 0.95 ± 0.15 Ωm until 80 m CSF (Fig. F36). Resistivity slightly decreases to 0.85 ± 0.05 Ωm between 80 and 120 m CSF, which is consistent with the higher porosities at these depths. Then resistivity increases to 0.95 ± 0.15 Ωm again and remains at this value to 220 m CSF.

Electrical resistivity measured on cube samples varies from 0.6 to 2.6 Ωm (Table T11; Fig. F36, F37). Measurements from discrete samples show continuity with data from the Wenner array. Anisotropy was calculated from resistivity measurements made in the *x*-, *y*-, and *z*-directions. In most cases, vertical resistivity is greater than horizontal (see "Physical properties" in the "Methods" chapter [Expedition 333 Scientists, 2012]), with vertical anisotropy becoming more negative downhole. The anisotropy values from this expedition match well with those measured in Hole C0011B during Expedition 322 (Expedition 322 Scientists, 2010) and exhibit the same trend with depth (Fig. F37). Measured resistiv-

ity values from this expedition increase slightly downhole but exhibit little variation. There is an abrupt increase in resistivity at the lithologic Unit I/II boundary. This could be due to the greater sand abundance in Unit II causing resistivity to increase or differences in data quality between this expedition and Expedition 322 because of the use of a different probe setup (see the "Methods" chapter [Expedition 333 Scientists, 2012]). Core recovery and core quality during Expedition 322 were generally poorer than during this expedition, and because resistivity measurements are strongly affected by coring disturbances such as coring-induced fractures, this may also account for the difference in data between the two expeditions. The general downhole trend of resistivity anisotropy becoming more negative is probably controlled by the alignment and flattening of pores caused by consolidation and grain reorientation.

The relationship between porosity and resistivity is illustrated by a log-log plot of porosity and resistivity (Fig. F38); resistivity was matched with nearest neighbor porosity values (within 30 cm) from MAD measurements. The points in the zone of anomalously high porosity from 80 to 240 m CSF do not fit the general trend from the rest of the data. This could hypothetically be due to the presence of a cementing phase (Ellis and Singer, 2007) or a change in clay mineralogy (Henry, 1997).

Thermal conductivity and heat flow

Nine in situ temperatures were measured from 22.5 to 184.5 m CSF using the advanced piston corer temperature tool (APCT-3) (Fig. F39). Temperature tends to increase linearly with depth. The average geothermal gradient determined by a least-squares regression on the nine temperature measurements is ~91.3°C/km, which is much higher than the average thermal gradient (~63°C/km) of Hole C0018A. The mean seafloor temperature obtained from the intercept of a least squares regression on the nine temperature measurements is ~1.7°C.

To estimate heat flow, we made 585 thermal conductivity measurements on core samples from Hole C0011D. Measurements were made with a full-space needle probe in most cases and a half-space line source if the needle probe could not be used because a core sample was too hard. Thermal conductivity ranges from 0.62 to 1.41 W/(m·K) (Fig. F40). Thermal conductivity with depth tends to be constant to 250 m CSF and then abruptly increases at 250 m CSF, which coincides with a logging boundary. For clastic sediments, the main controlling factors on thermal conductivity are porosity and quartz content. At Site C0011, thermal conductivity appears inversely correlated with porosity.

We estimated heat flow by multiplying the average thermal gradient by the harmonic mean of thermal conductivity (~0.98 W/[m·K]) estimated in the interval where temperatures were measured. Estimated heat flow is ~89.5 mW/m^2 in Hole C0011D, which is much higher than heat flow (~62 mW/m^2) in Hole C0018A.

To estimate temperatures from the seafloor to the basement, we used the Bullard method, which requires surface heat flow and thermal conductivity data (Fig. F41). Based on seismic reflection data, basement depth is estimated to be 1050 mbsf (Expedition 322 Scientists, 2010). Because we were not able to obtain complete cores from Hole C0011D, thermal conductivities determined from measurements on samples from Expedition 322 Hole C0011B were used in temperature estimates (Expedition 322 Scientists, 2010). A thermal conductivity of 1.35 mW/m^2 was assumed for the undrilled sediments between the base of Hole C0011B and basement. Temperature at the sediment/basement interface is estimated to be ~79°C.

Inorganic geochemistry

The main geochemical objective in Holes C0011C and C0011D, located seaward of the trench, was to document the variations in interstitial water chemical composition at shallow depths that could not be recovered during Expedition 322. In combination with the data obtained during Expedition 322, data from this site may be used to elucidate origins, volume and nature of flow, and fluid-rock interactions that may affect the state and geotechnical properties of the strata at the décollement and their evolution postsubduction. A total of 48 interstitial water samples were squeezed from selected whole-round sections for chemical analyses. Sample depths ranged from 0 to 379 mbsf, with samples from 360 to 379 mbsf overlapping Hole C0011B, which was cored during Expedition 322 (Expedition 322 Scientists, 2010). One sample per core was collected when possible; however, samples were collected at a higher spatial resolution in the uppermost 10 m in order to define the sulfate–methane transition (SMT) zone.

Fluid recovery

In order to obtain enough interstitial water for shipboard and shore-based analyses, whole-round sections from 19 to 41 cm long were squeezed from Holes C0011C and C0011D. Longer sections were squeezed from cores recovered deeper within the

holes where the sediments were more consolidated. Interstitial water volumes normalized by interstitial water section length (mL/cm) are presented as a function of depth in Figure F42A. Interstitial water recovery changes significantly at ~184.5 mbsf. Interstitial water volumes per centimeter of core range from 1.7 to 2.8 mL/cm between 0 and 184.5 mbsf (Cores 333-C0011C-1H to 333-C0011D-21H). Below Core 333-C0011D-21H (~184.5 mbsf), the average interstitial water volume per section length fell to 0.7 ± 0.3 mL/cm.

Because of the semilithified nature of the sediment in many of the deeper cores and the coring methods used, many of the cores taken by the EPCS and ESCS were moderately to highly disturbed. As much of the outer layers of these fractured samples as possible was removed prior to squeezing. Complete removal of the outer layers was not always possible, and thus, the interstitial waters may be contaminated by drilling fluid. Little to no drilling disturbance was noted in cores taken by the HPCS, which included the SMT. The disturbed cores taken via the EPCS or ESCS fell below the SMT; thus sulfate concentration is used to identify and quantify contamination as indicated in "Inorganic geochemistry" in the "Methods" chapter (Expedition 333 Scientists, 2012). The magnitude of possible drilling fluid contamination in the interval recovered by the EPCS and ESCS reaches ~13%; thus the samples that were obtained using the EPCS and ESCS were sulfate corrected for possible drilling contamination following the methods of Expedition 322 (Expedition 322 Scientists, 2010). The HPCS samples were not sulfate corrected. The uncorrected interstitial water data collected at Site C0011 are listed in Table T12. In addition, Table T13 presents a composite data set of uncorrected HPCS data and sulfate-corrected EPCS and ESCS data. The composite data are illustrated in Figures F43 and F44.

Salinity, chlorinity, and sodium

Interstitial water salinity rapidly decreases in the upper 70 m of Holes C0011C and C0011D (Fig. F43). Below this point, salinity continuously decreases. Salinity shows good correlation with the data from Expedition 322 for the overlapping depths. We interpret the rapid decrease in salinity in the upper ~70 m of the sediment section as reflecting active sulfate reduction and the subsequent precipitation of authigenic carbonates, which consumes interstitial water SO_4^{2-}, Ca, and Mg within this interval (Figs. F42B, F43, F44).

Chlorinity increases rapidly in the upper ~25 m of Hole C0011C, as generally observed below the seafloor. In the interval between ~25 and ~250 mbsf, chlorinity values are relatively constant. Below ~250 mbsf, chlorinity decreases with increasing depth. This is consistent with the results of Expedition 322 and may reflect diffusional exchange with a deeper stratigraphic interval where freshened interstitial water migrated along sandy turbidites. Freshening of the interstitial water probably occurred at depths considerably greater than the coring limits for this hole, where clay mineral dehydration reactions have advanced.

Dissolved sodium increases in the upper ~36 m of Site C0011. Sodium values are relatively constant from 36 to ~250 mbsf, followed by a slightly decreasing trend with depth, which was also observed during Expedition 322 in Hole C0011B.

Biogeochemical processes

Sulfate and alkalinity

Sulfate concentration decreases rapidly in the upper 70 m of Hole C0011C, followed by a less dramatic decrease from 70 to 183 mbsf, which corresponds to the end of HPCS coring (Fig. F42B). Sulfate is less continuous in the interval from ~200 to 380 mbsf, in which the EPCS and ESCS were used. The sulfate profile documents a sulfate reduction zone that is deeper than is observed at other sites in the Nankai area (e.g., Moore, Taira, Klaus, et al., 2001; Tobin et al., 2009). However, this site and Site C0012 are the only sites with known interstitial water sulfate concentration that are located in the Shikoku Basin. Site 1173 had overlying trench turbidites, the upper part of Site 1177 was not cored, and other sites were either in the trough or on the margin. Considering that the sedimentation within the uppermost 300 m at Site C0011 is dominantly hemipelagic with <0.5 wt% total organic carbon (TOC) deposited at relatively low sedimentation rates (<100 m/m.y.,) a relatively deep sulfate reduction zone is understandable. The scattering of sulfate below ~190 mbsf may reflect seawater intrusion resulting from disturbance during coring.

Interstitial water alkalinity increases sharply in the upper part of Hole C0011C and reaches a maximum at 79 mbsf. Alkalinity then decreases with depth to ~300 mbsf and increases again below this level (Fig. F43). The alkalinity trend shows a good correlation with interstitial water measured in the deeper sediments in Hole C0011B. A concurrent maximum in alkalinity and progressive change in sulfate concentration gradient at ~80 mbsf defines an upper zone of sulfate reduction at 40–150 mbsf. However, this zone does not correspond to the SMT. Methane concentration only reaches detection threshold below 260 mbsf (see "Organic geochemistry") then progressively increases downward and reaches relatively high but scattered values in lithologic Unit II. Fur-

thermore, sulfate is present at small concentrations to at least 183 mbsf. Barium concentration in solution rises sharply below 300 mbsf, indicating the remaining sulfate is removed from solution in this depth range, concurrently with a small increase of alkalinity. The SMT thus appears located some distance above the Unit I/II boundary (see **"Lithology"**). Its depth may be influenced by a minor methane source in Unit II, which has a slightly higher average TOC content than the hemipelagites above and/or by lateral migration in the tuffaceous sandstones.

Ammonium, phosphate, and bromide

Dissolved ammonium rapidly increases in the upper 95 mbsf of Holes C0011C and C0011D, which is followed by a slight decrease from 95 to 380 mbsf (Fig. **F43**). We interpret the initial increase as being the result of microbially mediated decomposition of organic matter. The decline with depth likely reflects decreasing metabolic rates, thus declining ammonium production as well as NH_4 sorption onto clay minerals.

Phosphate increases sharply with depth in Hole C0011C and the uppermost part of Hole C0011D, peaking at 36 mbsf and then exponentially decreases with depth to 380 mbsf (Fig. **F43**). The initial rapid increase in phosphate reflects active organic matter decomposition, which occurs at the top of the zone of active sulfate reduction. The decreasing and low phosphate below the depth of maximum concentration is likely controlled by the solubility of apatite, which is a major sink for phosphate.

Bromide concentration increases with depth in Hole C0011C and in the uppermost portion of Hole C0011D and then slightly decreases from ~50 to 380 mbsf (Fig. **F43**). There is some discontinuity between the Br trends in Hole C0011C/C0011D drilled during this expedition and Hole C0011B drilled during Expedition 322.

Major cations (Ca, Mg, and K)

Dissolved calcium in Holes C0011C and C0011D decreases with depth from 0 to ~60 mbsf, below which the profile reverses and Ca gradually increases (Fig. **F44**). There is good continuity with Hole C0011B. The initial decreasing trend may reflect Ca consumption during authigenic carbonate formation in the zone of most intense sulfate reduction. The increase in Ca with depth may reflect progressive ash alteration and carbonate diagenesis downhole.

Magnesium decreases throughout Holes C0011C and C0011D, which is consistent with the trend seen in Hole C0011B during Expedition 322 (Fig. **F44**). The decrease is more rapid in the upper 61 m of the sedimentary section. This zone of rapid Mg depletion roughly corresponds to the sulfate reduction zone, indicating some precipitation of Mg with authigenic carbonates within this depth interval, as well as uptake in clay minerals. The general decrease in Mg may indicate uptake of magnesium in hydrous silicate minerals (mainly clays) formed during volcanic ash alteration.

Potassium decreases throughout Holes C0011C and C0011D (Fig. **F44**). The overall decline in K likely reflects the uptake of dissolved potassium during the alteration of volcanic ash and feldspars.

Minor elements (B, Li, Si, Sr, Ba, Mn, and Fe)

Boron in Hole C0011C rapidly decreases from 480 µM at 0.6 mbsf to 240 µM at ~80 mbsf (Fig. **F43**). Between 80 and ~280 mbsf, boron decreases downhole slightly with some fluctuations then increases with depth to 380 mbsf. These values are consistent with those of the upper portion of Hole C0011B.

Lithium gradually increases from 34.6 µM at 0 mbsf to 166 µM at 250 mbsf and then slightly decreases with depth. Li shows good correlation between Holes C0011C/C0011D and C0011B (Fig. **F44**). The overall increasing lithium trend may reflect authigenic clay formation.

Dissolved silica is generally higher than silica concentration in modern seawater and is generally stable from 0 to 250 mbsf with concentrations of ~650 µM throughout that interval. At ~250 mbsf, silica exhibits a rapid decline to ~100 µM before increasing to ~500 µM at ~380 mbsf. This trend continues in Hole C0011B. The rapid decrease in silica is consistent with the observed decrease in porosity between 240 and 250 mbsf (**"Physical properties"**) as well as the dissolved silica profiles from Sites 1173 and 1177, the reference sites of the Muroto and Ashizuri transects, respectively (Moore, Taira, Klaus, et al., 2001). The secondary silica maximum around 560 mbsf correlates with the tuffaceaous sandstones in lithologic Unit II that still contain unaltered volcanic glass (see **"Lithology"**).

Strontium gradually increases with depth in Holes C0011C and C0011D from 80 µM at the seafloor to 100 µM at 180 mbsf. From 180 to 270 mbsf, Sr rapidly increases from 100 to 130 µM (Fig. **F44**). Sr stays constant or slightly decreases with depth below 170 mbsf. This trend continues in Hole C0011B and may be due to alteration of volcaniclastic material.

Barium gradually increases from 0.6 µM at 0 mbsf to 13 µM at 270 mbsf in Holes C0011C and C0011D and then drastically increases to 95.7 µM in the interval from 270 to 380 mbsf (Fig. **F44**). The increase

at depth may be attributed to a greater amount of barite dissolution or fluid migration in volcaniclastics at this interval.

Dissolved manganese in Holes C0011C and C0011D rapidly increases with depth from 4.2 µM at 0.6 mbsf to 16 µM at 20 mbsf and then decreases to 4.1 µM at 70 mbsf (Fig. F44). Below 70 mbsf, Mn rapidly increases again with depth to 30 µM at 170 mbsf and then generally increases to 50 µM at 380 mbsf with negative excursion in the interval between 270 and 310 mbsf. The rapid incline in the upper interval from 0 to 20 mbsf at this site reflects MnO_2 reduction within a depth interval where MnO_2 is a favorable and important electron acceptor for microbially mediated organic matter decomposition.

In the upper ~70 m of Site C0011, dissolved iron does not exhibit a clear trend (Fig. F44). Below 70 mbsf, Fe is generally constant at >2 µM and although there was little reported data from Expedition 322, the existing data are consistent with the data observed in Holes C0011C and C0011D.

Trace elements (Rb, Cs, V, Cu, Zn, Mo, Pb, and U)

Rubidium in Holes C0011C and C0011D shows a linear decrease from 3600 nM at 0 mbsf to 123 nM at 130 mbsf and then stays constant from 130 to 210 mbsf, followed by a gradual decrease to 570 nM at ~300 mbsf (Fig. F45). Below 300 mbsf, Rb increases to 1090 µM at 350 mbsf and then decreases to 650 µM at 380 mbsf.

Cesium fluctuates twice between ~90 and 350 mbsf (Fig. F45). It decreases with depth from 3.2 nM at 0 mbsf to 1.8 nM at 20 mbsf, followed by an increase to 3.1 nM at 210 mbsf, and then decreases again to 1.3 nM at ~320 mbsf, followed by an increase to 4.2 nM at ~350 mbsf.

Vanadium increases downhole with scattering in Hole C0011C and in the upper part of Hole C0011D from ~40 nM at the surface to ~60 nM at ~100 mbsf (Fig. F45). V concentration abruptly decreases to 36 nM at ~120 mbsf and then decreases to 23 nM at 380 mbsf. Copper exhibits considerable variability throughout Holes C0011C and C0011D, ranging from below detection limit to 4300 nM (Fig. F45). Zinc concentration in Holes C0011C and C0011D fluctuates between ~1000 and ~2000 nM in the upper ~120 m, below which there is no clear trend (Fig. F45).

Molybdenum concentration fluctuates throughout Site C0011 (Fig. F45). Mo decreases from ~100 nM at the surface to ~30 nM at 100 mbsf and then increases to ~200 nM at 300 mbsf, followed by a decrease to ~70 nM at 380 mbsf. Lead is generally low (0.8 ± 0.4 nM) in the upper ~80 mbsf and higher with a less cohesive trend (2.3 ± 1.8 nM) below 80 mbsf (Fig. F45). Uranium is generally low (3.5 ± 2.1 nM) throughout. U exhibits a peak of 24.7 nM at the surface (Fig. F45).

Organic geochemistry

Hydrocarbon gas

At Site C0011, no hydrocarbon gases other than methane were detected in the cored sequence (Table T14). Methane is either below detection or present at low concentrations in the uppermost 250 mbsf with an average value of 1.7 parts per million by volume (ppmv). Methane concentration increases below ~250 mbsf and reaches the maximum value of 873.6 ppmv at 376.4 mbsf (Fig. F46). Results of the present study are thus in agreement with the data from Expedition 322, which reported the presence of heavier hydrocarbons gases (i.e., ethane, propane, and butane) only below 425 mbsf at Site C0011 (Expedition 322 Scientists, 2010).

Sediment carbon, nitrogen, and sulfur composition

A total of 152 sediment samples were collected at Site C0011 and analyzed for concentrations of calcium carbonate ($CaCO_3$), TOC, total nitrogen (TN), and total sulfur (TS) (Table T15; Fig. F47). The atomic ratios of TOC and TN (TOC/TN_{at}) were calculated.

$CaCO_3$ content is highly variable at Site C0011, ranging from 0.25 to 24.51 wt%. From the top of the core to 146.0 mbsf, the sediments are enriched in $CaCO_3$, averaging 5.33 ± 4.60 wt% with a maximum of 17.66 wt% (Fig. F47). Thereafter, $CaCO_3$ content drops to low values (average = 2.80 ± 2.08 wt%) and shows little variation until 238.9 mbsf. From 238.9 to 318.6 mbsf, $CaCO_3$ content increases again and averages 6.70 ± 5.77 wt%. Sediments below 313.8 mbsf are characterized by low $CaCO_3$ values averaging 2.14 ± 1.13 wt%.

TOC content is low throughout the cored sequence and ranges from 0.09 to 0.59 wt% (average = 0.31 ± 0.09 wt%). TOC values are relatively high in the upper ~215 mbsf, where the TOC average is 0.34 ± 0.08 wt%. Beneath an abrupt decrease to 0.21 wt% at 216.0 mbsf, TOC values remain low and uniform until 340.8 mbsf. The values in the lowermost cored sequence are highly variable, ranging between 0.06 and 0.56 wt%. TN content fluctuates between 0.02 and 0.08 wt% with an average of 0.06 ± 0.01 wt% and generally follows the TOC variation pattern.

TOC/TN_{at} ratios vary from 3.2 to 10.7 with an average of 5.6 ± 1.3, suggesting a predominant input of marine-derived organic matter. However, the TOC and TN values at Site C0011 show a relative weak correlation (r^2 = 0.55), possibly suggesting an important contribution of inorganic nitrogen sources. Clay-bound ammonium can make up a significant TN fraction in organic-poor marine sediments (Müller, 1977). The admixtures of this inorganic nitrogen species and organic nitrogen may lead to an overestimate of marine-derived organic matter using the TOC/TN_{at} ratios at Site C0011.

TS content is generally low, varying between 0.02 and 0.34 wt% (average = 0.23 ± 0.96 wt%) throughout most of the cores. Higher average TS values (0.38 ± 1.42 wt%), however, are observed between 84.5 and ~251.1 mbsf. Notably, the sediment at 238.4 mbsf has the maximum TS content of this site (11.86 wt%). This remarkably elevated TS value coincides with the maximum Fe content (see **"Lithology"**), suggesting the enrichment of pyrite at this depth.

Rock-Eval pyrolysis

Twelve selected samples were subjected to shipboard Rock-Eval pyrolysis in order to determine the type and maturity of the sedimentary organic matter preserved in Holes C0011C and C0011D. Thermal distillation of sedimentary organic matter (S1) released <0.1 mg hydrocarbon/g sediment (mg HC/g sediment), while the pyrolytic degradation of nonvolatile organic matter (S2) yielded <0.3 mg HC/g sediment (Table **T16**). The hydrogen index (HI) is rather low and ranges from 26 to 41 mg HC/g TOC (Fig. **F48**). These low HI values are common for a Type III kerogen (Tissot and Welte, 1984) and suggest a terrestrial origin of the sedimentary organic matter. This finding, however, contradicts with the interpretation of the TOC/TN_{at} ratios, which indicate a predominantly marine derived nature of the organic matter. This contradiction can be due to intense degradation, which has been shown to reduce the hydrogen richness of sedimentary organic matter and ultimately lower HI values (Espitalié et al., 1977). An alternative explanation is that a large fraction of hydrocarbons may be adsorbed by clay minerals in TOC-poor sediments, which also can result in artificially low HI values (Espitalié et al., 1984).

T_{max} values range from 336° to 414°C and slightly increase with depth, suggesting a higher degree of thermal alteration of the organic matter at the base of the cored sequence. However, all T_{max} values fall below 430°C, which indicates that the organic matter is at a thermally immature stage.

References

Ellis, D.V., and Singer, J.M., 2007. *Well Logging for Earth Scientists,* (2nd ed.): Dordrecht, The Netherlands (Springer).

Erickson, S.N., and Jarrard, R.D., 1998. Velocity-porosity relationships for water-saturated siliciclastic sediments. *J. Geophys. Res., [Solid Earth],* 103(B12):30385–30406. **doi:10.1029/98JB02128**

Espitalié, J., Laporte, J.L., Madec, M., Marquis, F., Leplat, P., Paulet, J., and Boutefeu, A., 1977. Méthode rapide de caractérisation des roches mètres, de leur potentiel pétrolier et de leur degré d'évolution. *Rev. Inst. Fr. Pet.,* 32(1):23–42. **doi:10.2516/ogst:1977002**

Espitalié, J., Senga Makadi, K., and Trichet, J., 1984. Role of the mineral matrix during kerogen pyrolysis. *Org. Geochem.,* 6:365–382. **doi:10.1016/0146-6380(84)90059-7**

Expedition 316 Scientists, 2009a. Expedition 316 Site C0006. *In* Kinoshita, M., Tobin, H., Ashi, J., Kimura, G., Lallemant, S., Screaton, E.J., Curewitz, D., Masago, H., Moe, K.T., and the Expedition 314/315/316 Scientists, *Proc. IODP,* 314/315/316: Washington, DC (Integrated Ocean Drilling Program Management International, Inc.). **doi:10.2204/iodp.proc.314315316.134.2009**

Expedition 316 Scientists, 2009b. Expedition 316 Site C0007. *In* Kinoshita, M., Tobin, H., Ashi, J., Kimura, G., Lallemant, S., Screaton, E.J., Curewitz, D., Masago, H., Moe, K.T., and the Expedition 314/315/316 Scientists, *Proc. IODP,* 314/315/316: Washington, DC (Integrated Ocean Drilling Program Management International, Inc.). **doi:10.2204/iodp.proc.314315316.135.2009**

Expedition 322 Scientists, 2010. Site C0011. *In* Saito, S., Underwood, M.B., Kubo, Y., and the Expedition 322 Scientists, *Proc. IODP,* 322: Tokyo (Integrated Ocean Drilling Program Management International, Inc.). **doi:10.2204/iodp.proc.322.103.2010**

Expedition 333 Scientists, 2012. Methods. *In* Henry, P., Kanamatsu, T., Moe, K., and the Expedition 333 Scientists, *Proc. IODP,* 333: Tokyo (Integrated Ocean Drilling Program Management International, Inc.). **doi:10.2204/iodp.proc.333.102.2012**

Fergusson, C.L., 2003. Provenance of Miocene–Pleistocene turbidite sands and sandstones, Nankai Trough, Ocean Drilling Program Leg 190. *In* Mikada, H., Moore, G.F., Taira, A., Becker, K., Moore, J.C., and Klaus, A. (Eds.), *Proc. ODP, Sci. Results,* 190/196: College Station, TX (Ocean Drilling Program), 1–28. **doi:10.2973/odp.proc.sr.190196.205.2003**

Hayashida, A., Kamata, H., and Danhara, T., 1996. Correlation of widespread tephra deposits based on paleomagnetic directions: link between a volcanic field and sedimentary sequences in Japan. *Quat. Int.,* 34–36:89–98. **doi:10.1016/1040-6182(95)00072-0**

Henry, P., 1997. Relationship between porosity, electrical conductivity, and cation exchange capacity in Barbados wedge sediments. *In* Shipley, T.H., Ogawa, Y., Blum, P., and Bahr, J.M. (Eds.), *Proc. ODP, Sci. Results,* 156: College Station, TX (Ocean Drilling Program), 137–149. **doi:10.2973/odp.proc.sr.156.020.1997**

Hoffman, N.W., and Tobin, H.J., 2004. An empirical relationship between velocity and porosity for underthrust sediments in the Nankai Trough accretionary prism. *In* Mikada, H., Moore, G.F., Taira, A., Becker, K., Moore, J.C., and Klaus, A. (Eds.), *Proc. ODP, Sci. Results,* 190/196: College Station, TX (Ocean Drilling Program), 1–23. **doi:10.2973/odp.proc.sr.190196.355.2004**

Ike, T., Moore, G.F., Kuramoto, S., Park, J.-O., Kaneda, Y., and Taira, A., 2008. Tectonics and sedimentation around Kashinosaki Knoll: a subducting basement high in the eastern Nankai Trough. *Isl. Arc,* 17(3):358–375. **doi:10.1111/j.1440-1738.2008.00625.x**

Lourens, L., Hilgen, F., Shackleton, N.J., Laskar, J., and Wilson, D., 2004. The Neogene period. *In* Gradstein, F.M., Ogg, J.G., and Smith, A. (Eds.), *A Geologic Time Scale 2004:* Cambridge (Cambridge Univ. Press), 409–440.

Martini, E., 1971. Standard Tertiary and Quaternary calcareous nannoplankton zonation. *Proc. Second Planktonic Conf. Roma 1970,* 2:739–785.

Moore, G.F., Taira, A., Klaus, A., Becker, L., Boeckel, B., Cragg, B.A., Dean, A., Fergusson, C.L., Henry, P., Hirano, S., Hisamitsu, T., Hunze, S., Kastner, M., Maltman, A.J., Morgan, J.K., Murakami, Y., Saffer, D.M., Sánchez-Gómez, M., Screaton, E.J., Smith, D.C., Spivack, A.J., Steurer, J., Tobin, H.J., Ujiie, K., Underwood, M.B., and Wilson, M., 2001. New insights into deformation and fluid flow processes in the Nankai Trough accretionary prism: results of Ocean Drilling Program Leg 190. *Geochem., Geophys., Geosyst.,* 2(10):1058–1079. **doi:10.1029/2001GC000166**

Moore, G.F., Taira, A., Klaus, A., et al., 2001. *Proc. ODP, Init. Repts.,* 190: College Station, TX (Ocean Drilling Program). **doi:10.2973/odp.proc.ir.190.2001**

Müller, P.J., 1977. C/N ratios in Pacific deep-sea sediments: effect of inorganic ammonium and organic nitrogen compounds sorbed by clays. *Geochim. Cosmochim. Acta,* 41(6):765–776. **doi:10.1016/0016-7037(77)90047-3**

Nagahashi, Y., and Satoguchi, Y., 2007. Stratigraphy of the Pliocene to lower Pleistocene marine formations in Japan on the basis of tephra beds correlation. *Quat. Res. (Daiyonki Kenkyu),* 46(3):205–213. **doi:10.4116/jaqua.46.205**

Raffi, I., Backman, J., Fornaciari, E., Pälike, H., Rio, D., Lourens, L., and Hilgen, F., 2006. A review of calcareous nannofossil astrobiochronology encompassing the past 25 million years. *Quat. Sci. Rev.,* 25(23–24):3113–3137. **doi:10.1016/j.quascirev.2006.07.007**

Saito, S., Underwood, M.B., Kubo, Y., and the Expedition 322 Scientists, 2010. *Proc. IODP,* 322: Tokyo (Integrated Ocean Drilling Program management International, Inc.). **doi:10.2204/iodp.proc.322.2010**

Satoguchi, Y., Higuchi, Y., and Kurokawa, K., 2005. Correlation of the Ohta tephra bed in the Tokai group with a tephra in the Miura group, central Japan. *Chishitsugaku Zasshi,* 111(2):74–86.

Shipboard Scientific Party, 2001a. Leg 190 summary. *In* Moore, G.F., Taira, A., Klaus, A., et al., *Proc. ODP, Init. Repts.,* 190: College Station, TX (Ocean Drilling Program), 1–87. **doi:10.2973/odp.proc.ir.190.101.2001**

Shipboard Scientific Party, 2001b. Site 1173. *In* Moore, G.F., Taira, A., Klaus, A., et al., *Proc. ODP, Init. Repts.,* 190: College Station, TX (Ocean Drilling Program), 1–147. **doi:10.2973/odp.proc.ir.190.104.2001**

Shipboard Scientific Party, 2001c. Site 1177. *In* Moore, G.F., Taira, A., Klaus, A., et al., *Proc. ODP, Init. Repts.,* 190: College Station, TX (Ocean Drilling Program), 1–91. **doi:10.2973/odp.proc.ir.190.108.2001**

Spinelli, G.A., Mozley, P.S., Tobin, H.J., Underwood, M.B., Hoffman, N.W., and Bellew, G.M., 2007. Diagenesis, sediment strength, and pore collapse in sediment approaching the Nankai Trough subduction zone. *Geol. Soc. Am. Bull.,* 119(3–4):377–390. **doi:10.1130/B25920.1**

Taylor, S.R., and McLennan, S.M., 1985. *The Continental Crust: Its Composition and Evolution:* Oxford (Blackwell Scientific).

Tissot, B.P., and Welte, D.H., 1984. *Petroleum Formation and Occurrence* (2nd ed.): Heidelberg (Springer-Verlag).

Tobin, H., Kinoshita, M., Ashi, J., Lallemant, S., Kimura, G., Screaton, E.J., Moe, K.T., Masago, H., Curewitz, D., and the Expedition 314/315/316 Scientists, 2009. NanTroSEIZE Stage 1 expeditions: introduction and synthesis of key results. *In* Kinoshita, M., Tobin, H., Ashi, J., Kimura, G., Lallemant, S., Screaton, E.J., Curewitz, D., Masago, H., Moe, K.T., and the Expedition 314/315/316 Scientists, *Proc. IODP,* 314/315/316: Washington, DC (Integrated Ocean Drilling Program Management International, Inc.). **doi:10.2204/iodp.proc.314315316.101.2009**

Underwood, M.B., Saito, S., Kubo, Y., and the Expedition 322 Scientists, 2009. NanTroSEIZE Stage 2: subduction inputs. *IODP Prel. Rept.,* 322. **doi:10.2204/iodp.pr.322.2009**

Underwood, M.B., Saito, S., Kubo, Y., and the Expedition 322 Scientists, 2010. Expedition 322 summary. *In* Saito, S., Underwood, M.B., Kubo, Y., and the Expedition 322 Scientists, *Proc. IODP,* 322: Tokyo (Integrated Ocean Drilling Program Management International, Inc.). **doi:10.2204/iodp.proc.322.101.2010**

Zijderveld, J.D.A., 1967. AC demagnetization of rocks: analysis of results. *In* Collinson, D.W., Creer, K.M., and Runcorn, S.K. (Eds.), *Methods in Palaeomagnetism:* New York (Elsevier), 254–286.

Publication: 18 May 2012
MS 333-104

Figure F1. Detailed bathymetric map of Kashinosaki Knoll and Nankai Trough showing location of Sites C0011, C0012, and C0018.

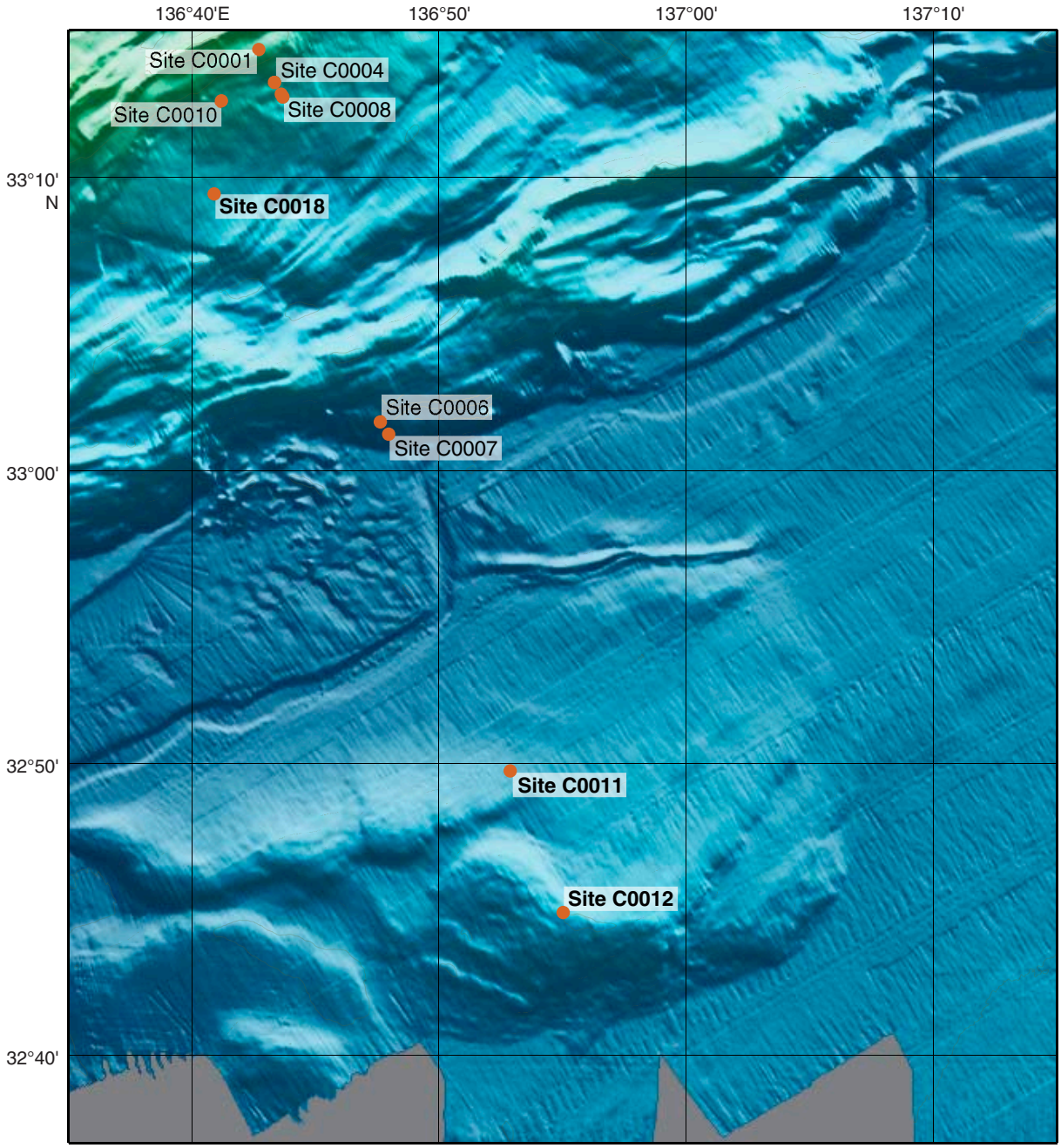

Figure F2. Lithologic columns on seismic background across Kashinosaki Knoll showing Sites C0011 and C0012, using results from Expeditions 333 and 322 (Underwood et al., 2010). VE = vertical exaggeration.

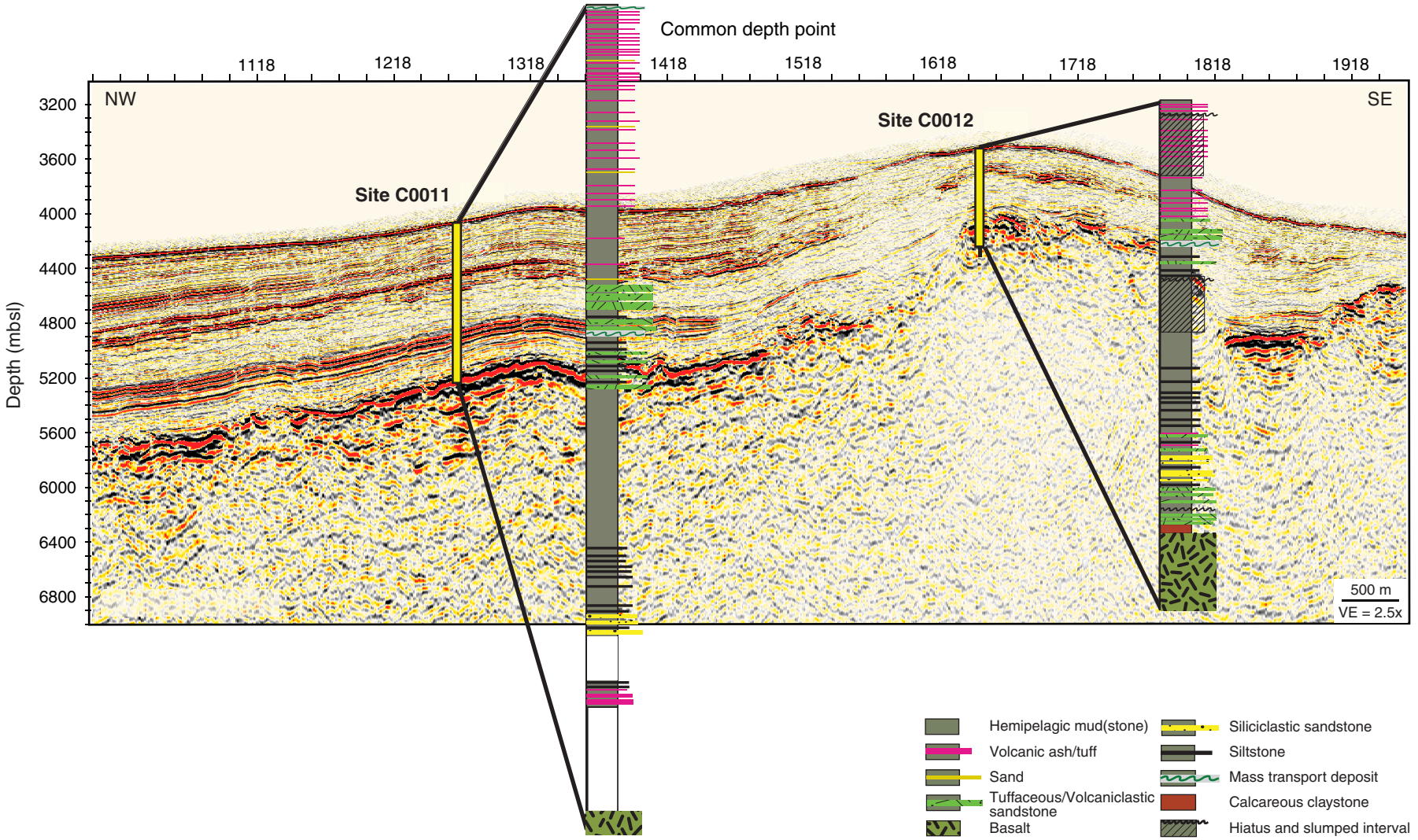

Figure F3. Sedimentary log, Holes C0011C and C0011D. MTD = mass transport deposit.

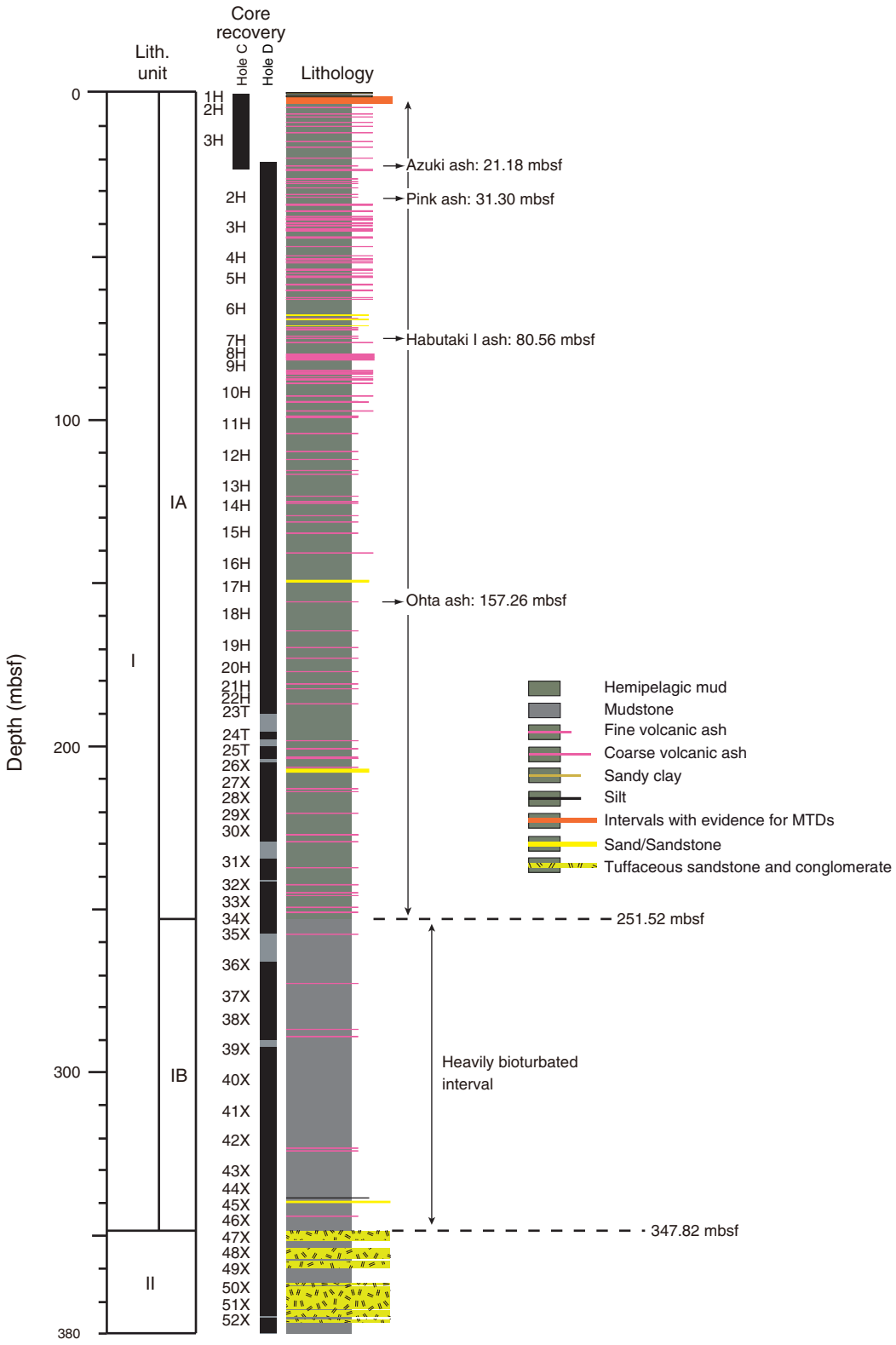

Figure F4. Occurrence of ash and sand depositional events, Holes C0011C and C0011D. MTD = mass transport deposit.

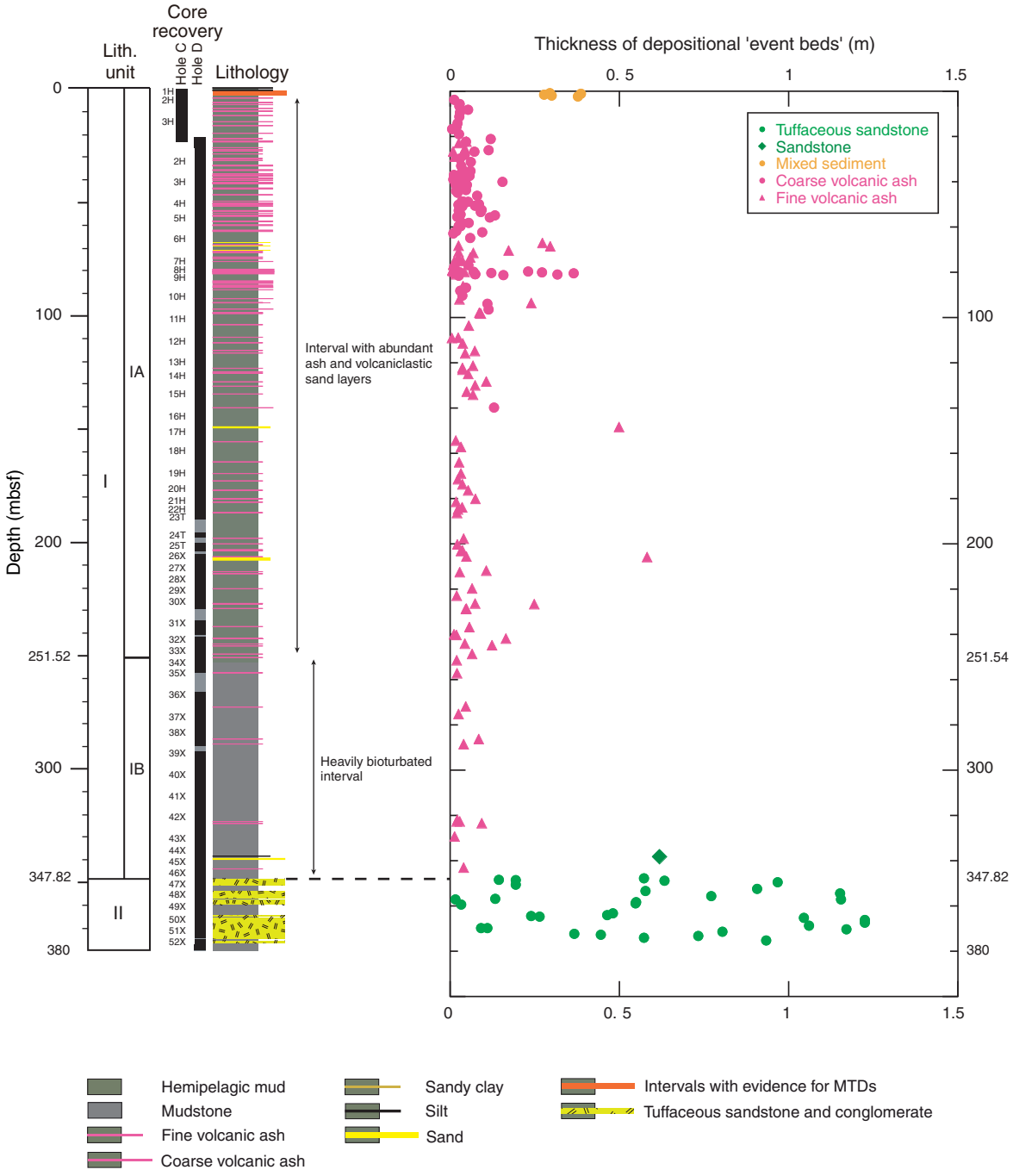

Figure F5. Detail of volcanic ash layers in Subunit IA, Holes C0011C and C0011D. Ash layers occur together with green bands in clay deposits, likely resulting from the accumulation of iron (Fe) in such bands, as revealed by XLF core scanning of green bands in comparable core sections (Fig. F6). **A.** Volcaniclastic silt grading upward into light brown clay with iron bands. **B.** Detail of a brown volcanic ash layer older than the Pink volcanic ash. Fe-rich bands are visible below the ash layer. **C.** Core photo showing a series of stacked volcaniclastic sand layers with erosional bases and fining-upward trends typical of fine-grained turbidite sequences. T = turbidite sequences.

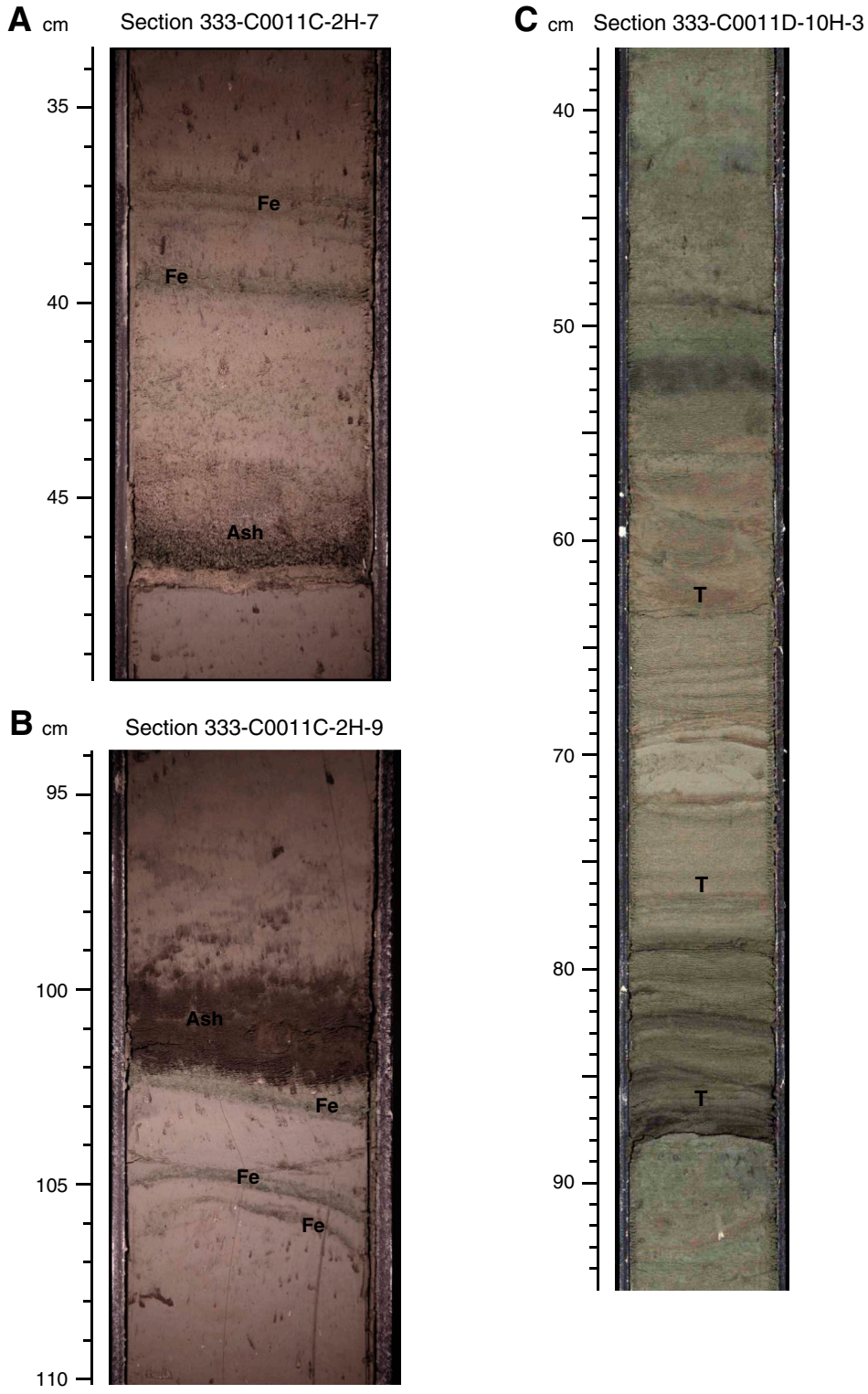

Figure F6. X-ray fluorescence core logging major element data, Sections 333-C0011C-3H-9 and 3H-10. Note the high iron content of the thin green bands.

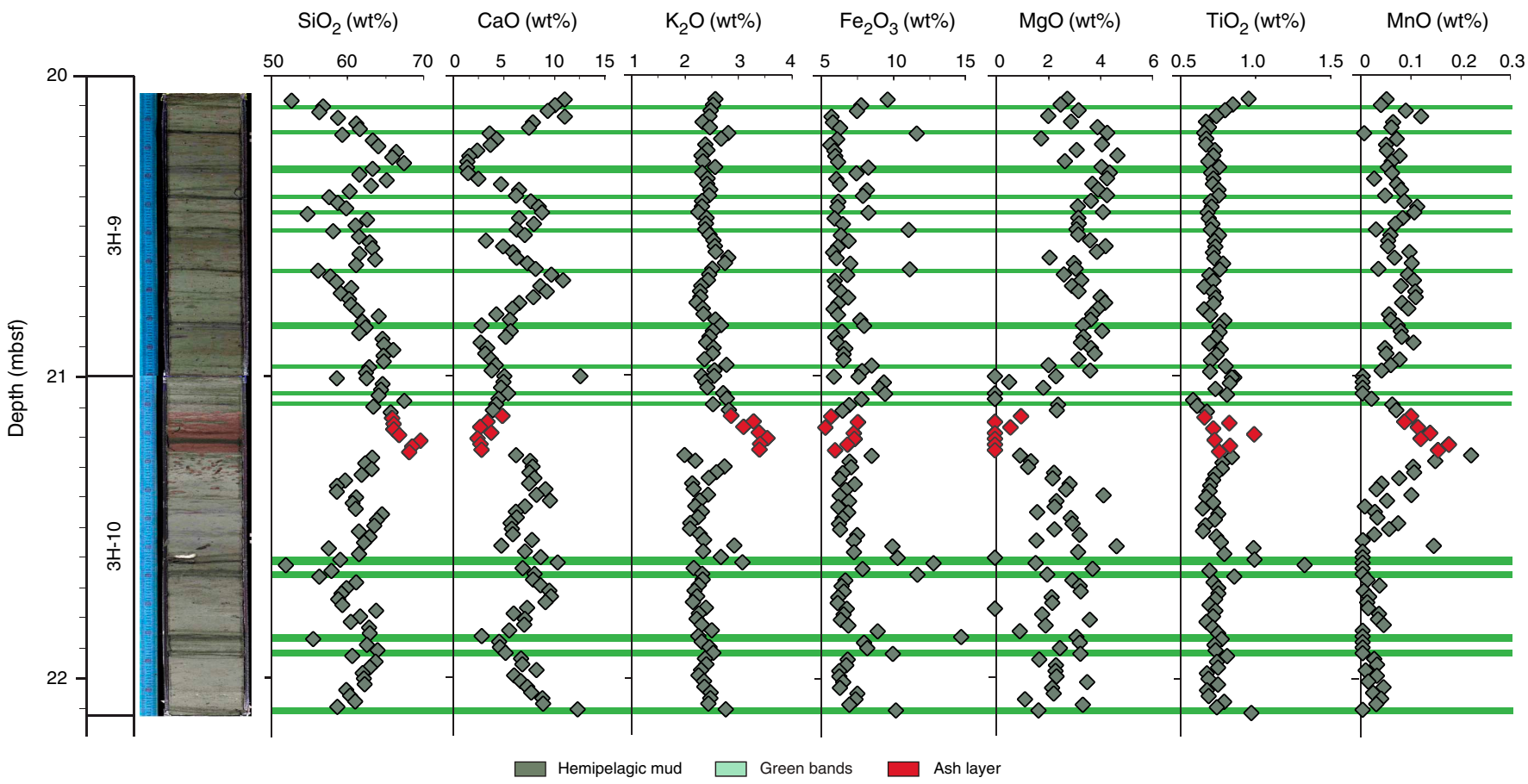

Figure F7. Core photo of strata in Subunit IB, Hole C0011D, showing bioturbated mudstone (example of *Zoophycos* genus). Note the presence of pervasive bioturbation and green staining.

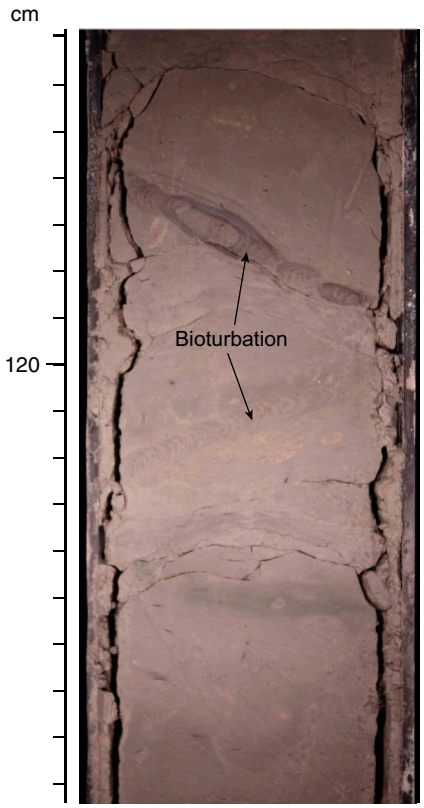

Figure F8. Variations in ash alteration state across Subunit IA/IB boundary and Unit I/II boundary, Hole C0011D. **A.** Last observed downsection occurrence of unaltered glass shards in ash layers immediately above the Subunit IA/IB boundary at 251.52 mbsf (Subunit IA). **B.** First observed downsection appearance of altered glass in the succession at 257.22 mbsf. The appearance of such a degree of ash alteration characterizes strata within Subunit IB. **C.** Relatively larger degree of alteration to the ash shown in B. **D.** Reappearance of unaltered ash within Unit II.

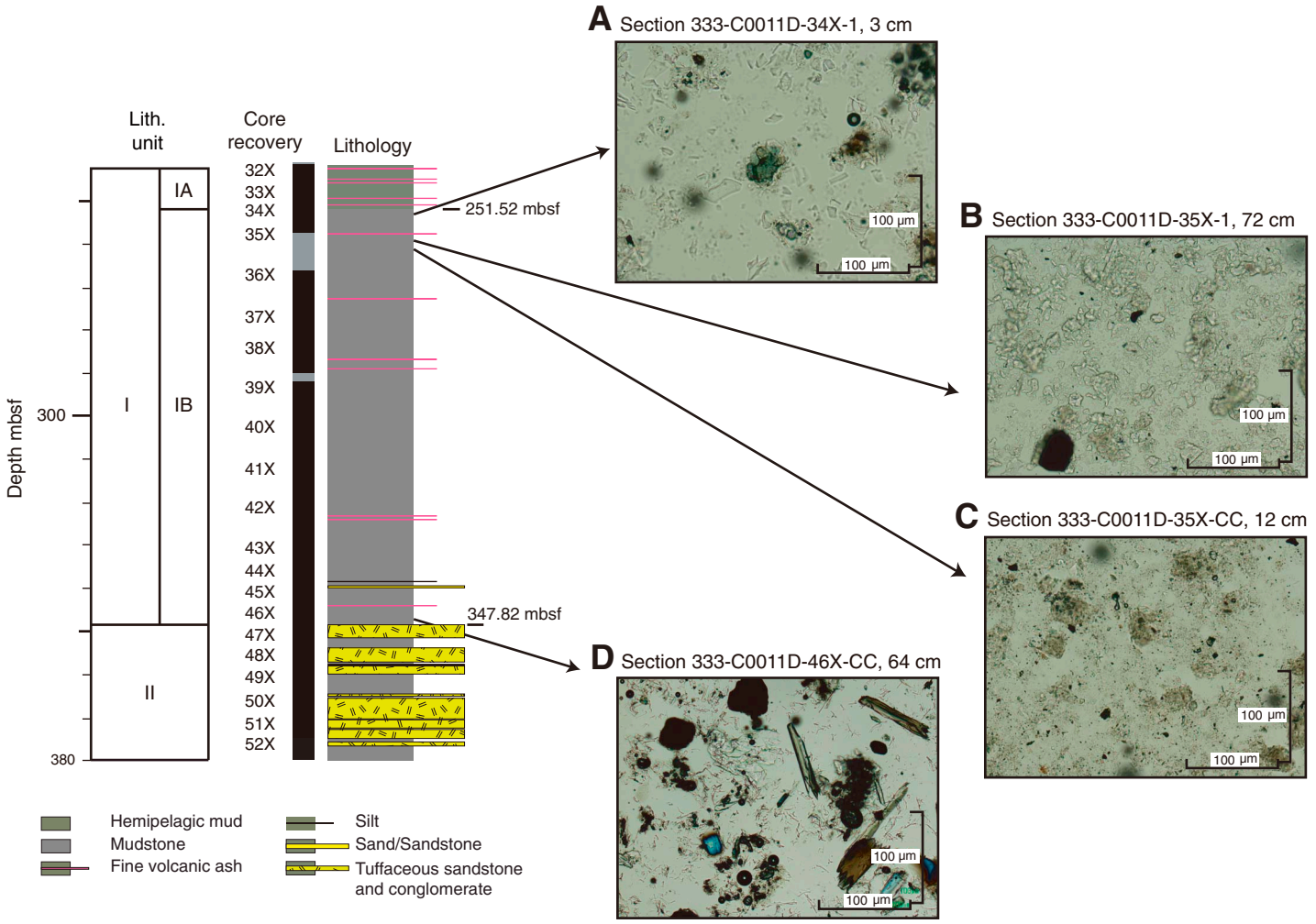

Figure F9. Details of smear slides in Units I and II, Holes C0011C and C0011D. **A.** Very fine volcanic ash with different degrees of weathering. Darker (and larger) ash is heavily weathered, denoting remobilization of volcanic lithic grains. **B.** Volcanic lithic fragments and transparent volcanic ash. B = air bubble due to smear slide preparation. **C.** Abundant *Discoaster* sp. (D).

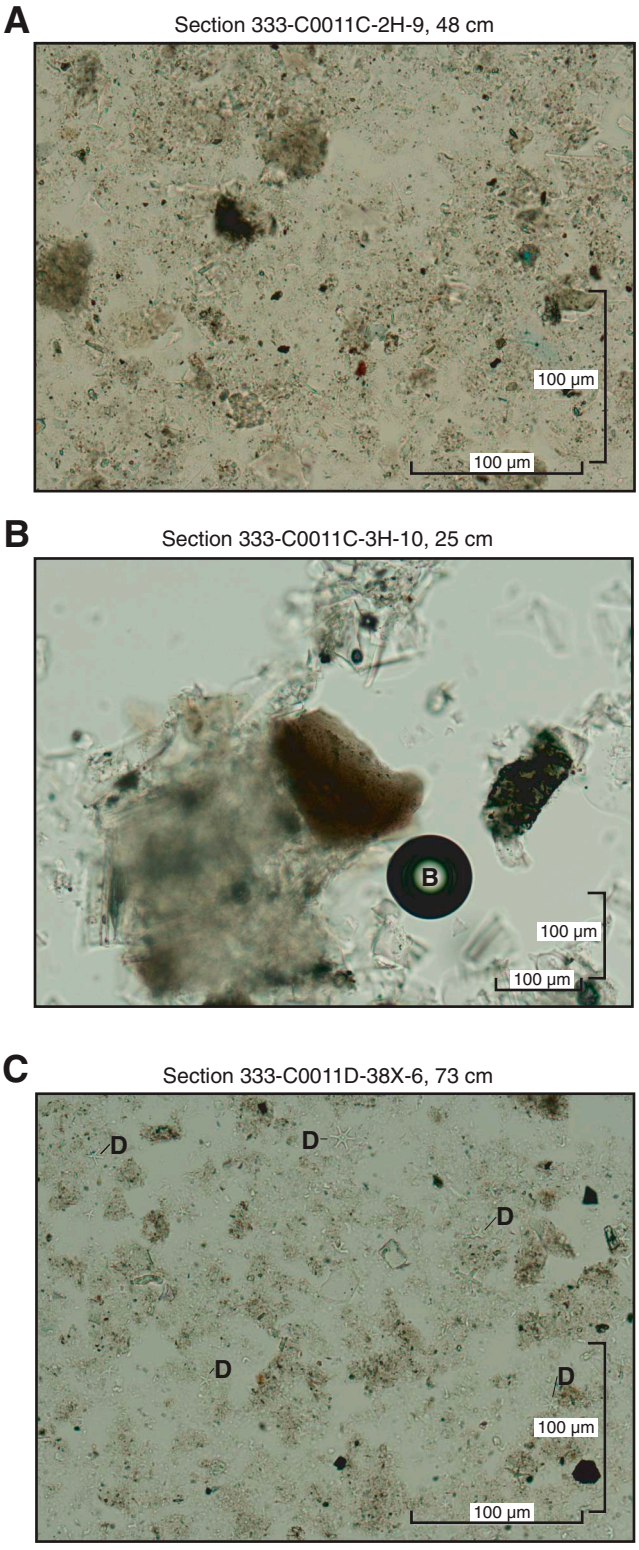

Figure F10. Comparative recoveries of (**A**) ESCS vs. (**B**) RCB cored during Expeditions 333 and 322, respectively, and detailed comparison between lithology from cores in lithologic Unit II and log character in logging Subunit 2B. MSCL = multisensor core logger, NGR = natural gamma ray.

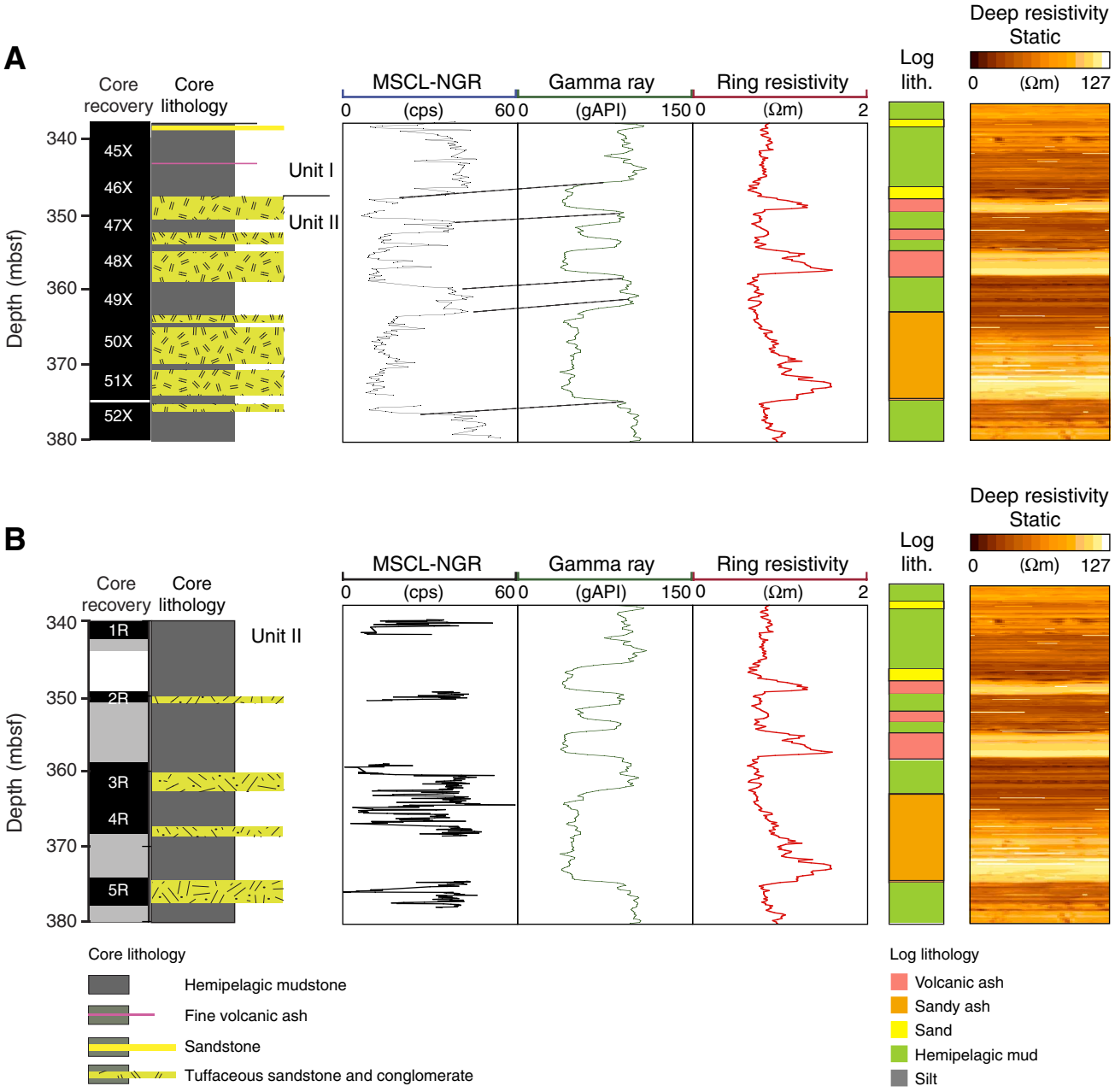

Figure F11. Core photos highlighting the lithologic and textural characteristics of tuffaceous sandstones in Unit II. **A.** Fining-upward trend in the uppermost tuffaceous sandstones defining the top of Unit II (Section 333-C0011D-46X-4). **B.** Detail of coarse sand with gravely clasts within Unit II (Section 47X-1). The tuffaceous sandstone is heterolithic, with clasts presenting lithologies varying from pumice to mudstone and volcanic rock fragments. (**C**) Sections 50X-3 and (**D**) 51X-2 presenting details of tuffaceous sandstones in Unit II showing cored sediment composed of heterolithic gravel, mudstone clasts, and coarse sand. P = pumice, M = mudstone.

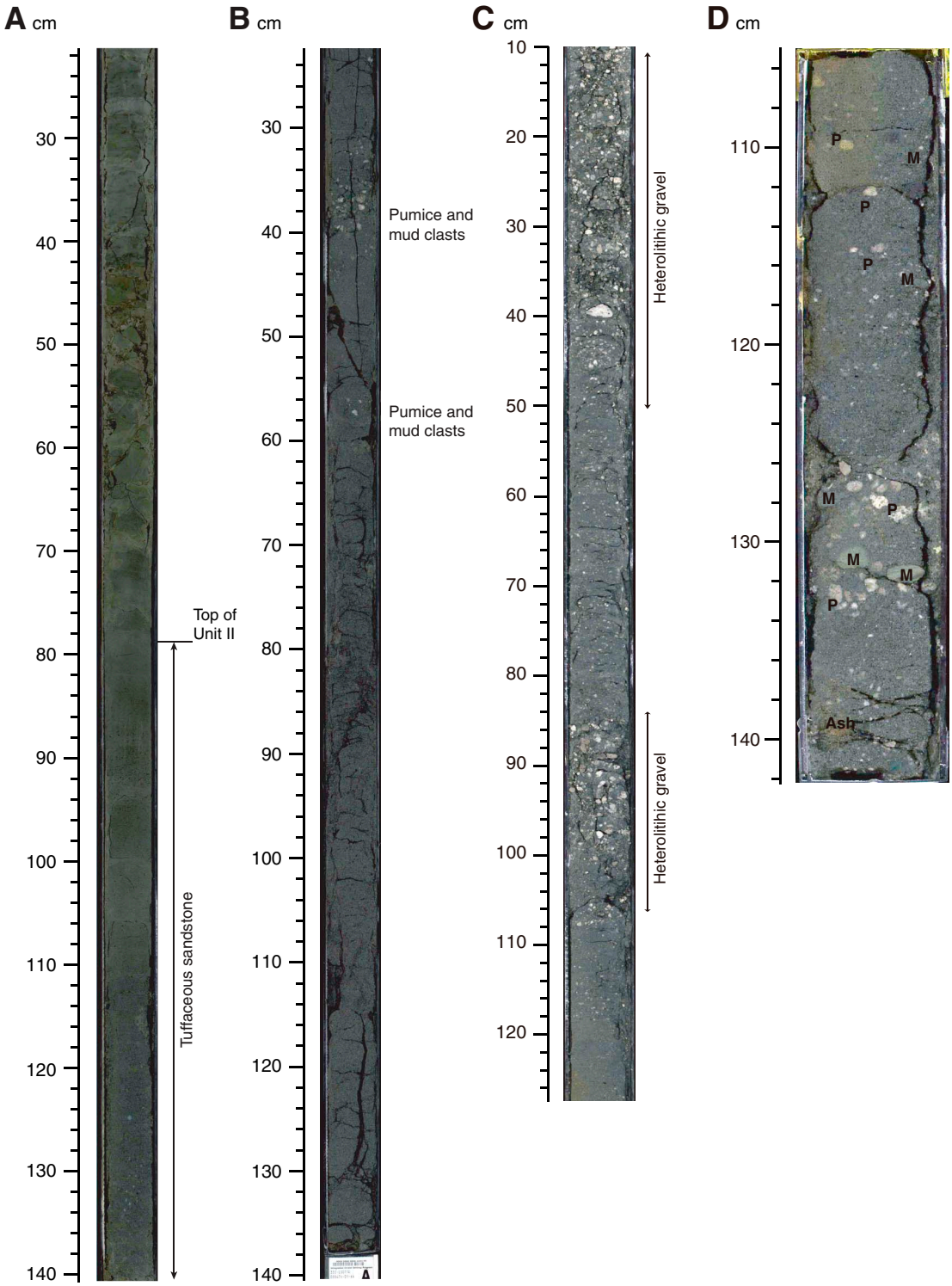

Figure F12. Detail of Section 333-C0011D-51X-3 (entire section) and smear slide photos from Unit II. **A.** Mudstone and heterolithic gravel. **B.** Smear slide (Unit II), showing fragmented Bryozoan shells (Bz), grains of volcanic glass (darker patches are weathered glass) (g), and crystals of orthopyroxene (opx). **C.** Crystals of orthopyroxene (small) and a larger crystal of hornblende (hb), a heavy mineral common in Unit II.

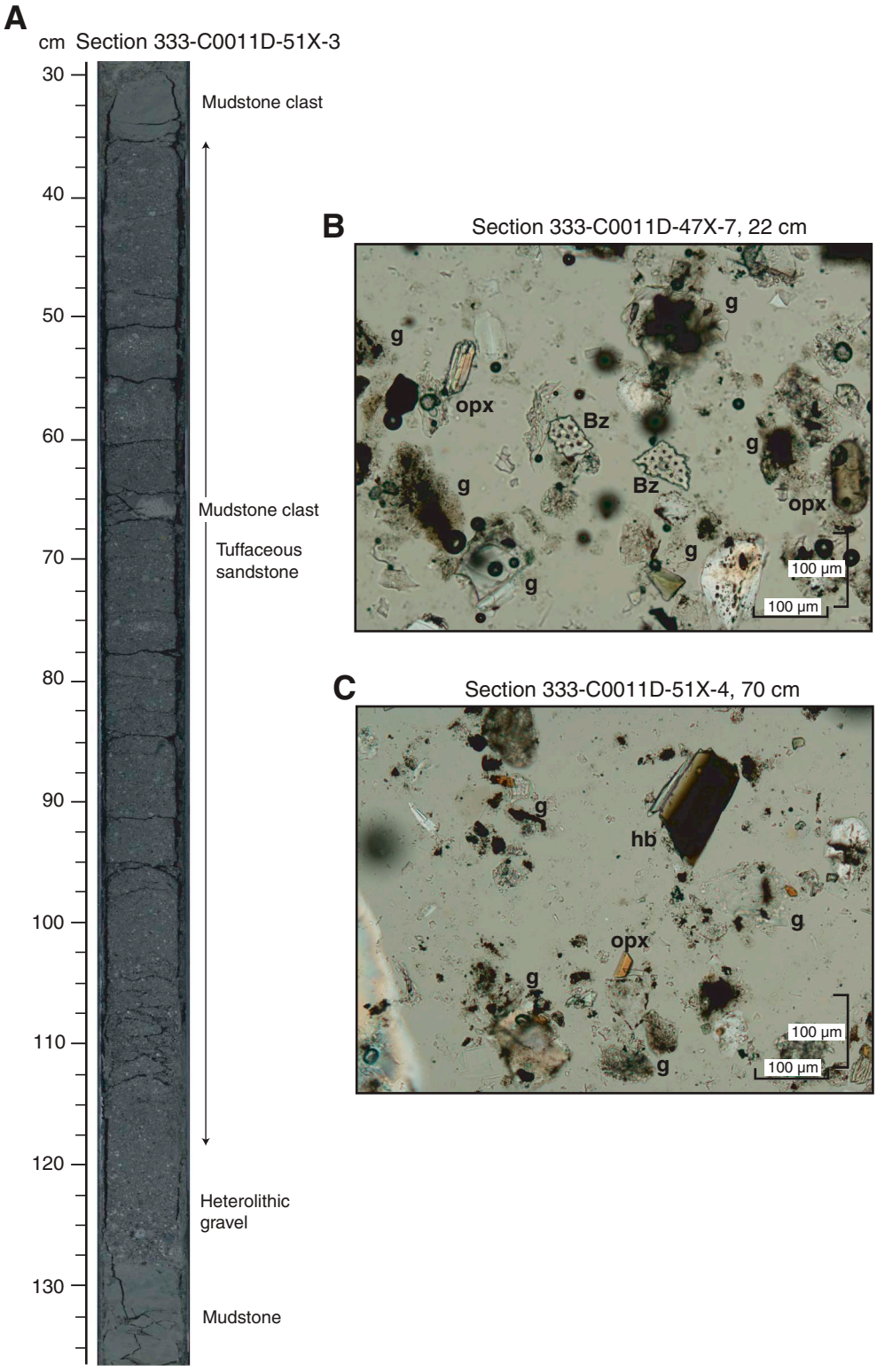

Figure F13. Relative abundance of major detrital constituents from bulk powder XRD data, Holes C0011C and C0011D. MTD = mass transport deposit.

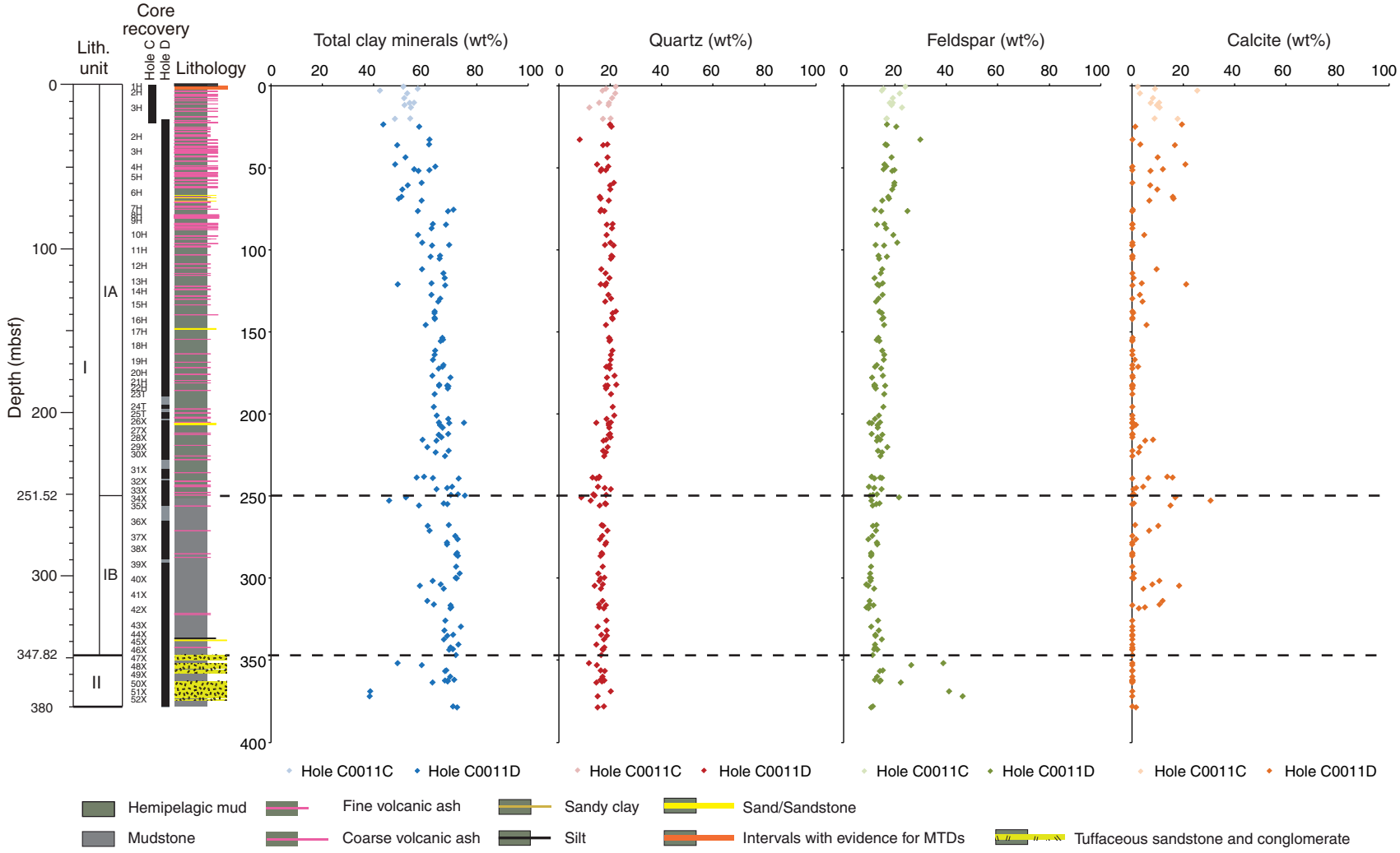

Figure F14. Discrete X-ray fluorescence (XRF) major element (SiO_2, Al_2O_3, CaO, Fe_2O_3, Na_2O, K_2O, and P_2O_5) composition as a function of depth, Site C0011.

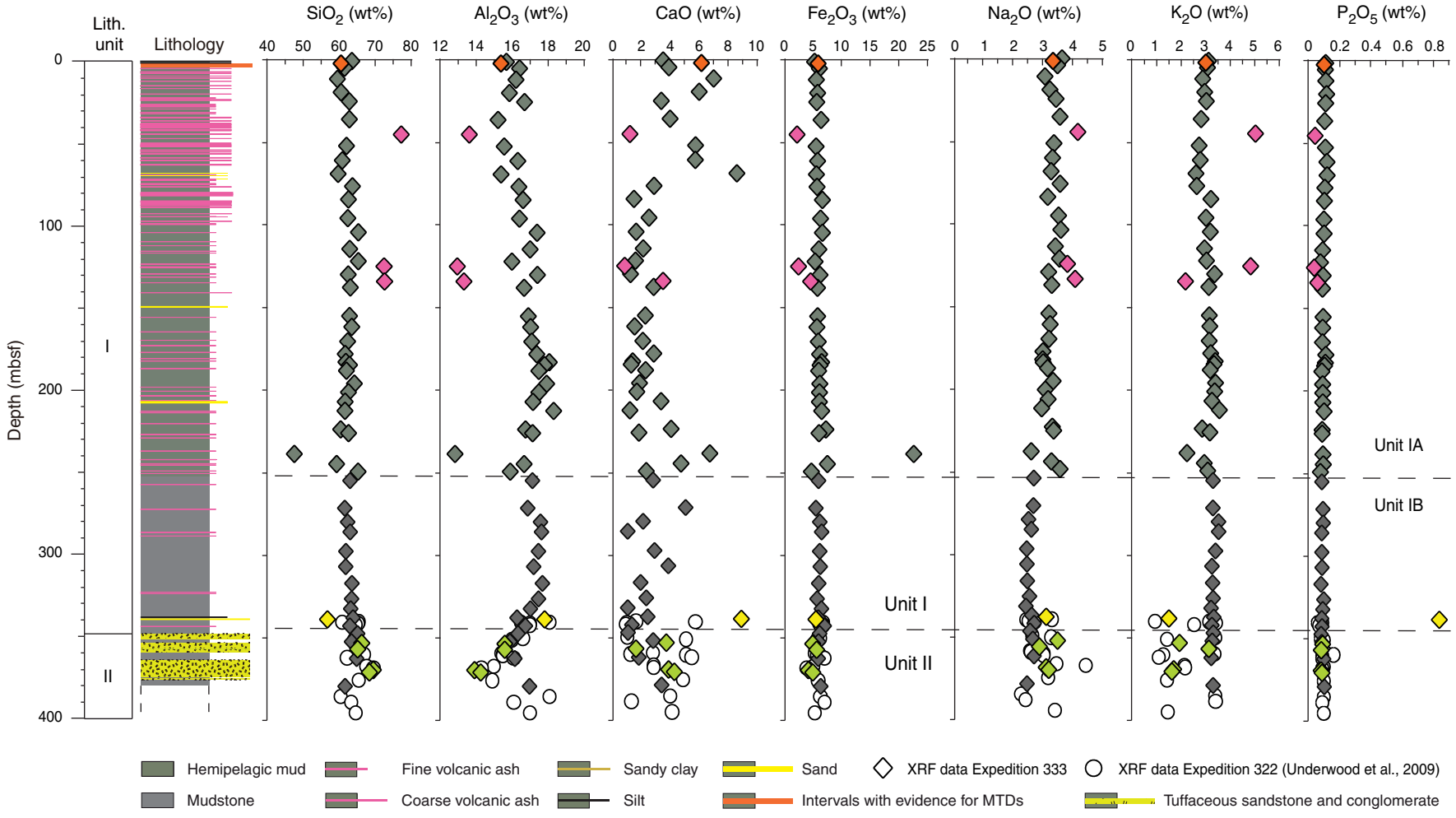

Figure F15. Distribution of bedding dip angles and deformation structures with depth, Holes C0011C and C0011D.

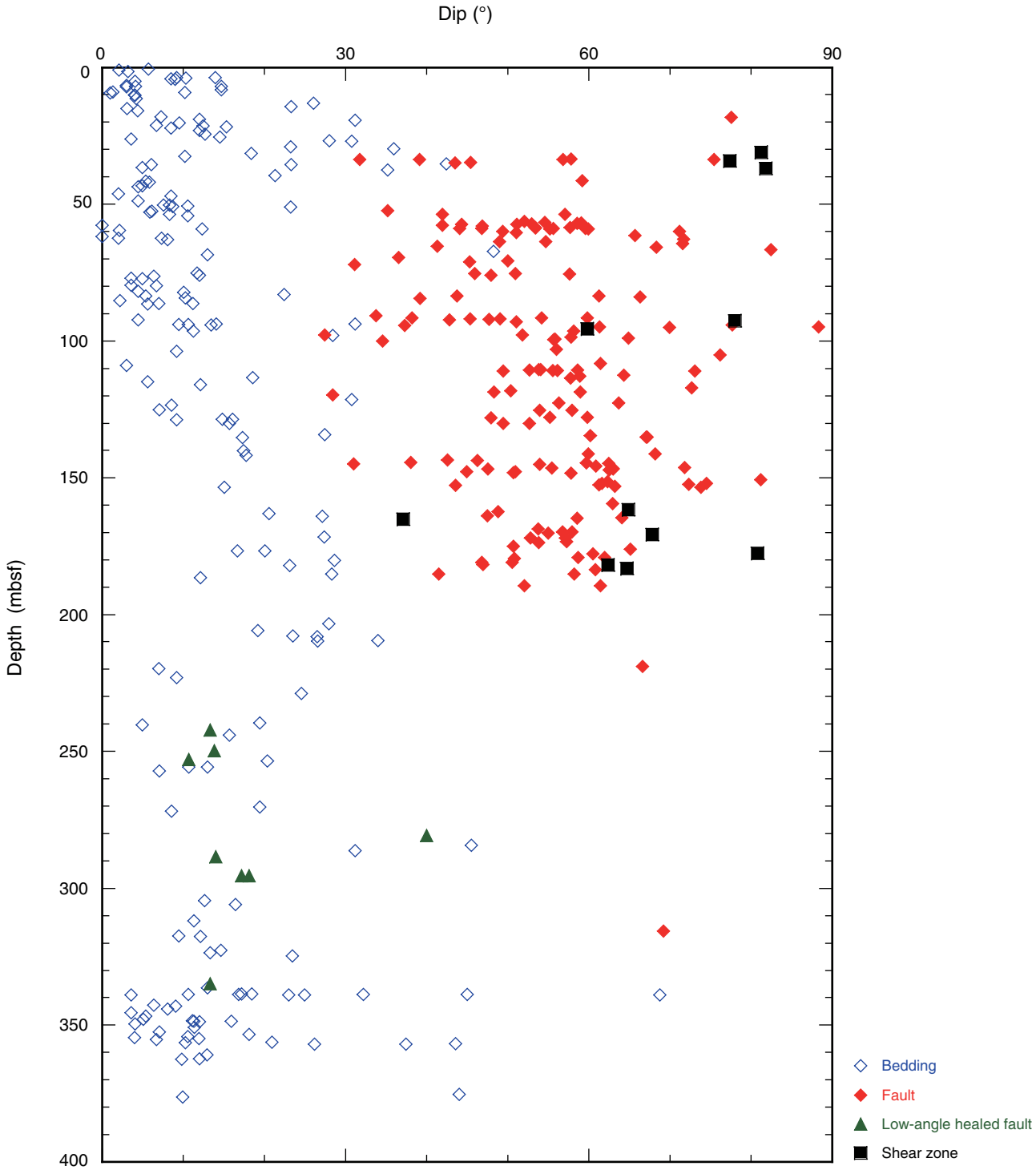

Figure F16. Lower hemisphere equal area projection of poles to bedding, Holes C0011C and C0011D. **A.** 0–100 mbsf. (Continued on next two pages.)

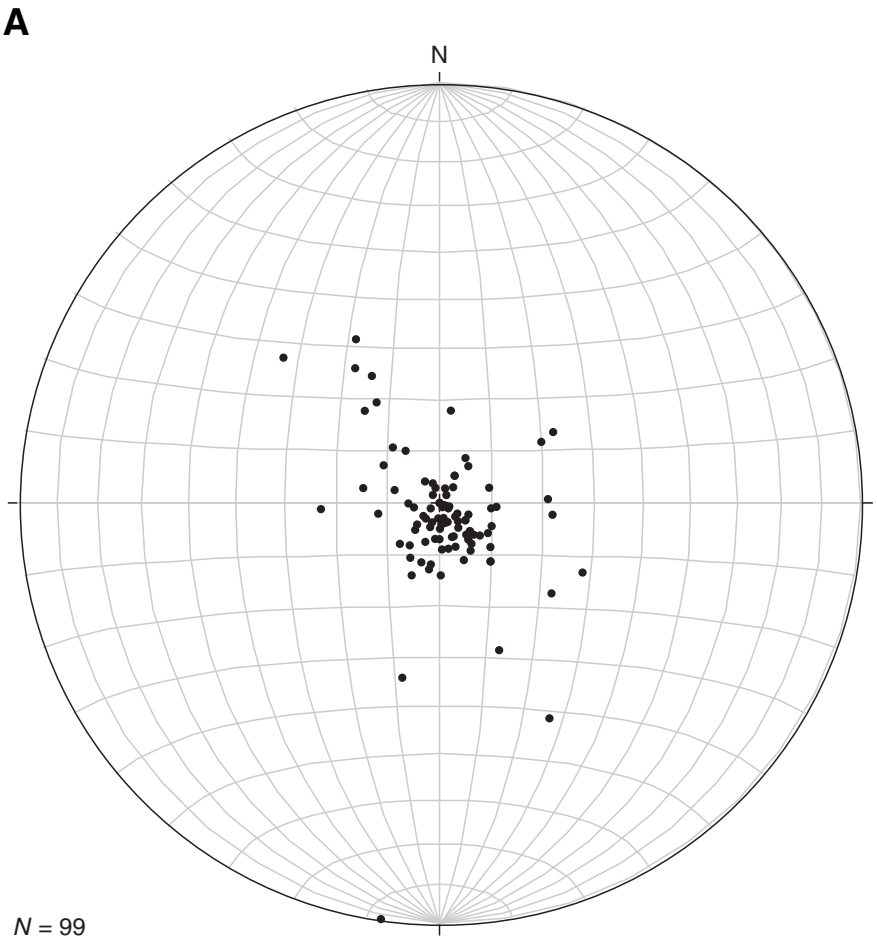

Figure F16 (continued). B. 100–251.54 mbsf. (Continued on next page.)

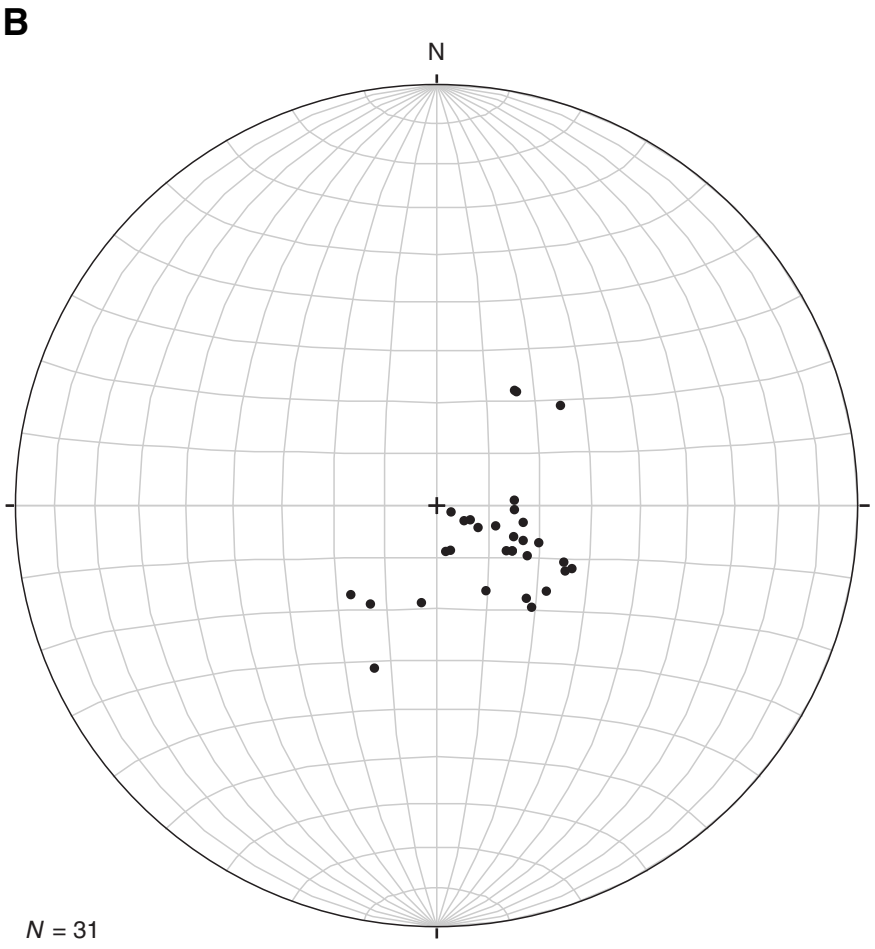

Figure F16 (continued). C. Below 251.54 mbsf.

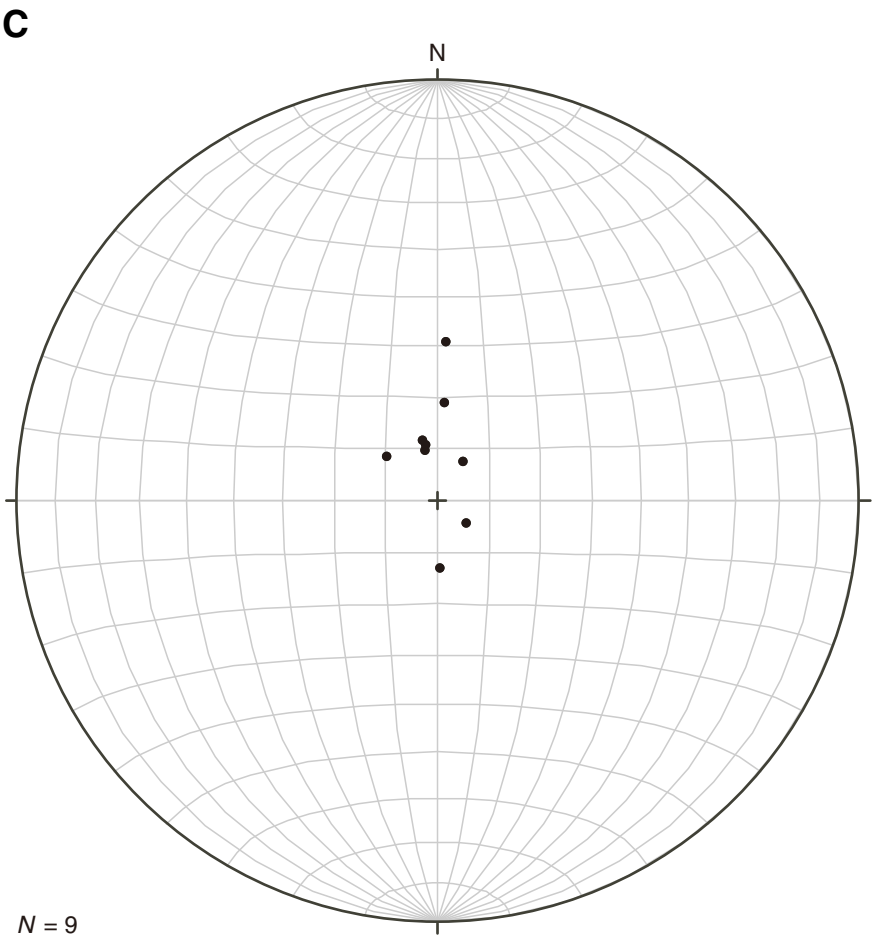

Figure F17. Conjugate set of normal faults (interval 333-C0011D-10H-8, 94–105 cm). Note that the fault offsets green layers. Offset = 7 mm and 8 mm, respectively. White arrows = the offsets of two faults. MSCL-I = photo image logger, CT = computed tomography.

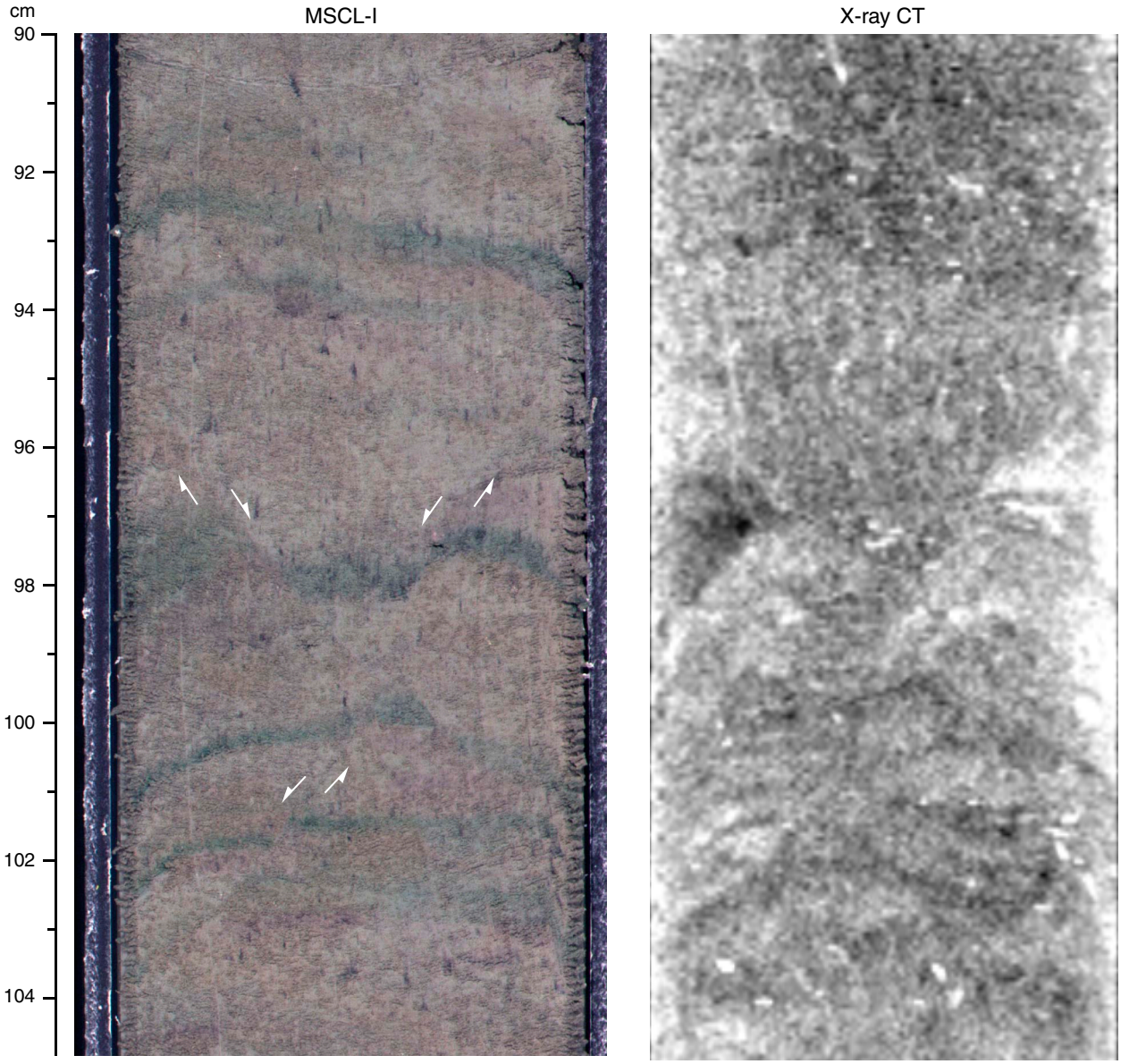

Figure F18. Lower hemisphere equal area projection of faults (great circle), Holes C0011C and C0011D.

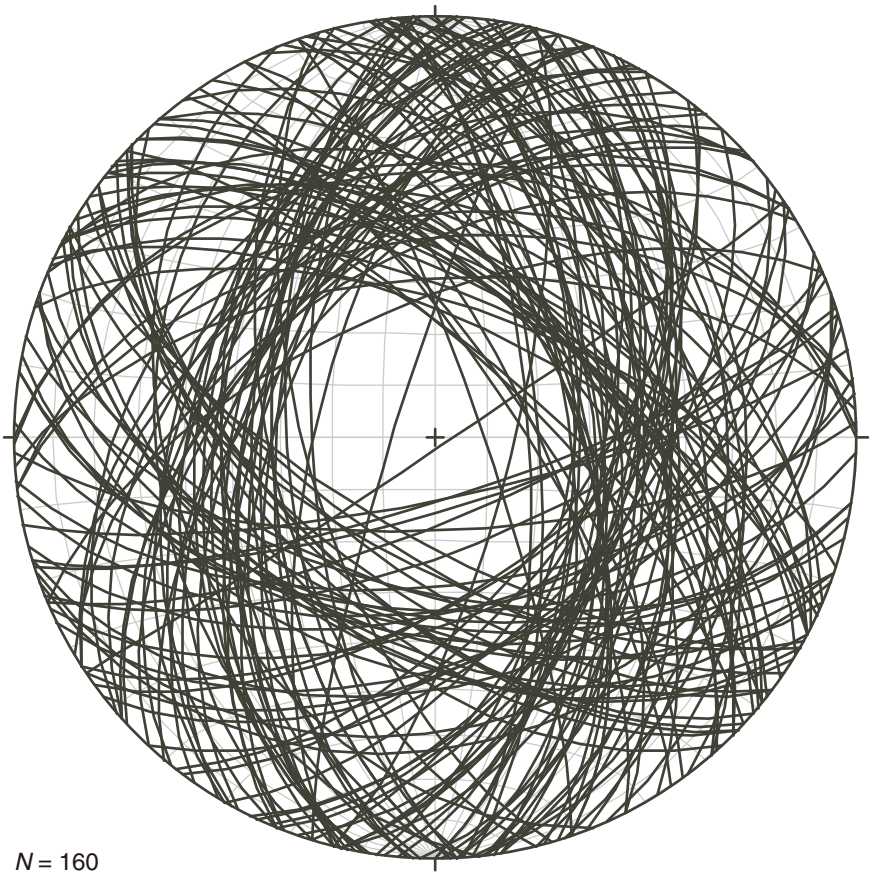

Figure F19. Appearance of low-angle healed fault (interval 333-C0011D-39X-3, 72–77 cm). Red triangles = localities of two faults. MSCL-I = photo image logger, CT = computed tomography.

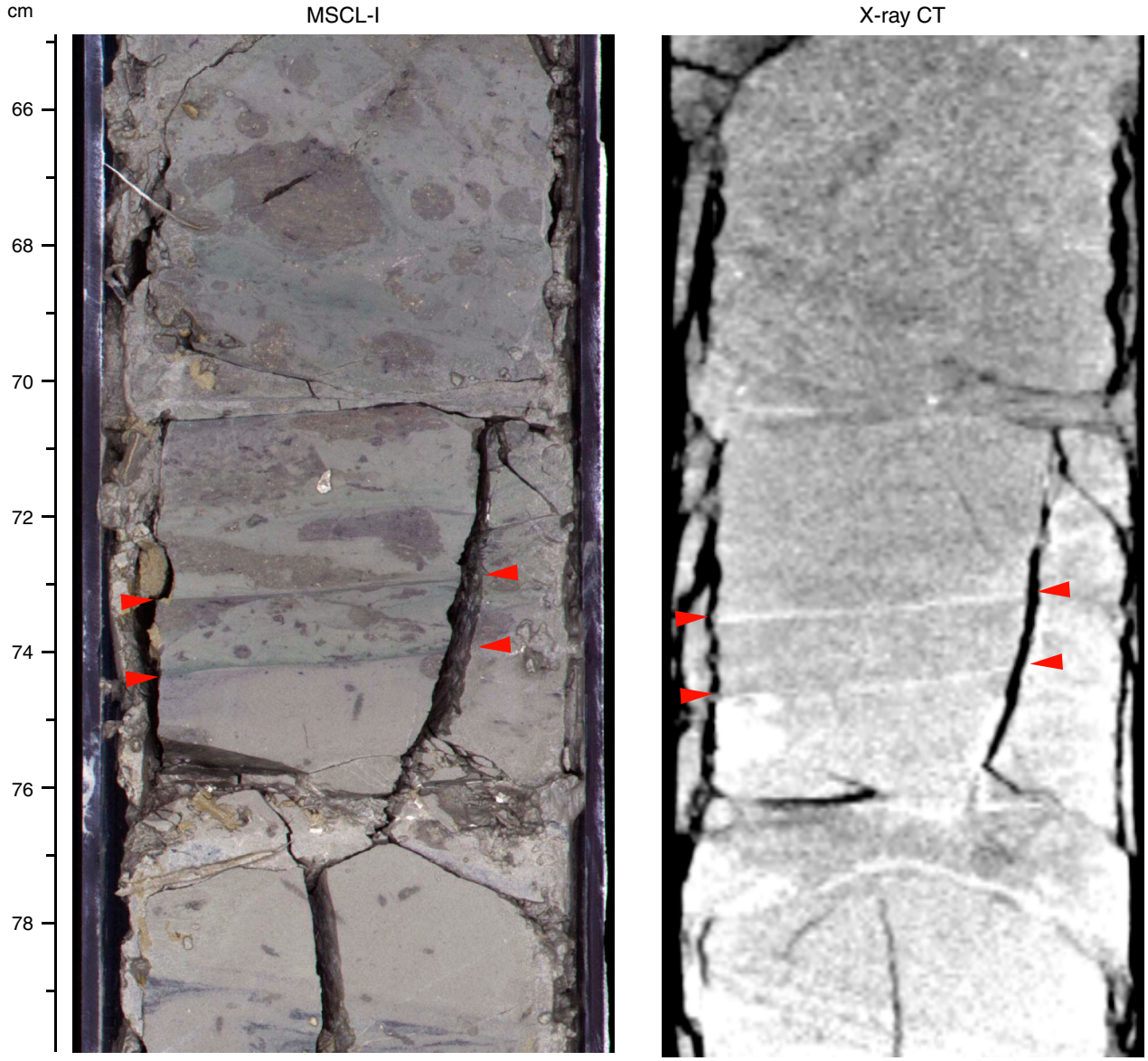

Figure F20. Lower hemisphere equal area projection of low-angle healed faults (great circle), Holes C0011C and C0011D.

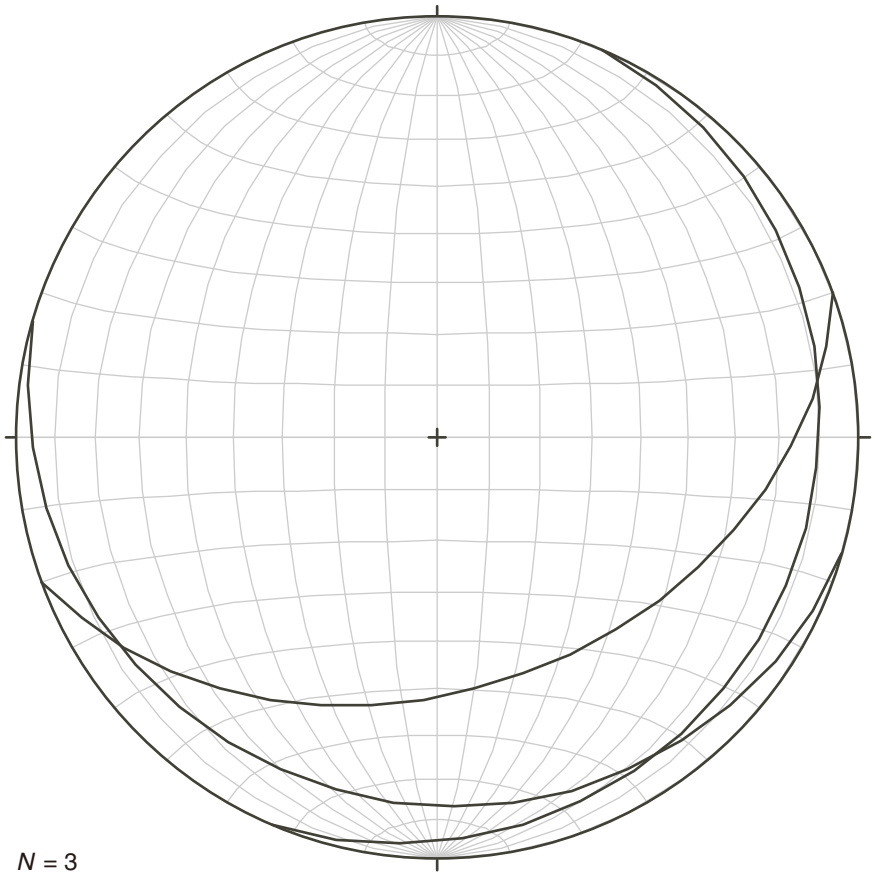

Figure F21. Appearance of shear zone (interval 333-C0011D-10H-4, 103–116 cm). MSCL-I = photo image logger, CT = computed tomography.

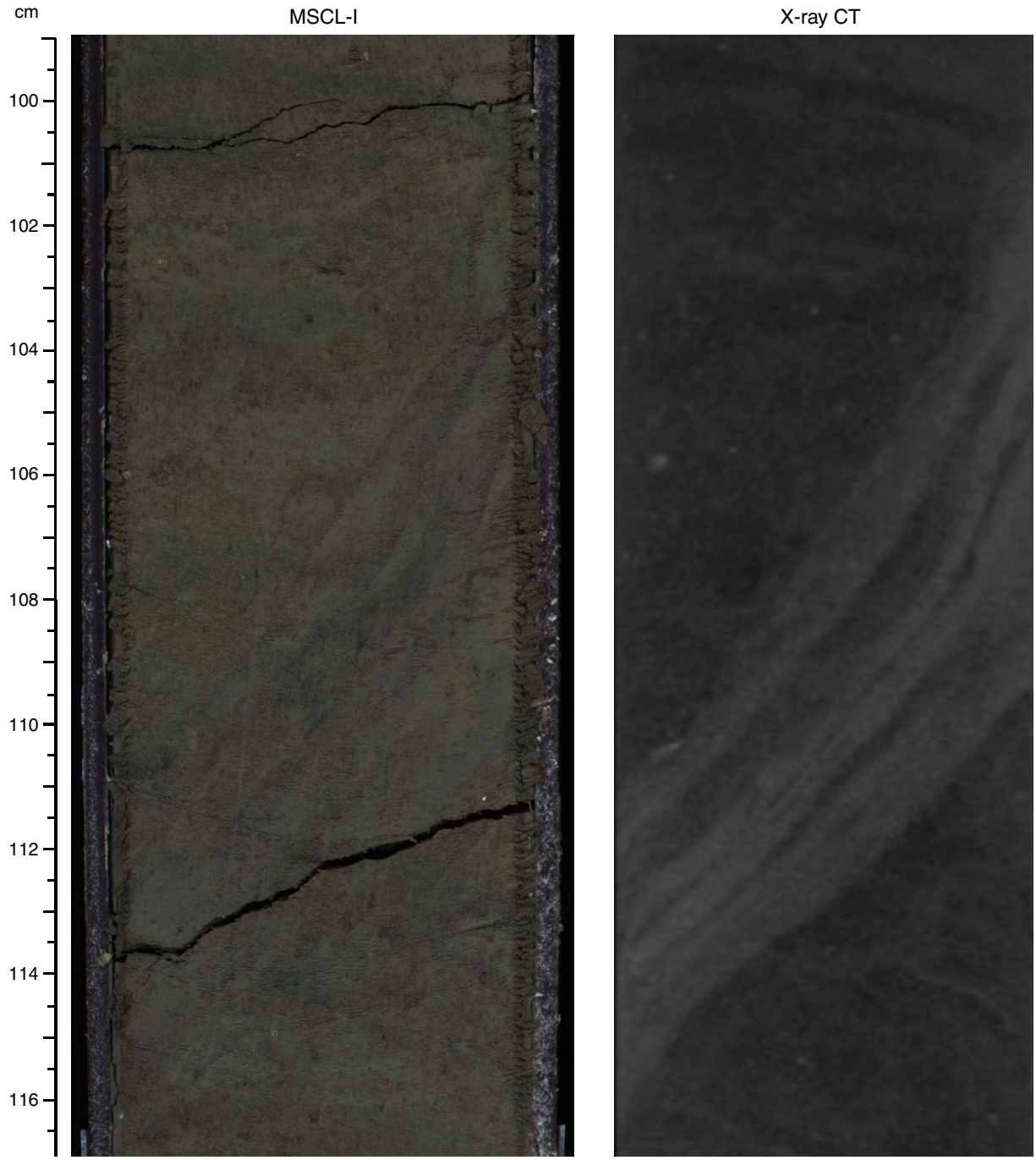

Figure F22. Lower hemisphere equal area projection of shear zones (great circle), Holes C0011C and C0011D.

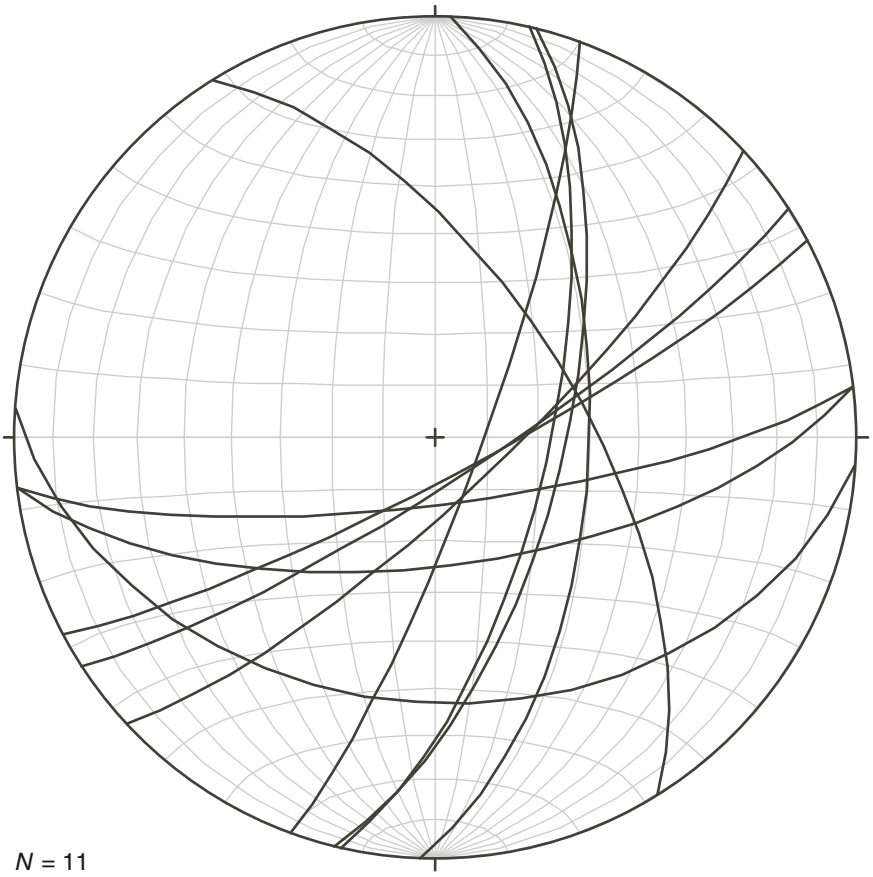

Figure F23. Appearance of sediment-filled vein (interval 333-C0011C-3H-10, 47–57 cm). Note that green bands are displaced by sediment-filled vein. MSCL-I = photo image logger, CT = computed tomography.

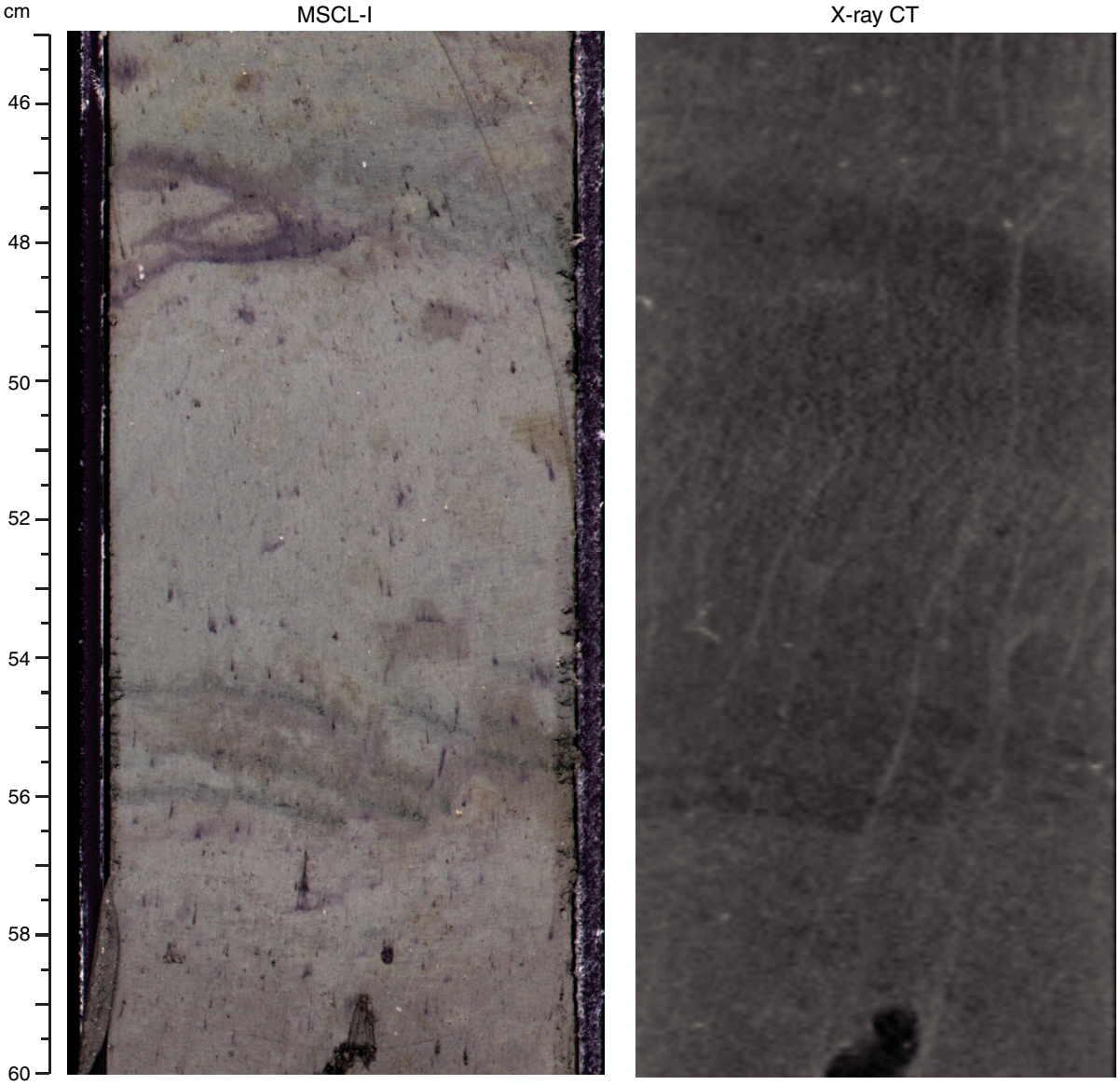

Figure F24. Appearance of mineral vein (interval 333-C0011D-41X-6, 91 cm). Red rectangle = locality of mineral vein.

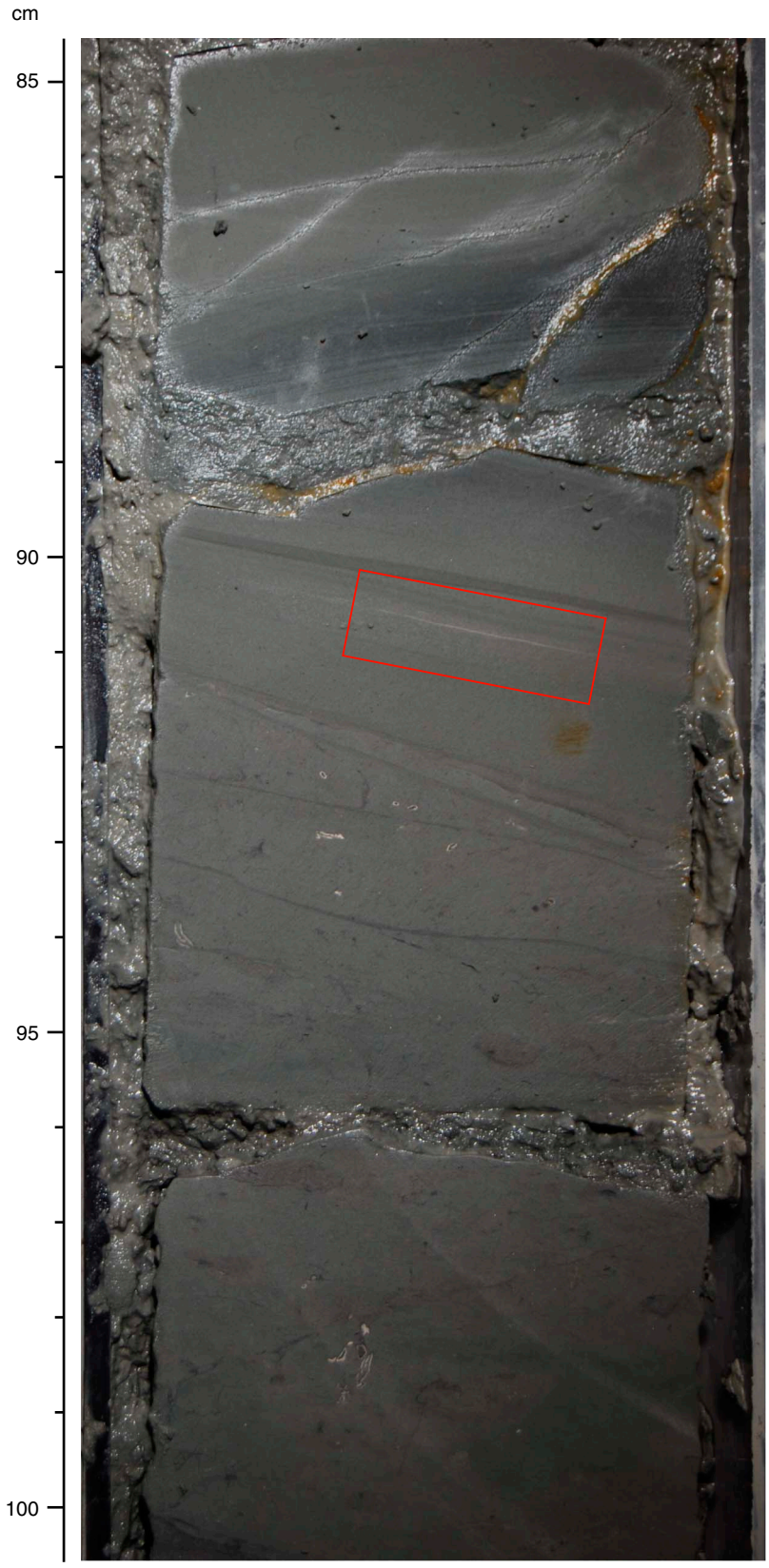

Figure F25. Age-depth plot for Holes C0011C and C0011D showing nannofossil datums, paleomagnetic events, and volcanic marker events. Sedimentation rates (in cm/k.y.) are indicated in the curve.

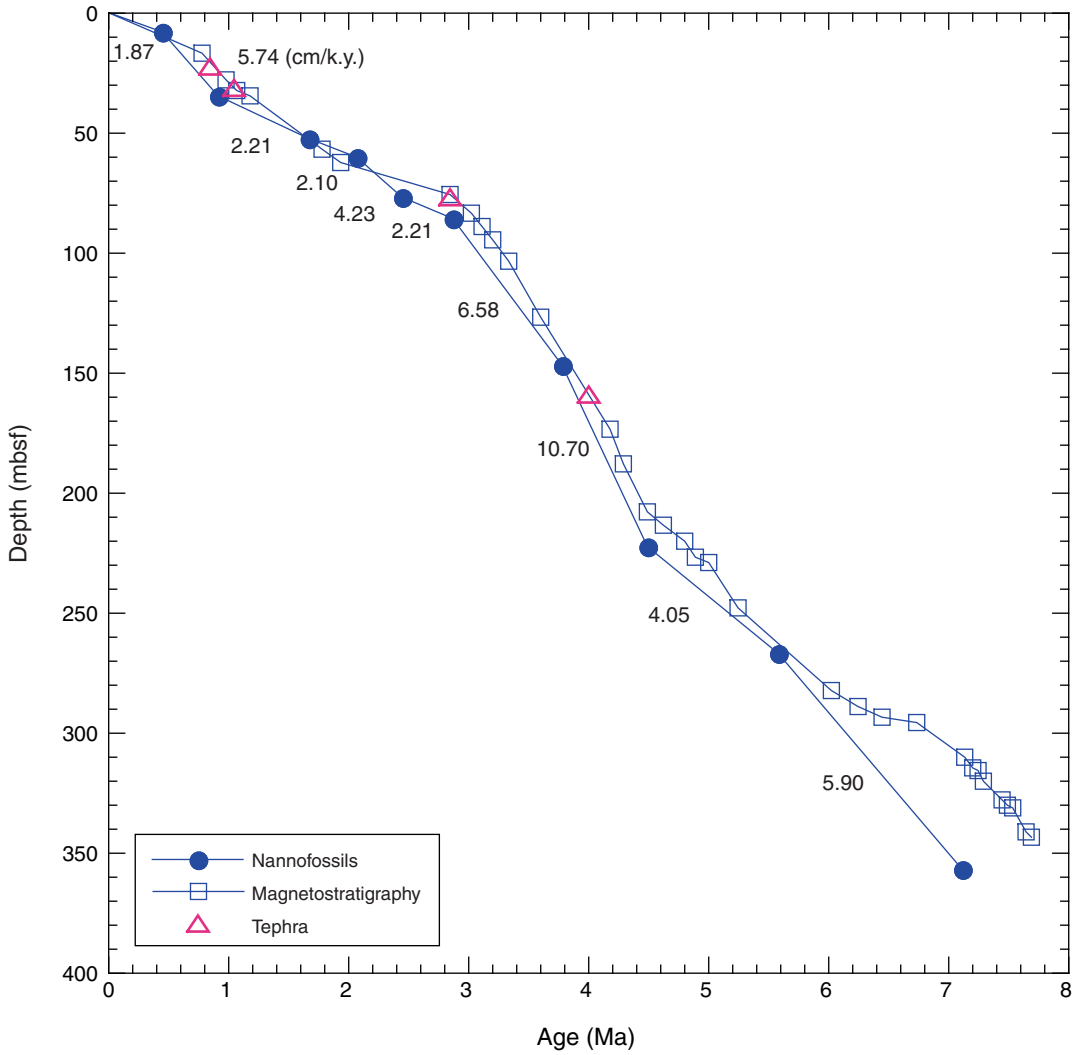

Figure F26. Magnetic susceptibility and remanent magnetization before and after 30 mT AF demagnetization, Site C0011. Green = natural remanent magnetization (NRM), blue = 30 mT AF demagnetization, red = remanent magnetization after 400°C thermal demagnetization.

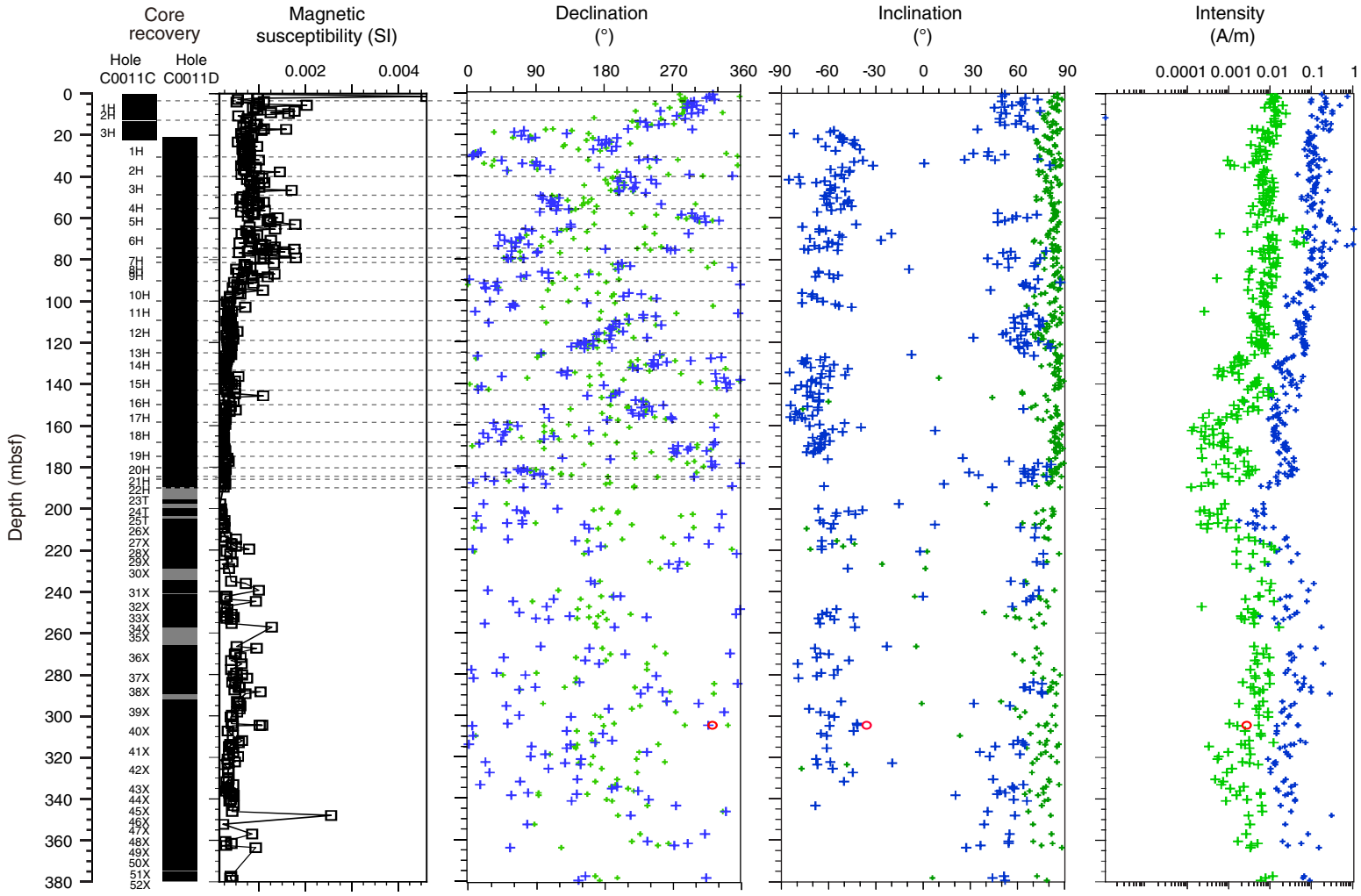

Figure F27. Zijderveld diagrams (Zijderveld, 1967) and Schmidt nets (in the lower hemisphere). **A.** Natural remanent magnetization (NRM) and remanent magnetization after 5, 10, 20, 30, and 40 mT AF demagnetization at 30.001 mbsf (Sample 333-C0011D-1H-9, 88–90 cm). **B.** NRM and remanent magnetization after 100°, 200°, 300°, 400°, 450°, 500°, 550°, and 600°C thermal demagnetization at 306.69 mbsf (interval 333-C0011D-40X-3, 37–39 cm). On the Zijderveld diagram, open circles = inclination, solid circles = declination. In particular, angles of the inclination decrease from NRM to remanent magnetization after 40 mT AF demagnetization, indicating drilling-induced magnetization. On the Schmidt nets, open circles = upward plots, solid circles = downward plots.

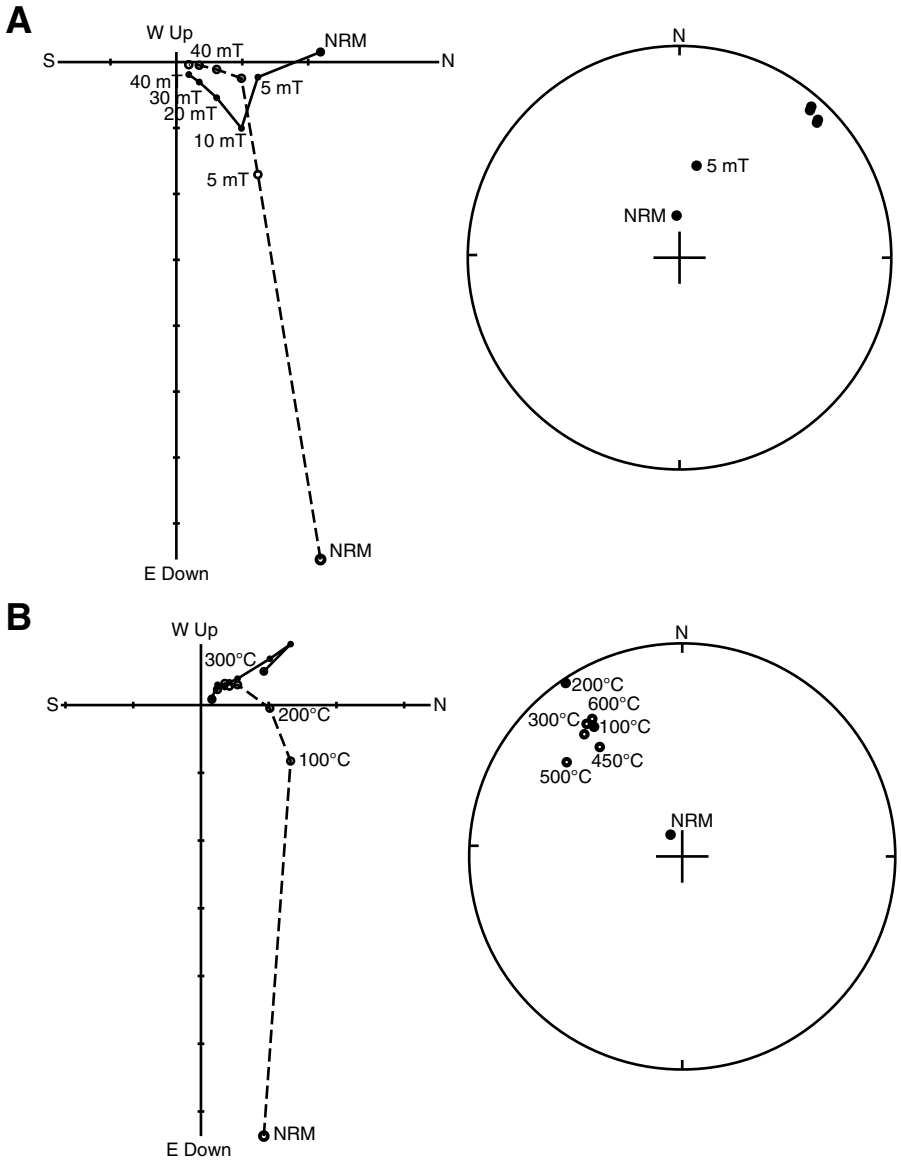

Figure F28. Downhole variation in stable magnetic inclination demagnetized at 30 mT, inferred polarity, and tephra chronological age for sediments, Site C0011. Black = normal polarity, white = reversed polarity, pink lines = volcanic ash beds. No interpretation provided for shaded areas.

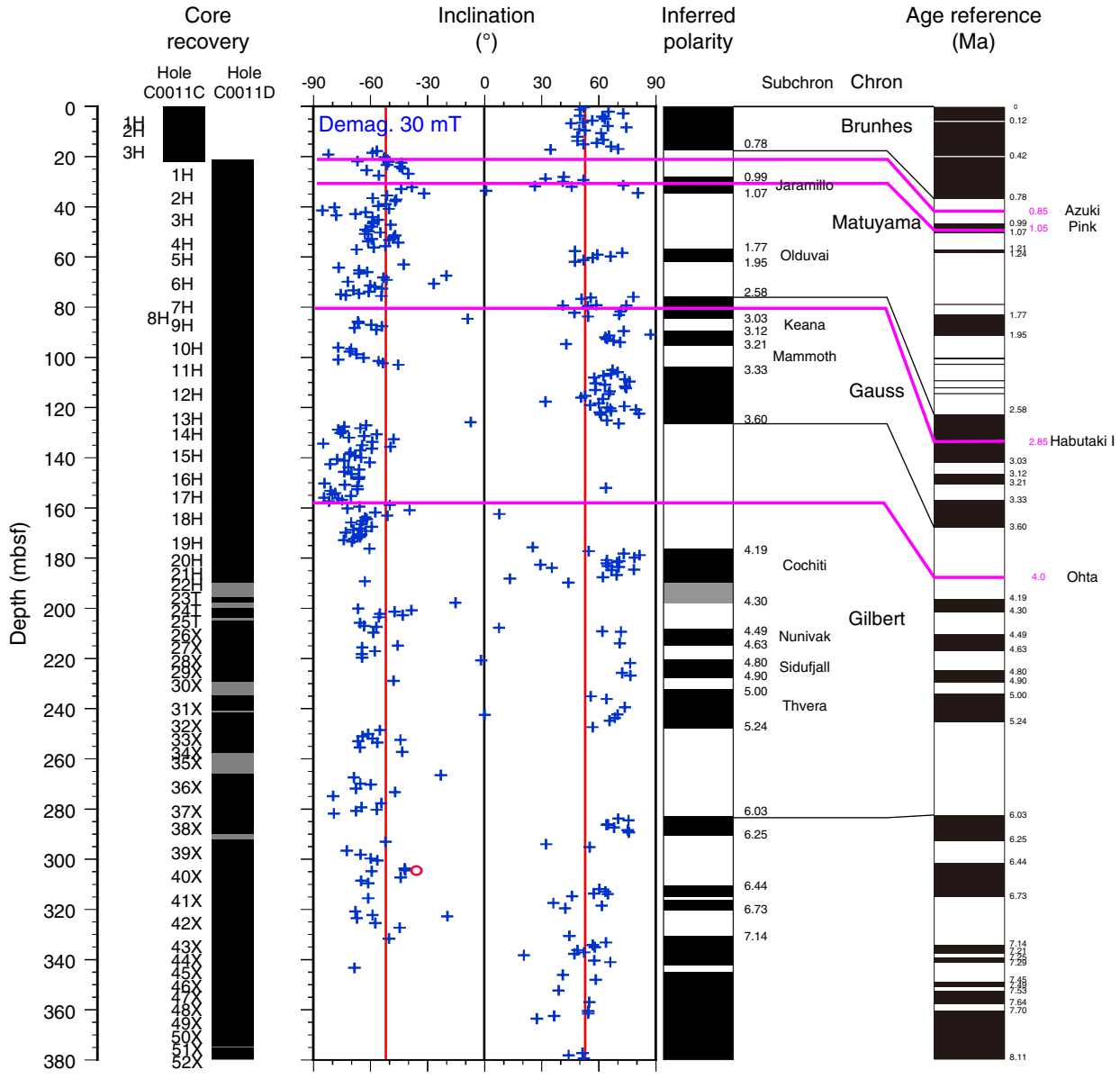

Figure F29. Diagram of burial depth vs. geologic age, indicating sedimentation rate throughout Holes C0011C and C0011D. Average sedimentation rate (uncorrected for compaction) = ~4.63 cm/k.y.

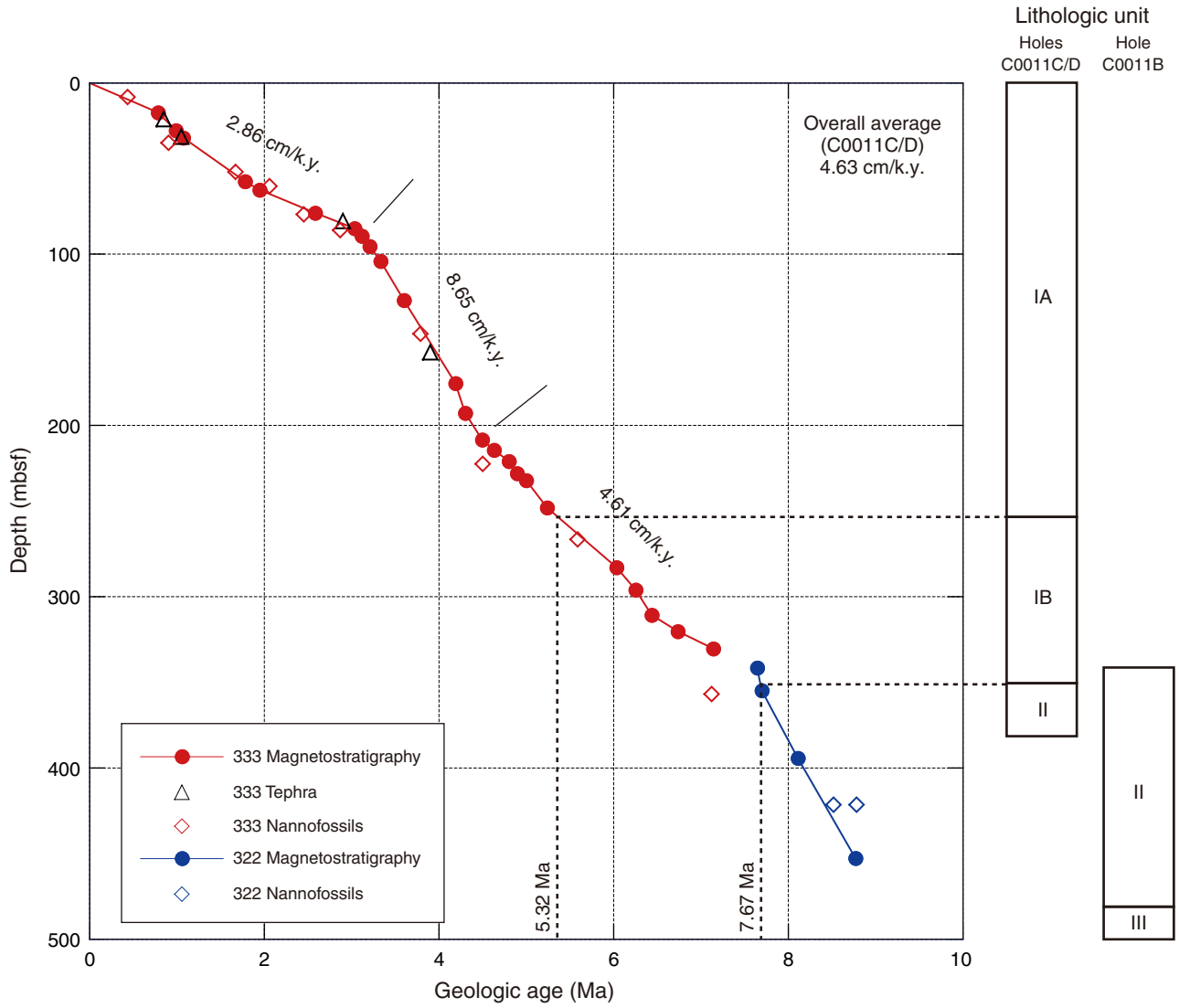

Figure F30. Site C0011 gamma ray attenuation (GRA) density, magnetic susceptibility, noncontact electrical resistivity, and natural gamma radiation determined by MSCL-W; gamma ray from logging-while-drilling (LWD) data. LWD ring resistivity is plotted with MSCL resistivity. CMS = corrected volume magnetic susceptibility, cps = counts per second, dashed lines = Expedition 322 Site C0011 logging units, black = Hole C0011C/C0011D, red = Expedition 322 Hole C0011B.

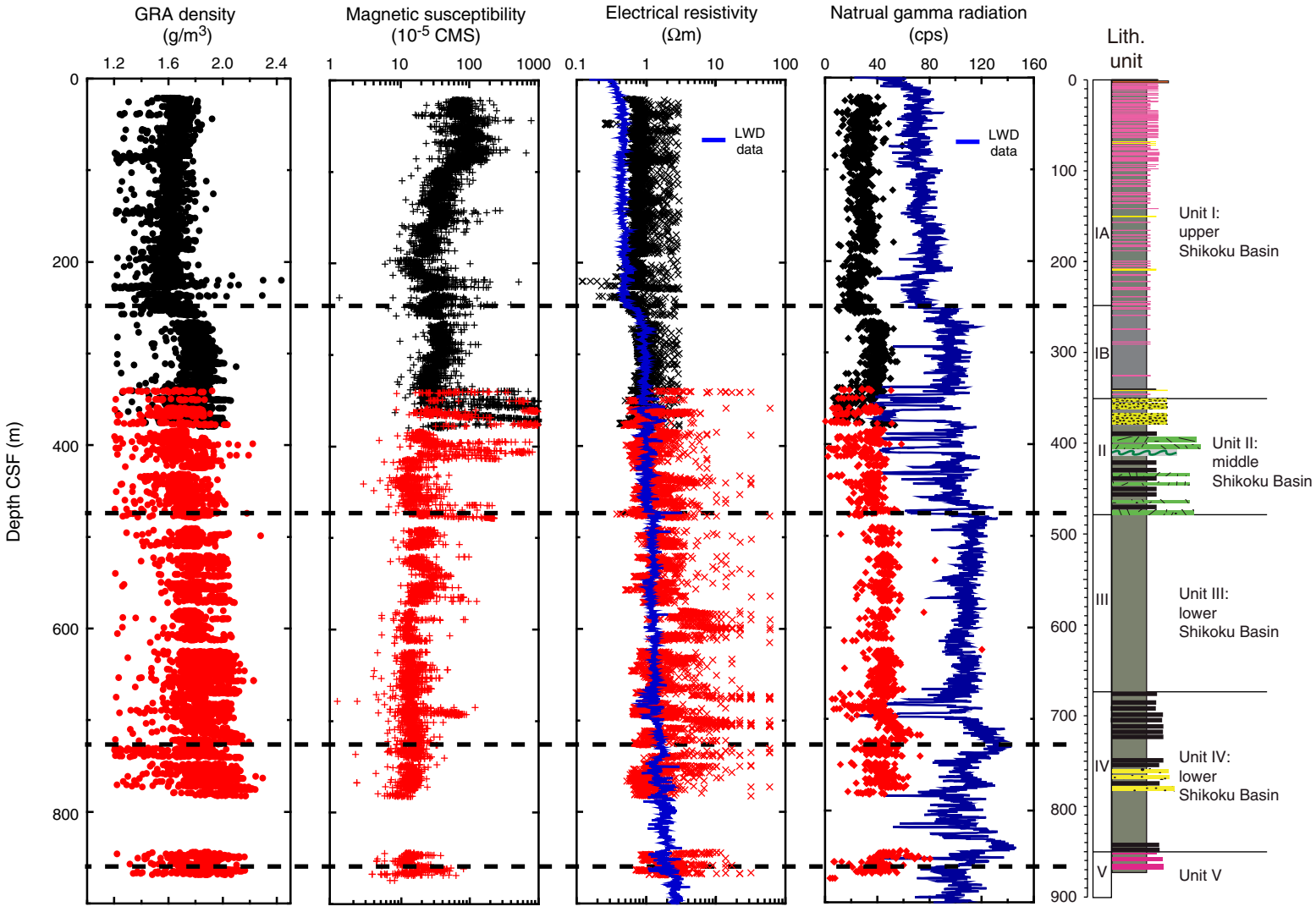

Figure F31. Bulk density, porosity, and grain density data, Site C0011. Red = noted sand or ash samples, filled symbols = Hole C0011C/C0011D, open symbols = Expedition 322 Hole C0011B.

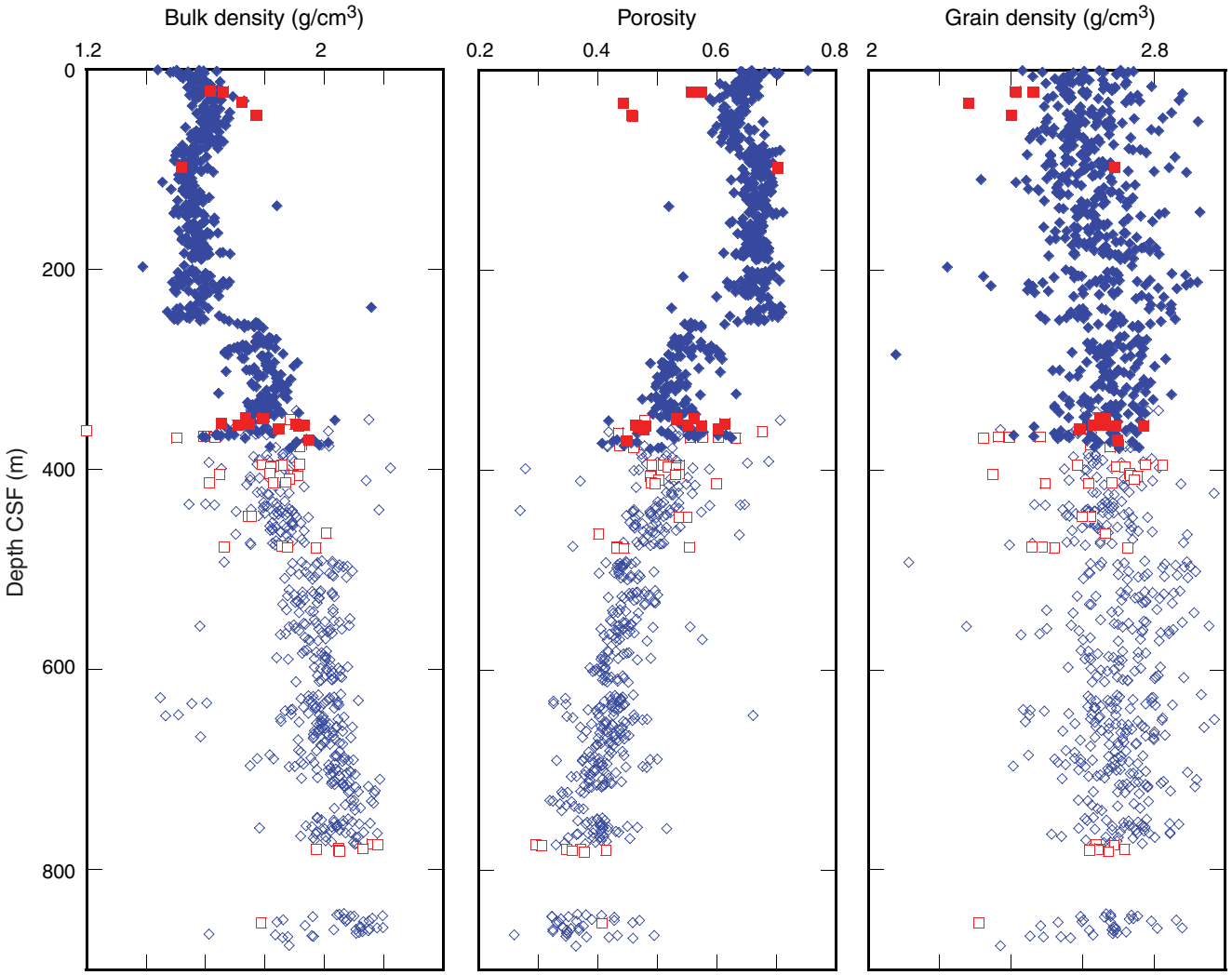

Figure F32. Porosity data from Site C0011 shown with porosity data from ODP Muroto transect Site 1173 and ODP Ashizuri transect Site 1177. At Site 1177, the full profile is not available because coring began at 300 mbsf (Moore et al., 2001).

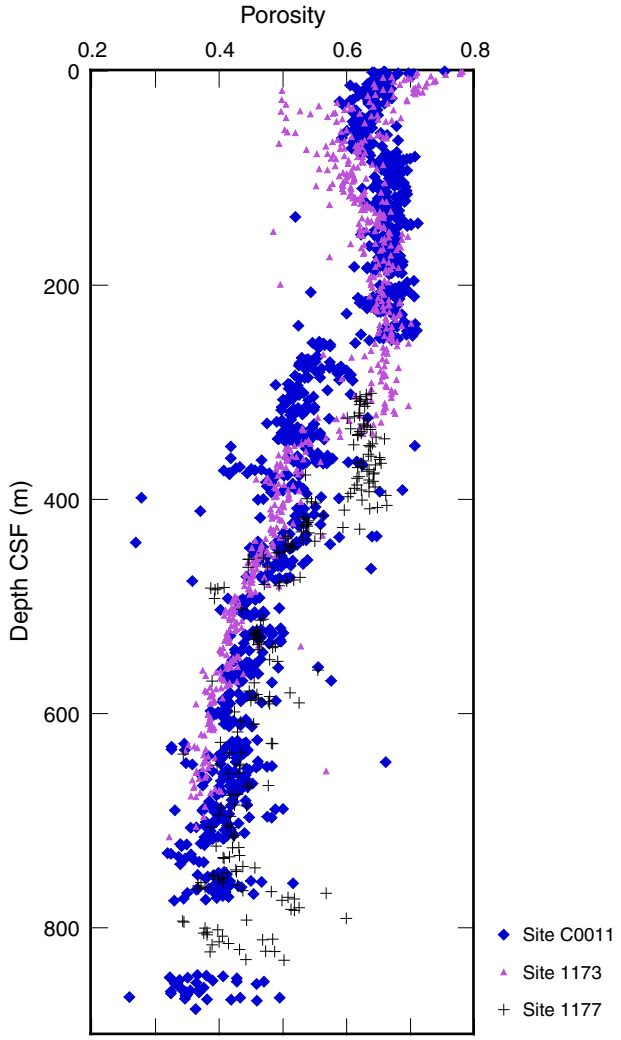

Figure F33. Penetrometer and vane shear measurements from Site C0011 plotted with porosity from MAD measurements and lithologic units.

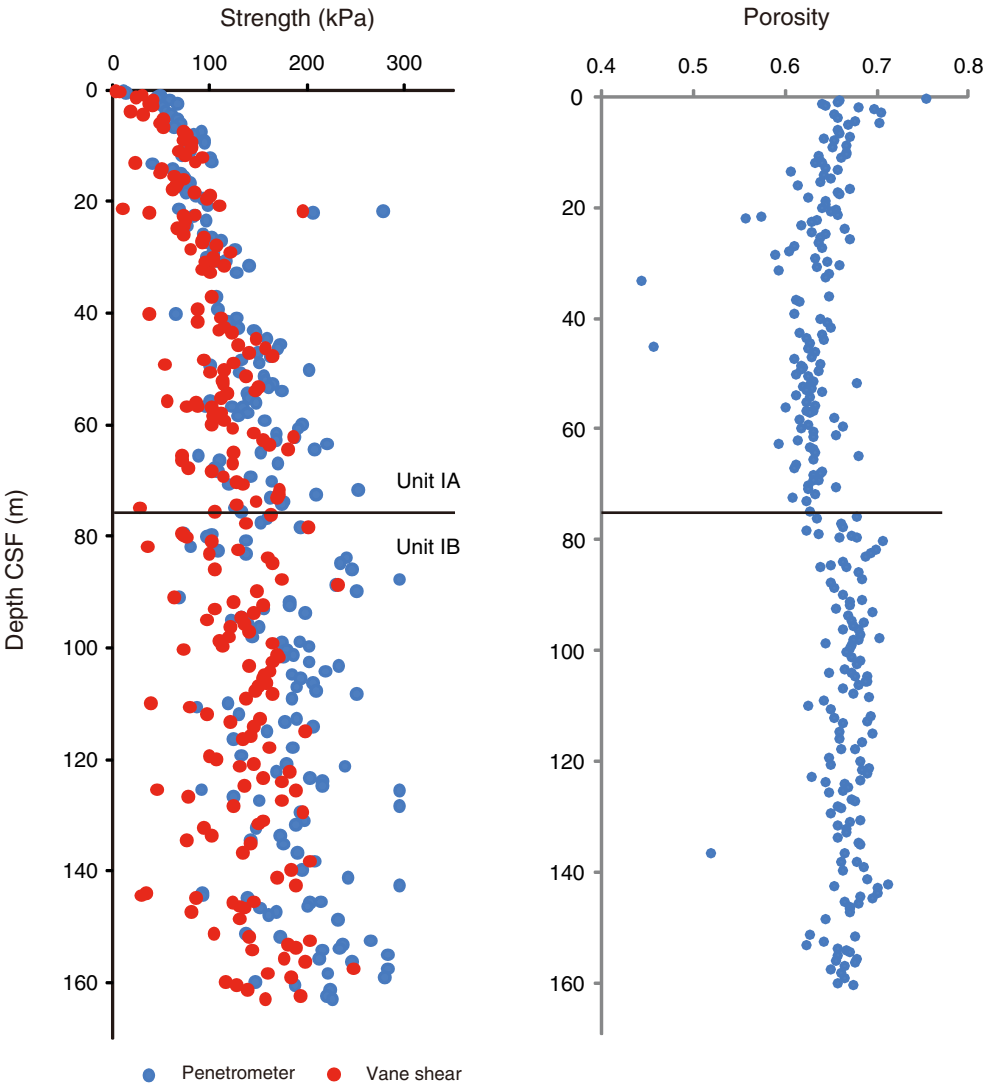

Figure F34. A. *P*-wave velocity. **B.** Vertical-plane anisotropy. Red = Hole C0011D, blue = Expedition 322 Hole C0011B.

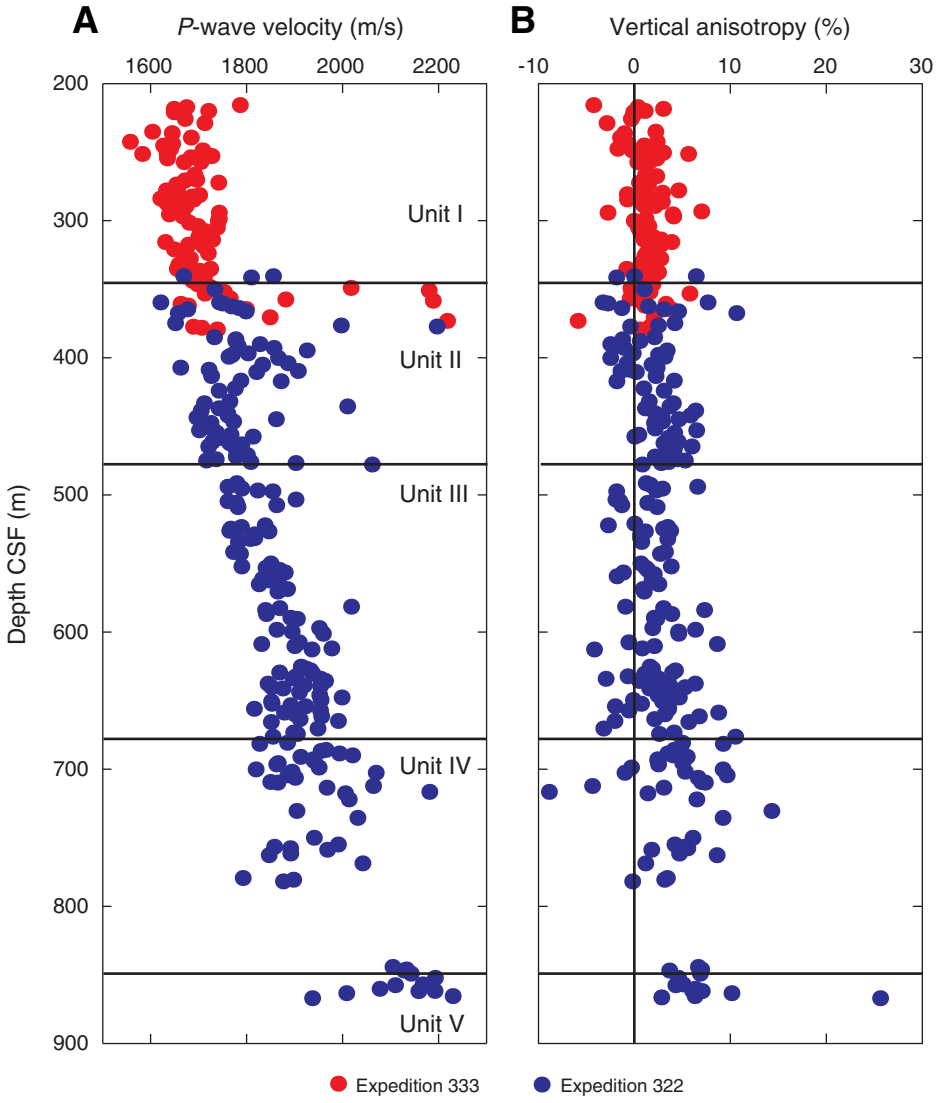

Figure F35. Velocity-porosity data with empirical trends. Red = Hole C0011D, blue = Expedition 322 Hole C0011B.

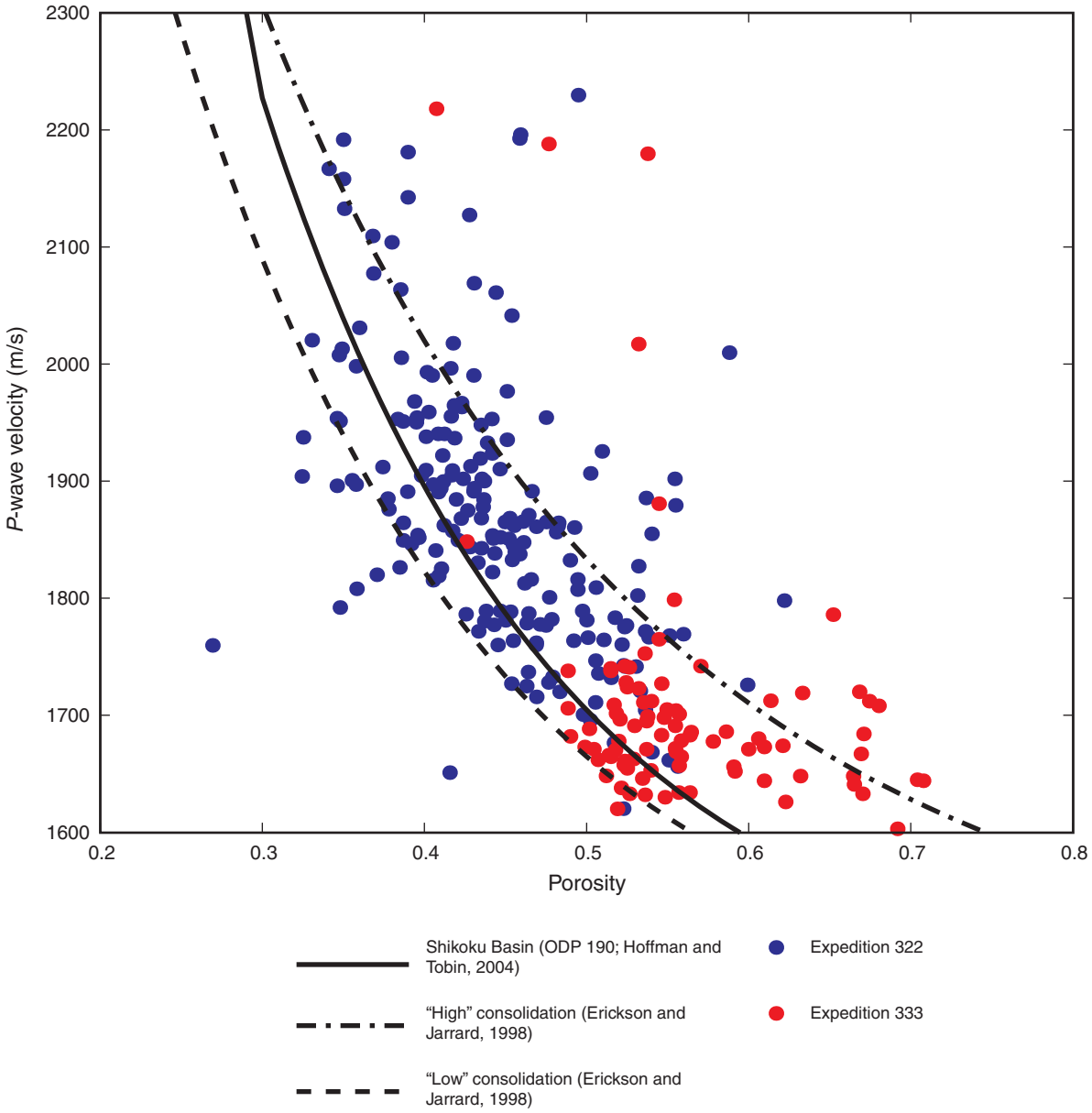

Figure F36. Resistivity measurements made on split sections from Site C0011 plotted with whole-round multisensor core logger (MSCL-W) resistivity and porosity from MAD measurements. Dashed lines = Expedition 322 Site C0011 logging units, black = Hole C0011C/C0011D, red = Expedition 322 Hole C0011B.

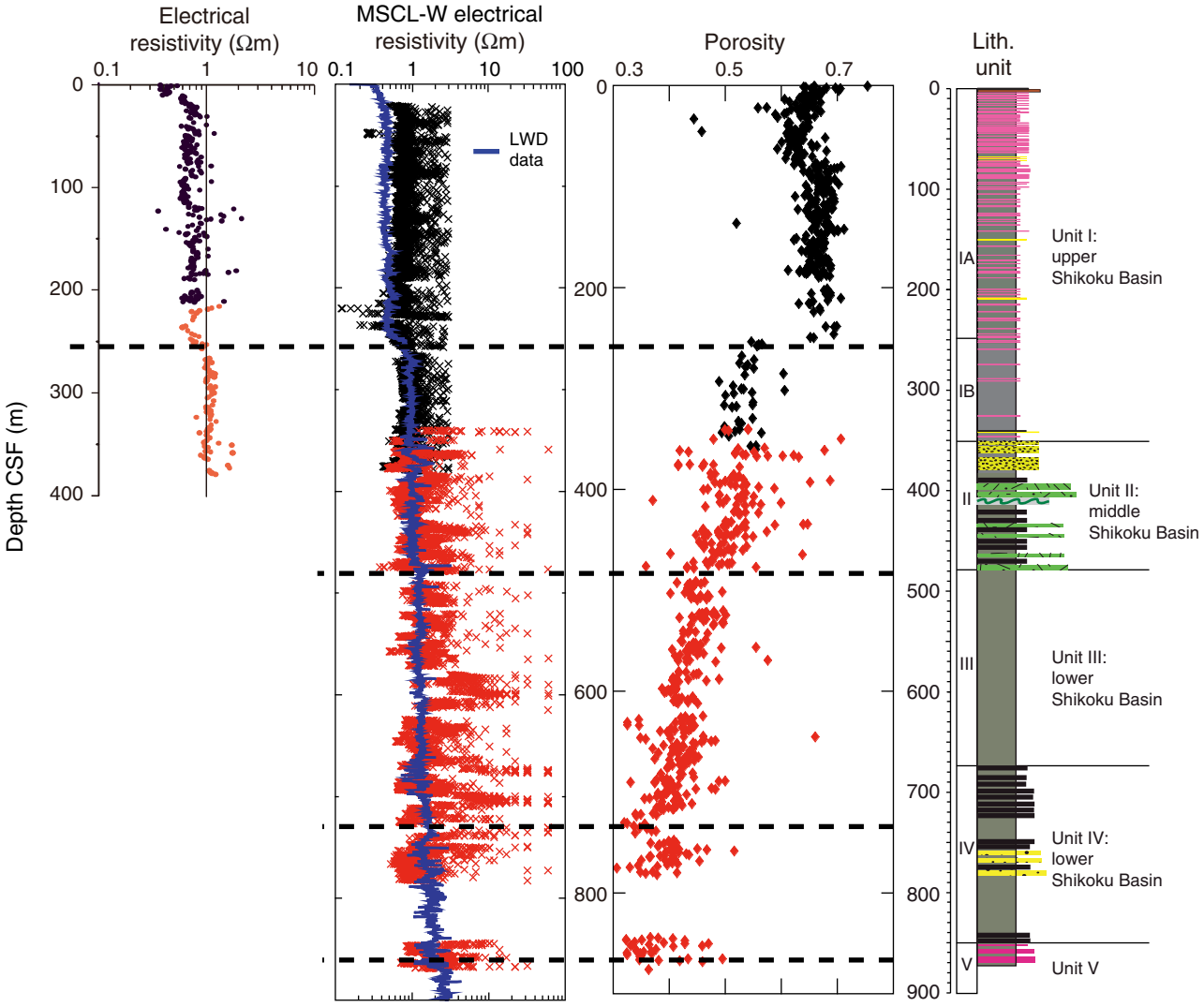

Figure F37. A. Electrical resistivity. **B.** Vertical-plane anisotropy. Red = Hole C0011D, blue = Expedition 322 Hole C0011B.

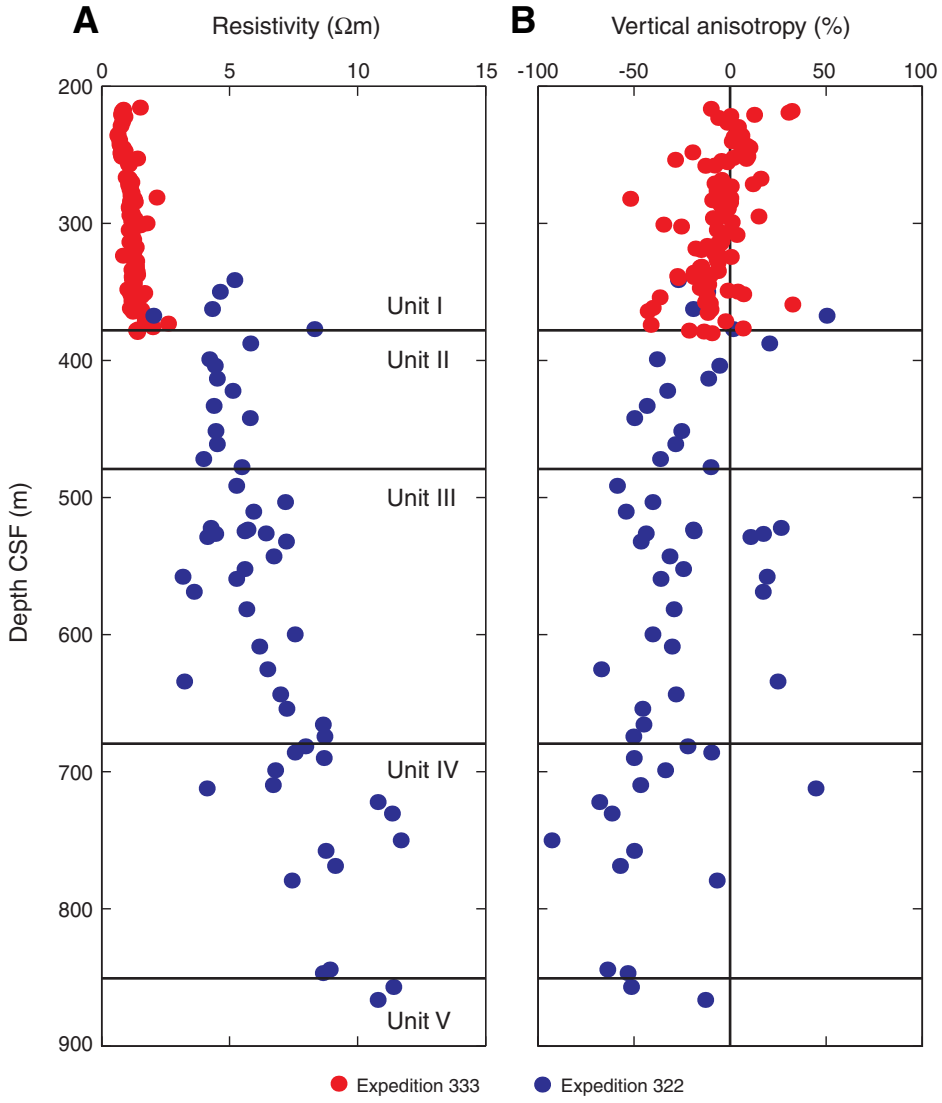

Figure F38. Log-log plot of porosity and resistivity, Holes C0011C and C0011D. Red = data from zone of anomalously high porosity from 80 to 240 m CSF.

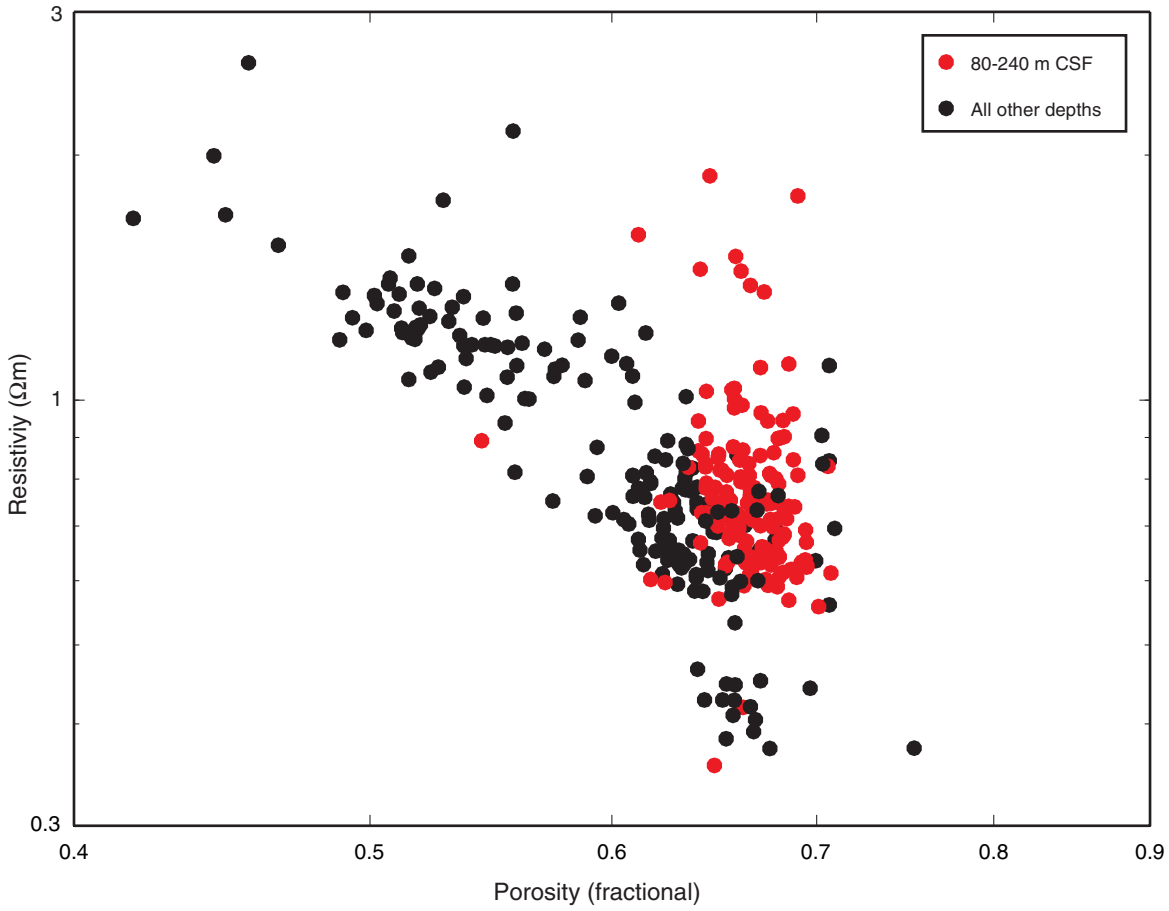

Figure F39. Temperatures measured using APCT-3, Hole C0011D. Least squares fit yields an average thermal gradient of 91.3°C/km and an intercept of 1.7°C at the seafloor.

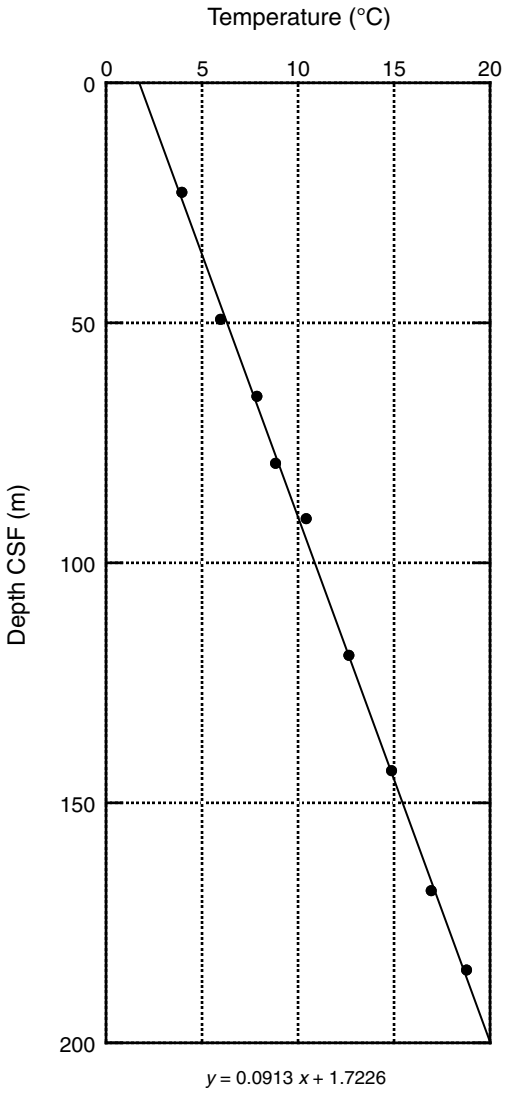

Figure F40. Thermal conductivity as a function of depth, Hole C0011D.

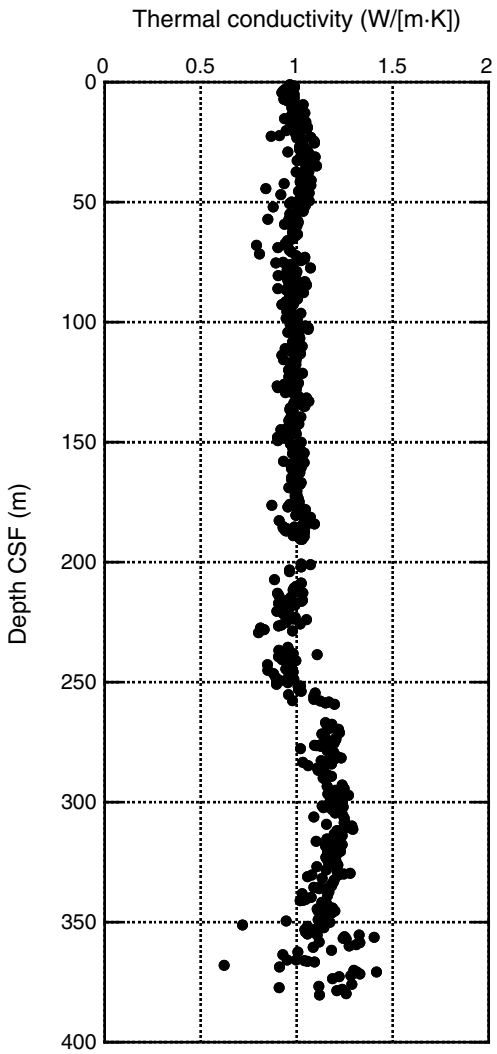

Figure F41. Temperatures estimated by the Bullard method, Site C0011. Red = measured temperatures. Estimated temperature at the basement is 79°C.

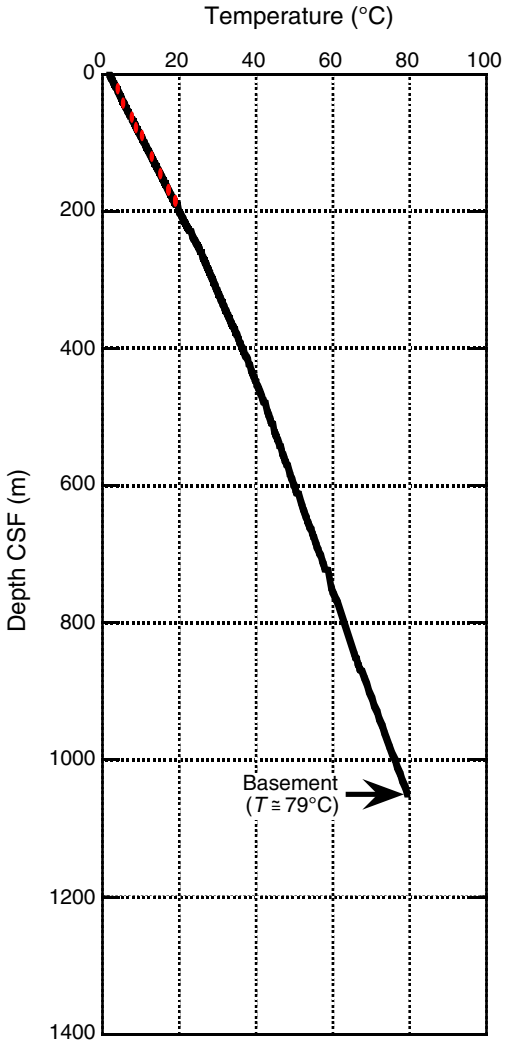

Figure F42. A. Volume of interstitial water (IW) recovered per length of IW whole-round section (mL/cm). Red = Holes C0011C and C0011D, blue = Expedition 322 Hole C0011B (see fig. F55 in Expedition 322 Scientists, 2010). **B.** Dissolved sulfate profile, used to estimate the (**C**) percent contamination values in drilling disturbed cores. Red = EPCS and ESCS in Holes C0011C and C0011D, blue = HPCS in Expedition 322 Hole C0011B (see table T17 in Expedition 322 Scientists, 2010).

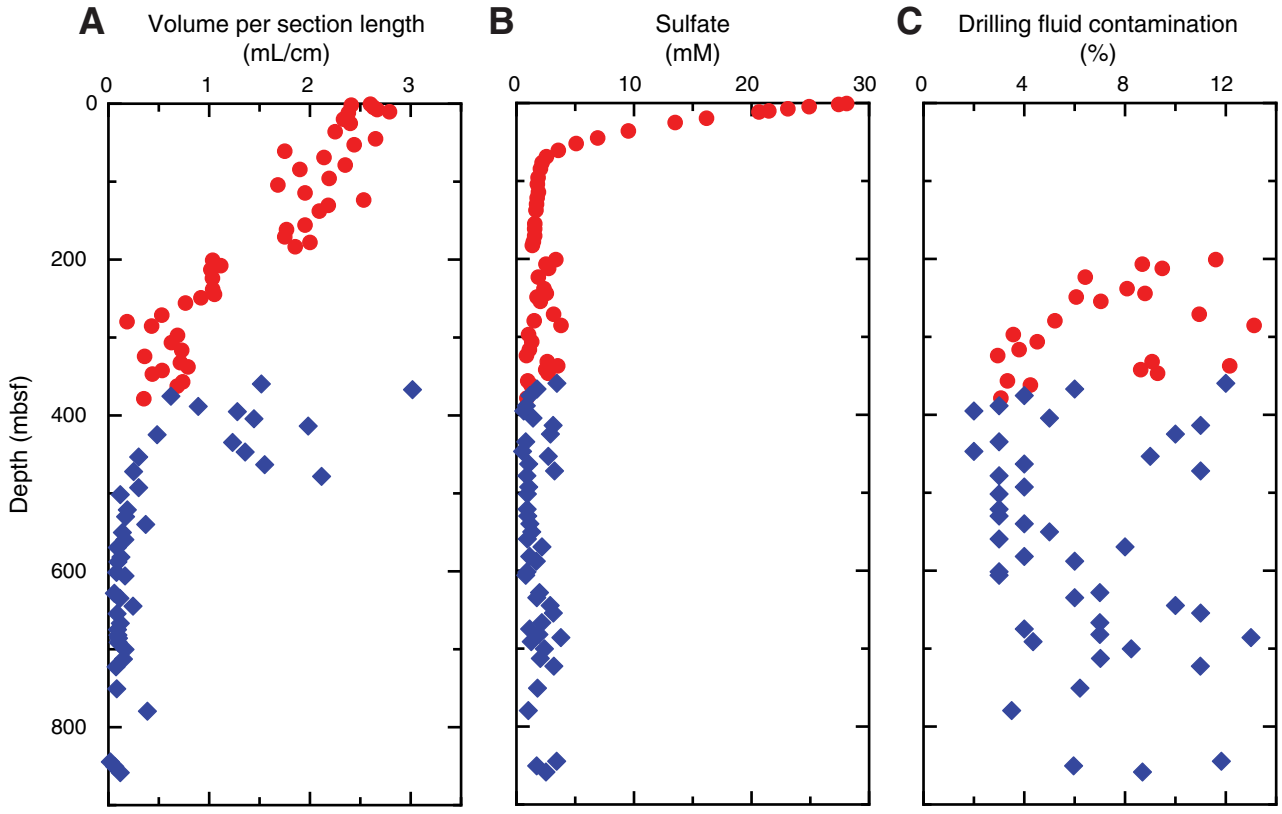

Figure F43. Interstitial water constituents (salinity, chlorinity, bromide, pH, alkalinity, sodium, ammonium, phosphate, Br/Cl, and boron). Red = Holes C0011C and C0011D (Table T13), blue = Expedition 322 Hole C0011B (see table T18 in Expedition 322 Scientists, 2010).

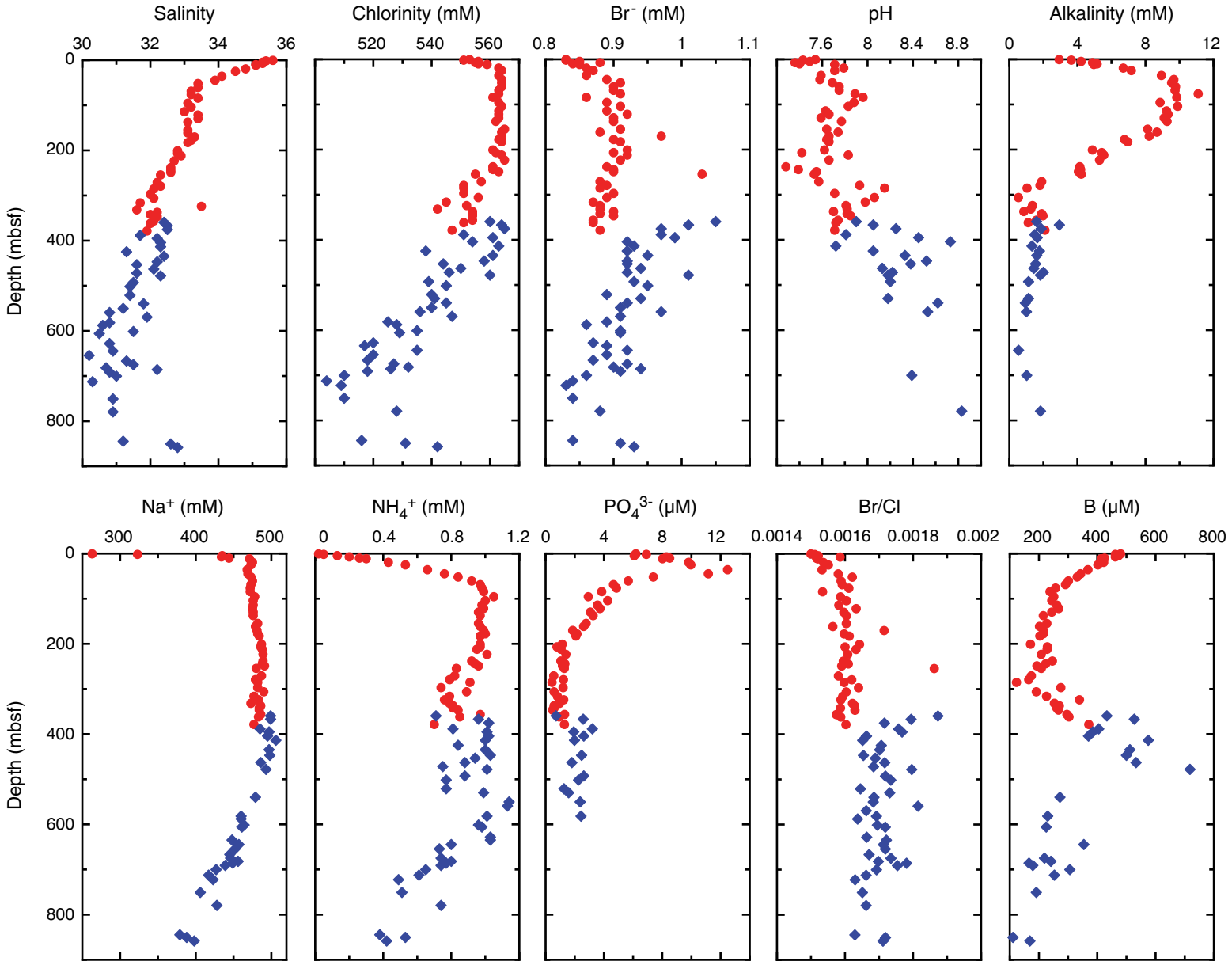

Figure F44. Interstitial water constituents (potassium, magnesium, calcium, Ca/Mg, silica, iron, lithium, strontium, barium, and manganese). Red = Holes C0011C and C0011D (Table T13), blue = Expedition 322 Hole C0011B (see table T18 in Expedition 322 Scientists, 2010).

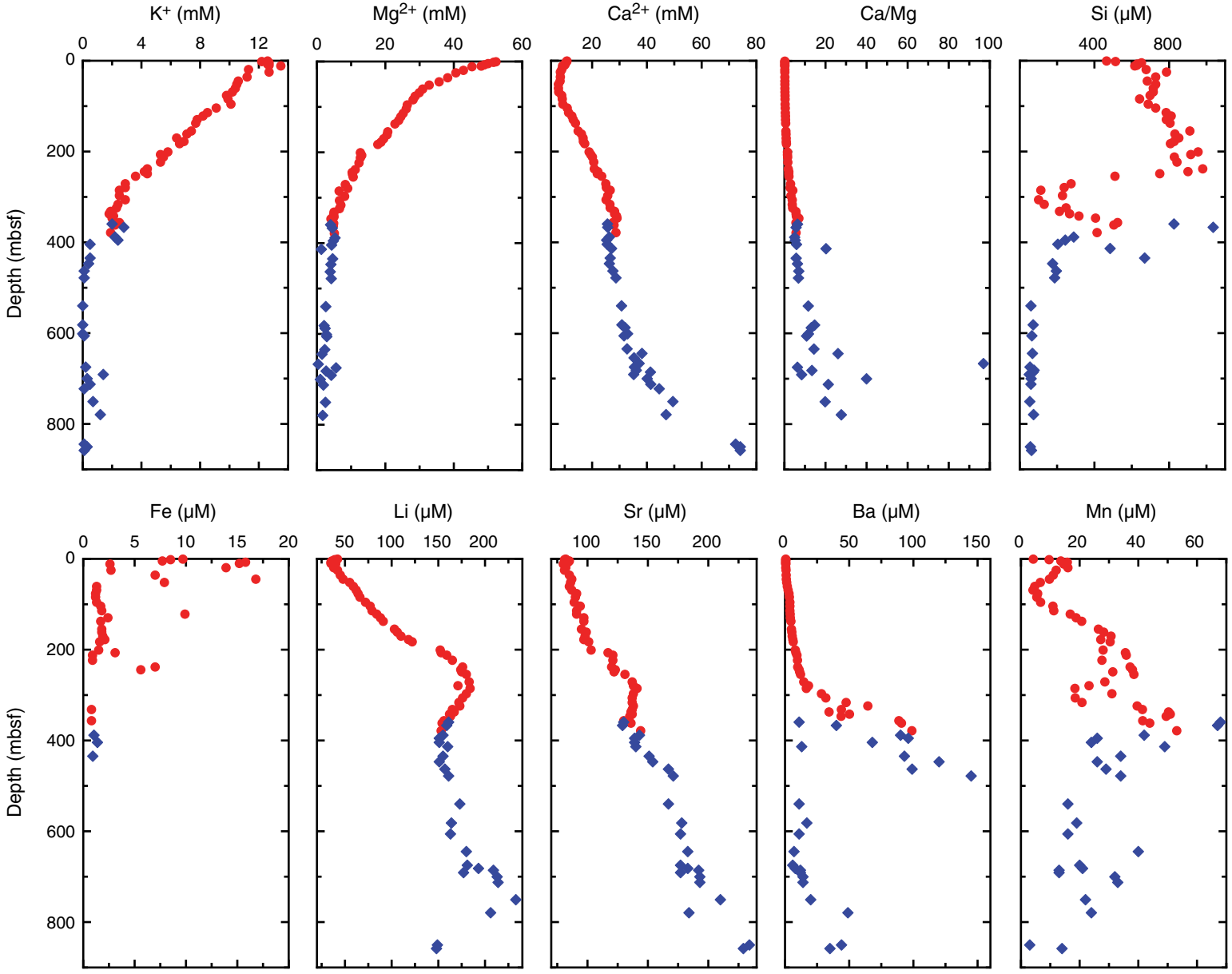

Figure F45. Interstitial water constituents of trace elements (rubidium, cesium, vanadium, copper, zinc, molybdenum, lead, and uranium), Holes C0011C and C0011D (Table T12).

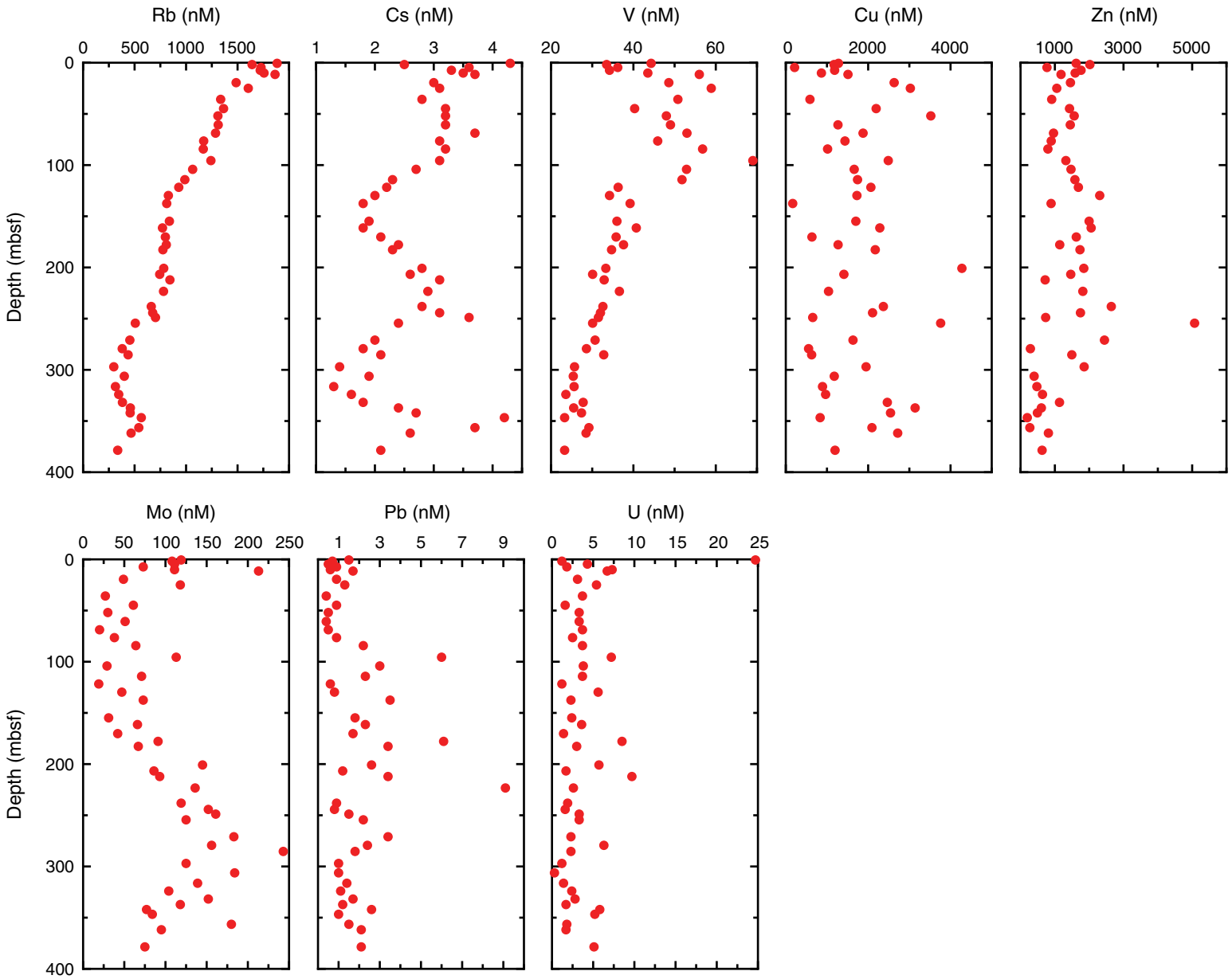

Figure F46. Headspace methane concentration, Holes C0011C and C0011D. Methane is set at 0.0 when below detection. ppmv = parts per million by volume.

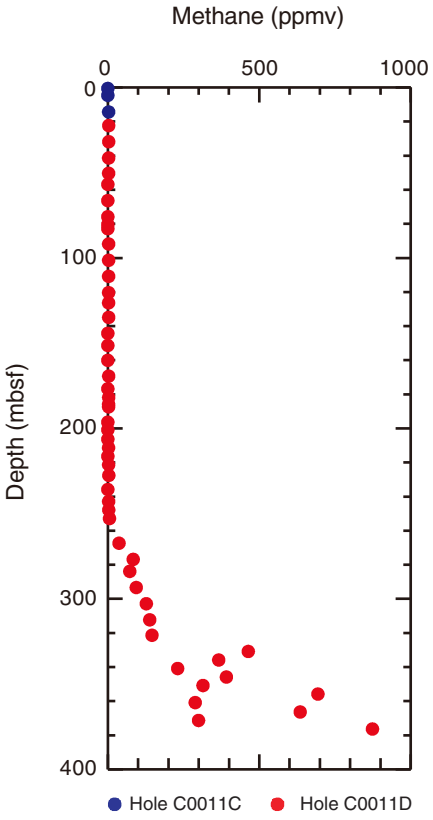

Figure F47. Calcium carbonate ($CaCO_3$), total organic carbon (TOC), total nitrogen (TN), the atomic ratios of total organic carbon to total nitrogen (TOC/TN_{at}), and total sulfur (TS) contents in bulk sediments, Holes C0011C and C0011D.

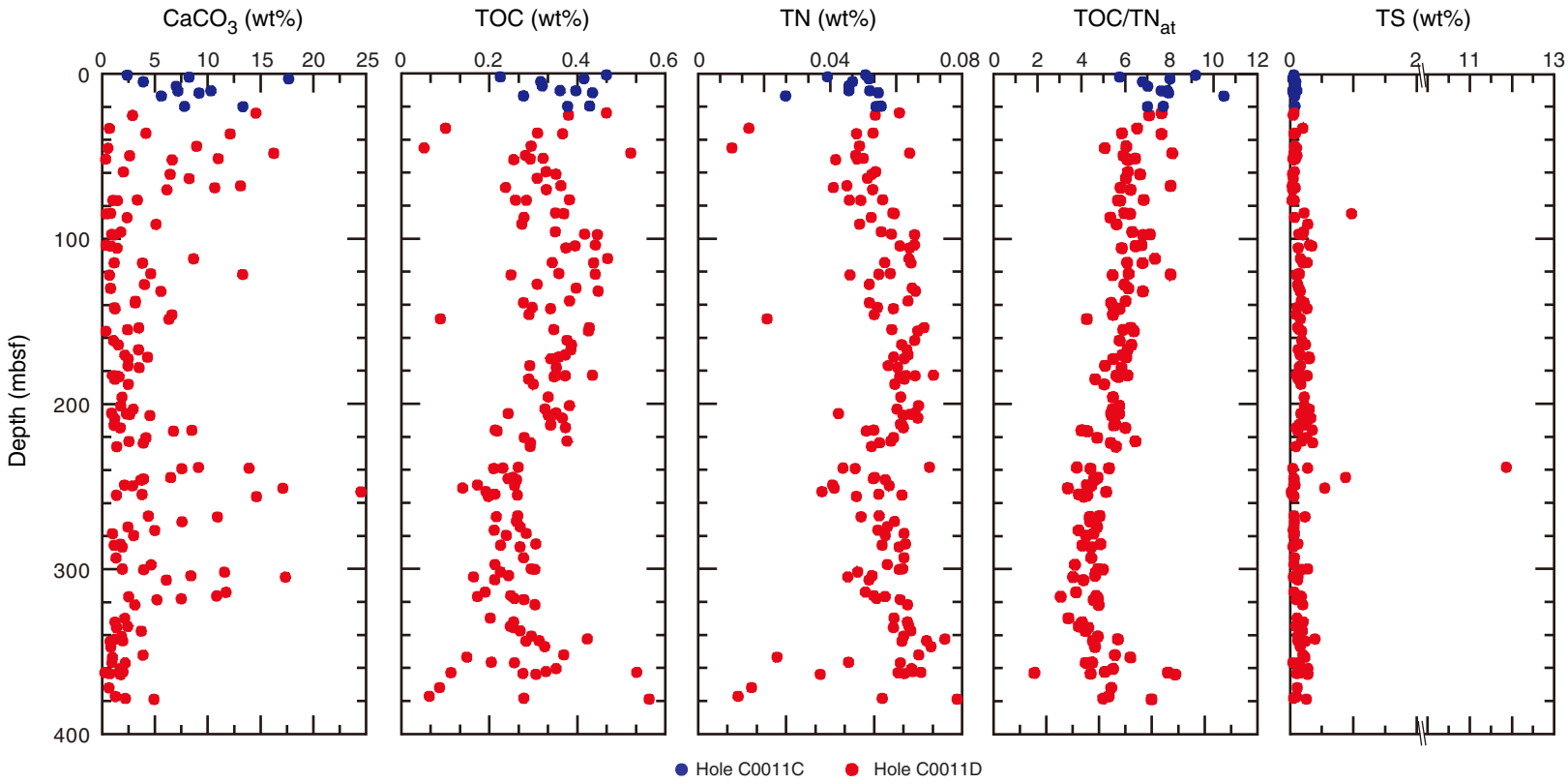

Figure F48. Rock-Eval pyrolysis parameters. S1, S2, T_{max}, hydrogen index (HI), and production index (PI), Holes C0011C and C0011D. HC = hydrocarbon, TOC = total organic carbon.

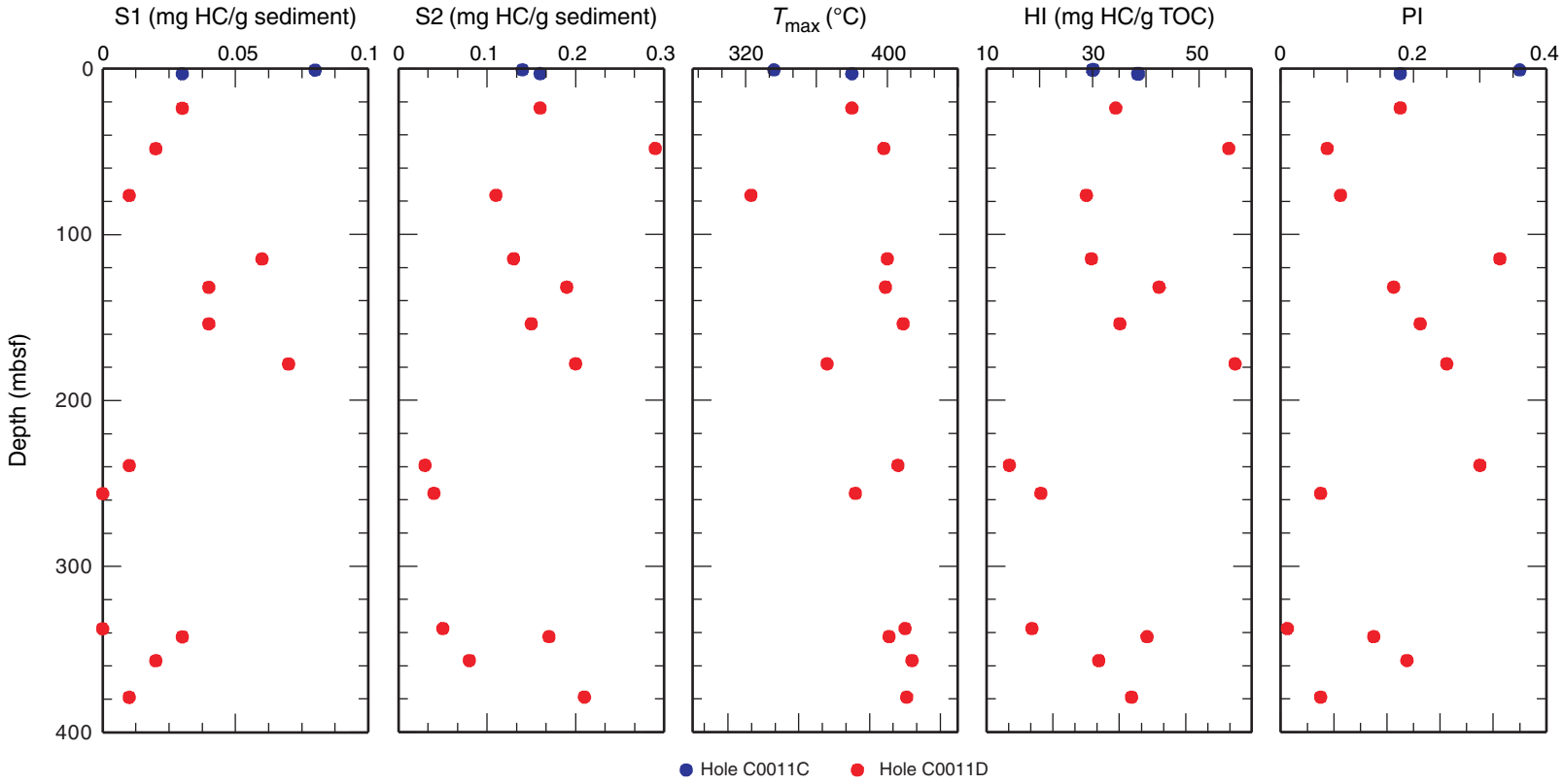

Table T1. Coring summary, Site C0011. (Continued on next page.)

Hole C0011C
Latitude: 32°49.7436′N
Longitude: 136°52.9250′E
Seafloor (DRF, m): 4079
Total depth (DRF, m): 4101.5
Total penetration (DSF, m): 22.5
Total length of cored section (m): 22.5
Total core recovered (m): 22.99
Core recovery (%): 102.2
Total number of cores: 3

Hole C0011D
Latitude: 32°49.7436′N
Longitude: 136°52.9250′E
Seafloor (DRF, m): 4079
Total depth (DRF, m): 4459
Total penetration (DSF, m): 380
Total length of cored section (m): 359
Total core recovered (m): 351.49
Core recovery (%): 97.9
Total number of cores: 52

Core	Depth CSF (m) Top	Depth CSF (m) Bottom	Advanced (m)	Core recovered (m)	Recovery (%)
333-C0011C-					
1H	0.00	3.50	3.50	3.50	100.0
2H	3.50	13.00	9.50	9.49	99.9
3H	13.00	22.50	9.50	10.00	105.3
333-C0011D-					
1H	21.00	30.50	9.50	9.80	103.2
2H	30.50	40.00	9.50	9.78	102.9
3H	40.00	49.00	9.00	9.46	105.1
4H	49.00	55.50	6.50	6.61	101.7
5H	55.50	65.00	9.50	9.91	104.3
6H	65.00	74.50	9.50	9.6	101.1
7H	74.50	79.00	4.50	4.33	96.2
8H	79.00	81.50	2.50	2.07	82.8
9H	81.50	90.50	9.00	9	100.0
10H	90.50	100.00	9.50	9.85	103.7
11H	100.00	109.50	9.50	9.56	100.6
12H	109.50	119.00	9.50	9.9	104.2
13H	119.00	125.00	6.00	6.79	113.2
14H	125.00	133.50	8.50	8.98	105.6
15H	133.50	143.00	9.50	9.86	103.8
16H	143.00	150.00	7.00	5.79	82.7
17H	150.00	158.50	8.50	8.89	104.6
18H	158.50	168.00	9.50	9.76	102.7
19H	168.00	175.00	7.00	7.05	100.7
20H	175.00	180.50	5.50	5.86	106.5
21H	180.50	184.50	4.00	4.69	117.3
22H	184.50	186.00	1.50	1.66	110.7
23T	186.00	195.50	9.50	3.67	38.6
24T	195.50	200.00	4.50	2.34	52.0
25T	200.00	205.00	5.00	3.86	77.2
26X	205.00	210.00	5.00	7.93	158.6
27X	210.00	215.00	5.00	6.48	129.6
28X	215.00	220.00	5.00	5.13	102.6
29X	220.00	225.00	5.00	5.41	108.2
30X	225.00	234.50	9.50	3.85	40.5
31X	234.50	241.50	7.00	6.41	91.6
32X	241.50	246.50	5.00	5.4	108.0
33X	246.50	251.50	5.00	5.24	104.8
34X	251.50	256.50	5.00	7.19	143.8
35X	256.50	266.00	9.50	0.88	9.3
36X	266.00	275.50	9.50	9.95	104.7
37X	275.50	282.50	7.00	7.43	106.1
38X	282.50	292.00	9.50	7.43	78.2
39X	292.00	301.50	9.50	9.8	103.2
40X	301.50	311.00	9.50	9.86	103.8
41X	311.00	320.00	9.00	8.93	99.2

Table T1 (continued).

Core	Depth CSF (m) Top	Depth CSF (m) Bottom	Advanced (m)	Core recovered (m)	Recovery (%)
42X	320.00	329.50	9.50	9.76	102.7
43X	329.50	334.50	5.00	5.93	118.6
44X	334.50	339.50	5.00	5.91	118.2
45X	339.50	344.50	5.00	5.36	107.2
46X	344.50	349.50	5.00	5.28	105.6
47X	349.50	354.50	5.00	5.81	116.2
48X	354.50	359.50	5.00	5.95	119.0
49X	359.50	365.00	5.50	6.58	119.6
50X	365.00	370.00	5.00	5.49	109.8
51X	370.00	375.00	5.00	4.44	88.8
52X	375.00	380.00	5.00	4.59	91.8

DRF = drilling depth below rig floor, DSF = drilling depth below seafloor, CSF = core depth below seafloor. H = hydraulic piston coring system, X = extended shoe coring system, T = extended punch coring system.

Table T2. Upper and lower boundaries of depositional units at Site C0011, Expedition 333 Holes C0011C and C0011D, Expedition 322 Hole C0011B.

Lith. unit	Core, section, interval (cm) Top	Core, section, interval (cm) Bottom	Depth (mbsf) Top	Depth (mbsf) Bottom	Thickness (m)
I	333-C0011C/D-1H-1, 0	333-C0011D-46X-4, 78.4	0	347.82	347.82
II	333-C0011D-46X-4, 78.4	322-C0011B-17R-CC, 6	347.82	479.06	131.24
III	322-C0011B-17R-CC, 6	322-C0011B-40R-2, 58	479.06	673.98	194.92
IV	322-C0011B-40R-2, 58	322-C0011B-57R-3, 73	673.98	849.95	175.97
V	322-C0011B-57R-3, 73	322-C0011B-61R-CC, 5	849.95	876.05	26.1

Table T3. Results of bulk powder X-ray diffraction analysis, Holes C0011C and C0011D. (Continued on next three pages.)

Lith. unit	Core, section, interval (cm)	Depth (mbsf)	Measured values of X-ray diffraction peaks: Peak intensity (counts/step)				Measured values of X-ray diffraction peaks: Integrated peak area (total counts)				Abundance calculated from SVD normalization factors: Absolute (wt%)					Abundance calculated from SVD normalization factors: Relative (wt%)			
			Clay minerals	Quartz	Feldspar	Calcite	Clay minerals	Quartz	Feldspar	Calcite	Clay minerals	Quartz	Feldspar	Calcite	Total	Clay minerals	Quartz	Feldspar	Calcite
	333-C0011C-																		
	1H-2, 20	0.83	29	803	187	78	2,744	28,116	13,759	3,813	36.0	15.5	16.7	1.6	69.8	52	22	24	2
	1H-4, 19.5	2.06	49	694	134	198	3,787	25,974	10,391	8,377	44.2	14.2	11.9	7.0	77.3	57	18	15	9
	1H-5, 108.5	3.16	32	625	118	479	2,595	23,475	9,669	17,171	32.3	13.0	11.3	19.4	76.1	42	17	15	26
	2H-2, 19	4.87	35	789	162	101	3,032	28,889	13,157	4,496	38.4	16.0	15.8	2.3	72.4	53	22	22	3
	2H-5, 19.5	7.72	38	797	143	172	3,098	27,833	11,925	7,374	38.3	15.4	14.1	6.1	73.9	52	21	19	8
IA	2H-8, 19	10.54	41	622	126	236	3,566	22,563	11,665	9,160	43.1	12.2	13.9	8.2	77.4	56	16	18	11
	2H-9, 8	10.64	38	747	145	191	3,310	26,794	12,117	7,072	40.6	14.7	14.4	5.5	75.2	54	20	19	7
	2H-10, 20	11.96	40	738	138	196	3,136	26,276	11,726	8,304	38.7	14.5	13.9	7.3	74.3	52	19	19	10
	3H-1, 47	13.47	34	366	128	156	2,565	13,871	11,080	7,125	33.1	7.3	13.8	6.6	60.7	54	12	23	11
	3H-8, 20	20.09	36	703	107	187	3,220	25,943	10,242	7,525	38.4	14.3	11.8	6.3	70.9	54	20	17	9
	3H-9, 20	20.31	35	684	124	343	3,061	24,480	11,000	13,287	37.7	13.5	13.0	13.9	78.1	48	17	17	18
															Average:	52	19	19	10
	333-C0011D-																		
	1H-3, 15	23.79	33	727	126	327	2,597	26,994	10,896	13,632	32.9	15.0	12.9	14.7	75.5	44	20	17	19
	1H-4, 20	25.17	35	730	127	69	3,290	26,199	12,147	3,479	40.3	14.4	14.4	0.9	70.0	58	21	21	1
	2H-2, 121	33.03	25	229	242	29	2,620	9,716	13,420	1,928	35.3	4.7	17.2	0.1	57.3	62	8	30	Tr
	2H-5, 20	35.99	38	692	118	106	3,809	24,869	10,304	4,796	44.2	13.6	11.8	2.3	71.9	61	19	16	3
	2H-7, 20	36.43	34	638	134	286	3,042	24,012	10,980	12,351	37.5	13.2	13.0	12.8	76.4	49	17	17	17
	3H-3, 121	43.83	35	757	142	216	3,297	26,871	12,340	8,786	40.7	14.8	14.7	7.8	77.9	52	19	19	10
	3H-8, 43	48.14	31	586	112	367	3,002	20,894	10,354	14,629	36.9	11.4	12.3	15.9	76.4	48	15	16	21
	4H-1, 59	49.47	43	727	113	71	4,241	27,070	11,209	2,997	49.0	14.8	12.8	0.1	76.7	64	19	17	Tr
	4H-2, 121	51.09	40	656	117	262	3,676	23,762	10,582	10,104	43.4	13.0	12.3	9.4	78.0	56	17	16	12
	4H-3, 46	51.63	52	745	151	19	4,173	27,448	13,627	901	50.0	14.9	16.2	0.1	81.1	62	18	20	Tr
	4H-5, 20.5	52.10	39	623	159	189	3,630	23,260	12,289	7,171	44.1	12.6	14.7	5.5	76.9	57	16	19	7
	5H-3, 124.5	59.38	42	789	132	48	3,467	27,863	12,095	2,271	41.9	15.3	14.3	0.1	71.6	59	21	20	Tr
	5H-5, 20	60.89	39	738	141	177	3,174	26,910	12,345	6,785	39.4	14.8	14.7	5.2	74.2	53	20	20	7
	5H-7, 119.5	63.40	32	756	126	214	3,026	26,795	11,858	8,222	37.7	14.8	14.1	7.3	73.8	51	20	19	10
	6H-3, 20	67.87	36	574	138	273	2,985	21,188	10,651	11,280	36.8	11.6	12.7	11.5	72.5	51	16	18	16
IA	6H-4, 21.5	69.00	34	570	113	287	2,818	21,073	10,537	11,122	35.0	11.5	12.6	11.4	70.6	50	16	18	16
	6H-5, 124	70.20	46	721	120	180	3,724	26,079	9,882	6,807	43.1	14.3	11.2	5.0	73.6	59	19	15	7
	7H-2, 125	75.74	52	608	104	84	4,806	22,807	8,497	3,643	52.8	12.3	9.2	0.2	74.5	71	17	12	Tr
	7H-4, 20	76.57	36	632	187	31	3,223	23,979	14,801	1,592	41.6	13.0	18.2	0.1	72.9	57	18	25	Tr
	7H-5, 20	76.67	48	650	109	41	4,675	23,082	10,044	1,924	52.6	12.4	11.3	0.1	76.4	69	16	15	Tr
	9H-3, 20	84.48	37	804	133	27	4,291	29,807	11,089	1,543	49.2	16.4	12.5	0.1	78.2	63	21	16	Tr
	9H-4, 34	84.83	52	698	125	15	4,644	25,935	9,144	723	51.4	14.1	10.0	0.1	75.6	68	19	13	Tr
	9H-6, 33	87.09	42	822	141	58	4,185	29,281	11,369	2,492	48.4	16.1	13.0	0.1	77.6	62	21	17	Tr
	10H-1, 68	91.15	37	675	144	129	3,414	24,765	11,935	5,484	41.5	13.5	14.2	3.4	72.7	57	19	20	Tr
	10H-5, 21	95.81	42	761	162	52	3,545	27,107	13,008	2,733	43.4	14.8	15.5	0.1	73.8	59	20	21	Tr
	10H-7, 8	97.23	46	760	130	33	5,252	27,675	9,765	1,985	57.9	15.0	10.5	0.1	83.5	69	18	13	Tr
	10H-7, 44	97.58	53	828	143	25	4,271	30,329	11,028	1,397	48.9	16.7	12.4	0.1	78.1	63	21	16	Tr
	11H-3, 104.5	103.78	49	882	126	13	4,915	31,118	10,461	678	54.8	17.1	11.4	0.1	83.4	66	20	14	Tr
	11H-5, 22	104.37	47	808	147	33	4,145	29,436	11,521	1,663	48.1	16.2	13.2	0.1	77.5	62	21	17	Tr
	11H-6, 121	105.56	46	802	126	35	4,622	29,242	10,087	2,070	51.8	16.0	11.1	0.1	79.0	66	20	14	Tr
	12H-2, 125	111.99	40	661	146	182	3,919	23,582	10,248	8,724	45.5	12.8	11.8	7.4	77.5	59	17	15	10

Table T3 (continued). (Continued on next page.)

Lith. unit	Core, section, interval (cm)	Depth (mbsf)	Measured values of X-ray diffraction peaks: Peak intensity (counts/step): Clay minerals	Quartz	Feldspar	Calcite	Integrated peak area (total counts): Clay minerals	Quartz	Feldspar	Calcite	Abundance calculated from SVD normalization factors: Absolute (wt%): Clay minerals	Quartz	Feldspar	Calcite	Total	Relative (wt%): Clay minerals	Quartz	Feldspar	Calcite
IA	12H-5, 20.5	114.45	47	735	126	40	4,691	26,423	10,309	2,314	52.8	14.4	11.5	0.1	78.7	67	18	15	Tr
	12H-8, 20	117.39	52	772	116	104	4,900	28,773	9,154	4,052	54.0	15.8	9.8	0.5	79.9	68	20	12	1
	13H-2, 125	120.59	43	719	125	116	4,302	26,755	10,719	5,645	49.3	14.6	12.2	3.0	79.1	62	18	15	4
	13H-3, 85	121.19	33	523	85	288	2,842	20,177	7,958	13,286	33.5	11.1	9.1	14.4	68.1	49	16	13	21
	13H-5, 22.5	121.85	47	597	100	34	4,173	23,000	8,728	2,044	46.6	12.5	9.7	0.1	68.9	68	18	14	Tr
	14H-3, 15	127.58	44	715	137	108	4,163	26,951	10,383	5,049	47.7	14.8	11.7	2.3	76.5	62	19	15	3
	14H-5, 22	129.91	49	820	126	23	4,769	30,007	10,184	1,153	53.2	16.4	11.2	0.1	80.9	66	20	14	Tr
	14H-7, 60	131.71	47	761	123	142	4,824	27,421	9,705	6,225	53.8	15.0	10.6	3.4	82.7	65	18	13	4
	15H-4, 21.5	137.72	48	856	125	76	4,384	31,181	9,982	3,349	49.3	17.2	10.9	0.1	77.6	64	22	14	Tr
	15H-5, 105	138.72	48	783	119	80	4,112	28,003	9,914	3,513	46.7	15.4	11.1	0.3	73.5	64	21	15	Tr
	15H-7, 125.5	141.59	44	786	113	40	4,237	28,686	10,546	1,890	48.3	15.7	11.9	0.1	76.0	64	21	16	Tr
	15H-8, 63	142.33	52	829	121	31	4,550	30,941	11,015	1,793	51.7	17.0	12.3	0.1	81.1	64	21	15	Tr
	16H-4, 52	145.96	41	761	127	154	4,107	26,629	11,014	6,670	47.7	14.6	12.6	4.5	79.3	60	18	16	6
	17H-5, 20	153.80	52	827	121	99	5,008	30,020	10,490	3,964	55.9	16.4	11.5	0.2	84.0	67	20	14	Tr
	17H-6, 20.5	155.01	52	846	123	52	5,091	30,772	10,192	2,674	56.5	16.9	11.0	0.1	84.4	67	20	13	Tr
	17H-7, 88	155.76	55	899	145	21	5,322	32,673	11,562	1,204	59.6	17.9	12.8	0.1	90.3	66	20	14	Tr
	18H-4, 21	161.58	56	842	142	31	4,675	31,586	11,310	1,438	53.1	17.3	12.7	0.1	83.2	64	21	15	Tr
	18H-6, 126	164.15	53	805	129	37	4,366	29,111	11,101	1,981	50.0	15.9	12.6	0.1	78.6	64	20	16	Tr
	18H-9, 20	167.17	58	870	136	86	4,526	30,372	11,530	4,256	51.9	16.7	13.0	0.9	82.5	63	20	16	1
	19H-3, 20	170.40	47	770	117	52	4,741	28,368	9,457	2,694	52.6	15.5	10.2	0.1	78.4	67	20	13	Tr
	19H-4, 127	171.41	50	755	123	96	4,871	27,371	9,307	5,119	53.9	14.9	10.0	1.9	80.8	67	18	12	2
	19H-5, 119	172.48	52	792	126	72	4,564	28,745	10,511	3,450	51.6	15.7	11.7	0.1	79.1	65	20	15	Tr
	20H-3, 20	176.89	40	684	122	62	4,105	29,399	10,314	2,829	46.9	16.2	11.5	0.1	74.7	63	22	15	Tr
	20H-4, 20	178.00	60	794	103	82	5,274	28,354	8,870	4,056	57.5	15.5	9.3	0.2	82.4	70	19	11	Tr
	21H-2, 120	182.37	55	878	146	19	5,106	34,759	9,900	1,212	56.1	19.2	10.4	0.1	85.9	65	22	12	Tr
	21H-4, 20.5	182.84	55	775	114	18	5,178	28,921	9,620	841	56.9	15.8	10.3	0.1	83.1	68	19	12	Tr
	21H-5, 20	182.99	51	651	124	28	4,837	28,435	12,106	1,620	55.4	15.4	13.8	0.1	84.8	65	18	16	Tr
	21H-5, 70	183.35	48	721	123	35	4,896	26,754	8,906	1,943	53.8	14.6	9.5	0.1	77.9	69	19	12	Tr
	22H-1, 53.5	184.63	66	790	117	28	5,359	29,099	10,114	1,886	59.1	15.8	10.9	0.1	86.0	69	18	13	Tr
	23T-2, 69	188.10	52	721	146	52	4,499	30,030	11,429	2,345	51.5	16.5	12.9	0.1	81.0	64	20	16	Tr
	24T-1, 38	195.88	51	861	124	53	4,441	30,596	11,137	2,198	50.7	16.8	12.5	0.1	80.1	63	21	16	Tr
	25T-2, 29	201.15	40	895	145	39	4,761	32,414	10,535	2,521	53.4	17.9	11.5	0.1	82.8	64	22	14	Tr
	25T-4, 61	203.18	46	733	119	64	4,957	27,047	9,151	3,673	54.6	14.7	9.8	0.1	79.2	69	19	12	Tr
	26X-1, 56	205.34	56	809	156	21	4,922	31,324	11,002	1,365	55.3	17.2	12.2	0.1	84.7	65	20	14	Tr
	26X-1, 92	205.55	46	455	78	58	4,408	17,385	6,232	3,009	47.5	9.3	6.4	0.1	63.3	75	15	10	Tr
	26X-1, 134	205.81	47	728	104	67	5,014	27,990	8,435	3,097	54.6	15.3	8.8	0.1	78.7	69	19	11	Tr
	26X-3, 30.5	206.88	47	787	128	121	4,840	29,224	10,082	4,656	54.1	16.0	11.0	1.2	82.3	66	19	13	2
	26X-6, 27	208.55	54	839	145	29	5,222	31,289	10,747	1,417	58.1	17.1	11.7	0.1	87.0	67	20	13	Tr
	27X-3, 30.5	212.37	49	822	114	19	5,180	29,693	8,720	975	56.2	16.3	9.0	0.1	81.7	69	20	11	Tr
	27X-4, 62	212.85	48	753	130	30	4,464	27,663	10,523	1,407	50.6	15.1	11.8	0.1	77.6	65	19	15	Tr
	27X-6, 21	214.42	48	804	117	45	4,689	28,956	9,682	1,972	52.2	15.9	10.5	0.1	78.7	66	20	13	Tr
	28X-1, 97	215.90	56	683	106	167	3,814	25,037	9,558	7,663	43.8	13.7	10.8	6.1	74.4	59	18	14	8
	28X-2, 17	216.47	43	664	97	150	4,488	25,020	9,339	6,455	50.3	13.6	10.3	4.0	78.2	64	17	13	5
	29X-1, 46	220.39	45	763	141	109	4,070	27,301	11,638	5,087	47.7	14.9	13.5	2.4	78.4	61	19	17	3
	29X-3, 25	222.61	46	570	100	53	4,430	22,781	8,781	2,733	49.3	12.3	9.7	0.1	71.4	69	17	14	Tr
	29X-4, 31	223.59	42	634	118	94	3,773	22,592	8,999	4,238	43.0	12.3	10.2	1.7	67.2	64	18	15	3

Table T3 (continued). (Continued on next page.)

Lith. unit	Core, section, interval (cm)	Depth (mbsf)	Measured values of X-ray diffraction peaks: Peak intensity (counts/step): Clay minerals	Quartz	Feldspar	Calcite	Integrated peak area (total counts): Clay minerals	Quartz	Feldspar	Calcite	Abundance calculated from SVD normalization factors: Absolute (wt%): Clay minerals	Quartz	Feldspar	Calcite	Total	Relative (wt%): Clay minerals	Quartz	Feldspar	Calcite
IA	30X-1, 85	225.85	49	741	115	41	4,933	26,734	10,645	1,581	55.4	14.5	11.9	0.1	81.8	68	18	15	Tr
	31X-4, 29	238.43	35	381	61	166	2,467	13,374	4,734	6,688	27.5	7.3	5.1	6.3	46.2	59	16	11	14
	31X-5, 47	238.92	42	503	104	262	3,787	19,149	9,682	12,284	44.1	10.3	11.2	12.3	78.0	57	13	14	16
	31X-5, 76	239.21	51	670	124	187	4,698	24,847	11,297	7,695	53.9	13.4	12.9	5.4	85.6	63	16	15	6
	31X-5, 106	239.51	56	600	102	78	5,575	23,149	9,447	3,694	61.1	12.3	10.2	0.1	83.8	73	15	12	Tr
	32X-4, 28.5	244.54	49	678	103	180	5,678	24,790	8,461	6,909	61.5	13.3	8.8	3.8	87.3	70	15	10	4
	32X-5, 82	245.29	47	705	103	106	4,960	26,214	8,989	4,638	54.6	14.3	9.6	1.3	79.7	68	18	12	2
	32X-6, 23	246.03	47	767	119	80	4,383	28,486	10,330	3,732	49.7	15.6	11.5	0.4	77.2	64	20	15	Tr
	33X-3, 30.5	249.15	44	483	100	67	4,877	18,970	8,819	3,851	53.9	10.0	9.8	0.5	74.3	73	13	13	1
	33X-4, 37	249.52	64	790	117	77	5,544	29,284	9,496	3,400	60.5	15.9	10.0	0.1	86.6	70	18	12	Tr
	33X-4, 82	249.93	64	603	119	69	5,856	22,170	8,421	2,866	63.2	11.8	8.8	0.1	83.8	75	14	10	Tr
	33X-5, 58	251.01	38	420	334	331	4,017	17,283	17,238	15,998	52.2	8.8	21.6	16.8	99.4	52	9	22	17
															Average:	63	19	15	3
IB	34X-2, 76	252.99	37	465	84	395	2,982	17,381	7,395	20,107	34.9	9.5	8.4	23.3	76.1	46	12	11	31
	34X-4, 34	254.68	55	794	123	103	5,222	28,971	11,127	4,425	58.6	15.7	12.4	0.6	87.3	67	18	14	1
	34X-5, 60	255.10	58	829	128	36	5,560	30,284	10,668	2,254	61.5	16.5	11.6	0.1	89.6	69	18	13	Tr
	34X-6, 45	255.97	46	642	107	296	4,288	24,511	8,851	12,863	48.3	13.4	9.7	12.6	83.9	58	16	12	15
	36X-2, 55	267.84	59	775	125	111	5,722	28,412	10,890	5,047	63.4	15.3	11.9	1.1	91.8	69	17	13	1
	36X-2, 110	268.36	47	735	105	232	4,663	27,004	9,156	10,191	52.0	14.8	9.9	8.7	85.3	61	17	12	10
	36X-5, 34	271.29	53	806	132	200	4,671	29,319	99,52	7,937	52.4	16.1	10.9	5.7	85.0	62	19	13	7
	36X-8, 55	274.48	64	787	109	66	6,089	29,026	9,960	3,041	66.3	15.7	10.5	0.1	92.5	72	17	11	Tr
	37X-1, 111	276.52	64	766	100	125	6,229	27,525	8,899	5,507	67.1	14.8	9.1	1.4	92.4	73	16	10	2
	37X-3, 50	278.51	61	859	121	18	5,639	30,915	10,976	1,576	62.4	16.8	11.9	0.1	91.3	68	18	13	Tr
	37X-4, 32.5	279.65	66	825	132	80	5,577	30,166	11,020	3,189	61.9	16.4	12.1	0.1	90.5	68	18	13	Tr
	38X-2, 98	284.89	70	816	117	46	6,336	29,390	9,872	2,324	68.6	15.9	10.3	0.1	94.8	72	17	11	Tr
	38X-3, 35	285.67	68	777	110	30	6,299	29,708	9,990	2,098	68.3	16.0	10.5	0.1	94.9	72	17	11	Tr
	38X-5, 38	286.66	64	777	106	41	6,339	28,617	9,844	2,425	68.6	15.4	10.3	0.1	94.4	73	16	11	Tr
	39X-1, 126	293.21	65	772	125	36	6,222	29,616	9,746	2,043	67.4	16.0	10.1	0.1	93.6	72	17	11	Tr
	39X-5, 35	297.38	66	748	114	125	6,491	27,524	9,674	5,121	70.2	14.8	10.1	0.7	95.7	73	15	11	1
	39X-7, 124	299.95	66	827	116	60	6,167	30,293	9,370	2,692	66.5	16.4	9.6	0.1	92.7	72	18	10	Tr
	39X-8, 22	300.33	67	748	113	117	6,067	27,547	9,464	4,804	65.8	14.8	9.9	0.6	91.2	72	16	11	1
	40X-1, 40	301.88	52	714	101	220	5,078	25,928	8,950	10,990	56.0	14.1	9.5	9.5	89.1	63	16	11	11
	40X-2, 125	304.01	58	733	96	191	5,139	26,409	7,546	8,829	55.5	14.4	7.6	6.7	84.1	66	17	9	8
	40X-3, 72	304.85	44	642	104	351	4,625	22,866	8,165	15,827	51.3	12.4	8.7	16.3	88.7	58	14	10	18
	40X-5, 40	306.64	58	754	125	168	5,563	27,761	10,198	7,167	61.5	15.0	11.0	4.0	91.5	67	16	12	4
	41X-3, 32	314.08	50	713	108	257	4,632	26,172	8,226	11,118	51.1	14.3	8.7	10.0	84.0	61	17	10	12
	41X-4, 106	316.24	50	711	109	266	5,072	25,408	8,608	10,919	55.7	13.8	9.1	9.4	88.0	63	16	10	11
	41X-5, 38.5	316.76	60	817	118	83	5,812	30,668	10,146	3,209	63.6	16.7	10.8	0.1	91.1	70	18	12	Tr
	41X-6, 120	317.98	62	722	109	192	6,064	27,281	8,411	7,866	65.2	14.7	8.5	4.7	93.0	70	16	9	5
	41X-7, 43	318.62	57	776	95	135	5,712	28,652	8,639	5,945	61.7	15.6	8.8	2.4	88.5	70	18	10	3
	43X-1, 33	329.77	55	907	158	46	5,816	32,571	11,822	3,034	64.7	17.7	13.0	0.1	95.5	68	19	14	Tr
	43X-3, 35	332.09	65	608	123	28	6,833	28,418	10,423	1,823	73.9	15.2	11.0	0.1	100.2	74	15	11	Tr
	44X-1, 25	334.71	58	846	118	71	5,544	31,431	11,560	3,397	61.9	17.1	12.7	0.1	91.9	67	19	14	Tr
	44X-1, 105	335.38	61	743	130	33	6,313	30,153	11,319	1,966	69.4	16.2	12.3	0.1	98.0	71	17	13	Tr
	44X-4, 38	337.53	59	853	133	86	5,733	31,717	10,827	3,588	63.3	17.3	11.7	0.1	92.3	69	19	13	Tr
	45X-1, 128	340.67	53	741	147	34	5,475	29,906	12,280	2,285	61.8	16.2	13.8	0.1	91.9	67	18	15	Tr

Table T3 (continued).

Lith. unit	Core, section, interval (cm)	Depth (mbsf)	Measured values of X-ray diffraction peaks: Peak intensity (counts/step)				Measured values of X-ray diffraction peaks: Integrated peak area (total counts)				Abundance calculated from SVD normalization factors: Absolute (wt%)					Abundance calculated from SVD normalization factors: Relative (wt%)			
			Clay minerals	Quartz	Feldspar	Calcite	Clay minerals	Quartz	Feldspar	Calcite	Clay minerals	Quartz	Feldspar	Calcite	Total	Clay minerals	Quartz	Feldspar	Calcite
IB	45X-3, 38.5	342.44	63	631	112	26	6,281	26,056	10,760	1,903	68.8	13.9	11.7	0.1	94.5	73	15	12	Tr
	45X-5, 13	343.51	62	894	150	50	6,118	31,513	11,120	2,706	67.3	17.1	12.0	0.1	96.4	70	18	12	Tr
	45X-5, 45	343.80	68	719	129	25	5,979	29,229	10,431	2,042	65.5	15.8	11.2	0.1	92.5	71	17	12	Tr
	46X-3, 39	347.08	65	741	143	25	6,126	31,329	11,892	1,831	67.9	16.9	13.0	0.1	98.0	69	17	13	Tr
															Average:	68	17	12	3
II	47X-4, 50	351.99	67	751	105	93	5,877	27,342	9,662	3,624	64.1	14.7	10.2	0.1	89.1	72	17	11	Tr
	47X-6, 115	353.22	33	758	554	44	3,159	25,225	32,624	2,082	53.9	12.9	42.6	0.1	109.6	49	12	39	Tr
	48X-2, 93	356.42	47	736	307	30	4,283	26,707	20,225	1,722	55.9	14.2	25.2	0.1	95.4	59	15	26	Tr
	48X-3, 38	356.81	62	728	163	38	5,725	28,906	12,908	2,143	64.8	15.5	14.7	0.1	95.1	68	16	15	Tr
	49X-1, 93	360.25	66	773	134	54	5,257	28,712	11,172	2,309	58.9	15.6	12.4	0.1	87.0	68	18	14	Tr
	49X-3, 41	362.15	61	823	124	53	5,910	29,620	11,327	2,386	65.4	16.0	12.4	0.1	93.9	70	17	13	Tr
	49X-4, 50	362.57	56	713	124	28	5,839	27,255	10,301	1,878	64.1	14.7	11.1	0.1	90.0	71	16	12	Tr
	49X-4, 71	362.74	65	807	155	24	5,601	30,452	12,105	1,469	62.9	16.5	13.5	0.1	93.0	68	18	15	Tr
	49X-4, 120	363.14	56	693	122	21	5,289	27,040	11,062	1,553	59.2	14.6	12.4	0.1	86.2	69	17	14	Tr
	49X-5, 59	363.79	50	714	240	49	4,704	25,476	16,898	2,670	57.8	13.5	20.6	0.1	92.0	63	15	22	Tr
	50X-4, 56	369.18	22	1149	486	36	1,731	37,087	31,605	1,924	38.5	20.2	41.1	0.1	99.8	39	20	41	Tr
	51X-2, 81	372.19	25	1073	877	36	1,653	33,444	40,880	1,932	44.6	17.7	54.0	0.1	116.4	38	15	46	Tr
	52X-3, 56	378.37	69	813	127	57	5,978	29,896	10,080	3,635	65.2	16.2	10.7	0.1	92.2	71	18	12	Tr
	52X-4, 37	378.93	67	664	92	110	5,749	24,447	8,958	5,100	62.5	13.1	9.4	1.3	86.3	72	15	11	2
															Average:	63	16	21	Tr

SVD = singular value decomposition. Tr = trace.

Table T4. Results of XRF analysis, Holes C0011C and C0011D.

Lith. unit	Core, section, interval (cm)	Depth (mbsf)	Major element oxide (wt%)										LOI (wt%)	Total
			SiO_2	Al_2O_3	Fe_2O_3	MnO	MgO	CaO	Na_2O	K_2O	TiO_2	P_2O_5		
	333-C0011C-													
	1H-2, 20.0–22.0	0.80	63.6	15.7	5.39	0.06	2.37	3.51	3.63	3.11	0.65	0.11	7.1	98.1
	1H-4, 19.5–21.5	1.98	60.6	15.4	5.94	0.06	2.45	6.18	3.34	2.98	0.65	0.10	9.1	97.7
	2H-2, 19.0–21.0	4.83	61.6	16.4	6.22	0.07	2.68	3.91	3.48	3.06	0.69	0.11	7.6	98.2
	2H-10, 20.0–22.0	11.63	59.5	16.2	5.70	0.08	2.67	7.04	3.06	2.87	0.69	0.11	9.4	98.0
	3H-8, 20.0–22.0	19.67	60.6	15.9	5.92	0.07	2.48	6.03	3.23	2.95	0.66	0.12	9.2	97.9
	333-C0011D-													
	1H-4, 20.0–22.0	25.18	62.9	16.7	5.77	0.07	2.46	3.38	3.43	3.02	0.71	0.11	6.5	98.6
	2H-5, 20.0–22.0	36.00	62.9	15.2	6.52	0.07	2.53	3.99	3.57	2.80	0.63	0.11	7.3	98.4
	3H-5, 21.5–23.5	45.02	77.2	13.6	2.25	0.06	0.39	1.21	4.16	5.00	0.15	0.04	4.9	104.1
	4H-5, 20.5–22.5	52.11	62.1	15.6	5.65	0.08	2.23	5.77	3.36	2.72	0.64	0.11	8.0	98.2
	5H-5, 20.0–22.0	60.90	60.9	16.3	5.91	0.07	2.50	5.76	3.31	2.77	0.72	0.12	8.0	98.4
	6H-4, 21.5–23.5	69.01	59.7	15.4	5.71	0.09	2.22	8.66	3.27	2.59	0.67	0.12	9.6	98.5
	7H-4, 20.0–22.0	76.57	63.8	16.4	5.82	0.07	2.22	2.87	3.57	2.62	0.68	0.11	5.6	98.1
	9H-3, 20.0–22.0	84.49	62.6	16.6	6.75	0.06	2.64	1.47	3.15	3.20	0.72	0.10	6.0	97.4
	10H-5, 21.0–23.0	95.82	62.5	16.4	6.43	0.07	2.45	2.52	3.52	3.00	0.70	0.10	6.4	97.7
	11H-5, 22.0–24.0	104.38	65.4	17.4	6.75	0.06	2.67	1.62	3.60	3.18	0.72	0.10	6.5	101.5
	12H-5, 20.5–22.5	114.46	63.0	17.0	6.13	0.07	2.37	2.12	3.41	2.94	0.71	0.09	6.4	97.9
	13H-5, 22.5–24.5	121.85	65.4	16.0	5.48	0.08	2.00	1.58	3.55	3.02	0.57	0.08	6.5	97.8
IA	14H-1, 8.0–10.0	125.08	72.5	13.0	2.51	0.06	0.30	0.86	3.82	4.80	0.11	0.04	5.1	98.0
	14H-5, 22.0–24.0	129.92	62.6	17.4	6.33	0.06	2.75	1.23	3.18	3.35	0.72	0.10	6.5	97.7
	15H-1, 74.0–76.0	134.20	72.7	13.3	4.62	0.09	0.92	3.51	4.07	2.15	0.31	0.06	6.9	101.8
	15H-4, 21.5–23.5	137.73	63.2	16.7	5.90	0.07	2.48	2.85	3.29	3.12	0.70	0.09	7.4	98.4
	17H-6, 20.5–22.5	155.01	62.9	16.9	5.92	0.11	2.46	2.27	3.19	3.14	0.68	0.10	7.0	97.7
	18H-4, 21.5–23.5	161.59	63.6	17.1	5.80	0.07	2.42	1.52	3.23	3.16	0.70	0.09	6.6	97.6
	19H-3, 20.0–22.0	170.40	62.4	17.1	6.03	0.10	2.53	2.09	3.19	3.13	0.70	0.09	7.1	97.4
	20H-4, 20.0–22.0	178.01	61.7	17.4	6.26	0.16	2.55	2.86	2.99	3.19	0.73	0.11	7.4	98.0
	21H-4, 20.5–22.5	182.84	61.9	18.1	6.62	0.11	2.70	1.38	2.98	3.38	0.74	0.11	6.6	98.0
	22H-1, 53.5–55.5	184.64	62.9	17.8	6.35	0.10	2.63	1.28	3.00	3.33	0.72	0.11	6.4	98.3
	23T-2, 69.0–71.0	188.11	62.1	17.5	6.09	0.10	2.52	2.29	3.15	3.17	0.70	0.09	6.9	97.7
	24T-1, 40.0–42.0	195.91	64.3	17.9	6.30	0.07	2.67	1.86	3.33	3.39	0.75	0.09	6.7	100.7
	25T-2, 29.0–31.0	201.16	62.6	17.5	6.24	0.07	2.54	1.67	3.07	3.36	0.74	0.09	6.8	97.9
	26X-3, 30.5–32.5	206.89	61.7	17.2	6.23	0.10	2.50	3.36	3.17	3.24	0.68	0.09	7.9	98.3
	27X-3, 30.5–32.5	212.37	61.7	18.3	6.63	0.12	2.81	1.19	2.95	3.55	0.77	0.10	6.8	98.1
	29X-4, 31.0–33.0	223.60	60.5	16.8	7.35	0.11	2.65	4.07	3.31	2.85	0.76	0.09	7.4	98.4
	30X-1, 85.0–87.0	225.86	62.7	17.2	6.16	0.08	2.52	1.82	3.35	3.16	0.71	0.09	6.3	97.7
	31X-4, 29.0–31.0	238.44	47.5	12.8	22.60	0.25	1.93	6.77	2.60	2.23	0.54	0.10	17.2	97.3
	32X-4, 28.5–30.5	244.55	59.3	16.7	7.61	0.25	2.43	4.76	3.28	2.93	0.68	0.10	9.3	98.1
	33X-3, 30.5–32.5	249.16	65.3	15.9	4.84	0.10	1.83	2.33	3.57	3.07	0.50	0.08	6.9	97.6
	34X-4, 34.0–36.0	254.68	63.0	17.1	6.05	0.18	2.39	2.83	2.69	3.28	0.71	0.09	6.7	98.4
	36X-5, 34.0–36.0	271.30	61.5	16.9	5.58	0.13	2.40	5.08	2.68	3.27	0.70	0.09	8.3	98.4
	37X-4, 32.5–34.5	279.66	62.3	17.6	6.26	0.19	2.63	2.14	2.51	3.50	0.74	0.10	6.2	98.0
	38X-3, 35.0–37.0	285.68	63.1	17.7	6.59	0.13	2.64	1.07	2.60	3.51	0.71	0.09	5.5	98.1
	39X-5, 35.0–37.0	297.39	61.9	17.5	6.25	0.33	2.55	2.93	2.45	3.38	0.73	0.09	6.9	98.0
	40X-5, 40.0–42.0	306.65	61.8	17.2	6.34	0.21	2.36	3.88	2.46	3.23	0.69	0.09	7.6	98.3
IB	41X-5, 38.5–40.5	316.77	63.5	17.7	6.08	0.09	2.30	1.96	2.47	3.26	0.70	0.08	5.8	98.2
	42X-6, 36.0–38.0	326.10	63.5	17.5	5.80	0.14	2.39	2.36	2.54	3.28	0.71	0.10	6.2	98.3
	43X-3, 35.5–37.5	332.09	63.2	17.0	6.55	0.30	2.53	1.07	2.42	3.20	0.69	0.09	5.6	97.1
	44X-4, 38.0–40.0	337.53	63.9	16.3	6.01	0.34	2.40	2.46	2.62	3.31	0.68	0.09	6.1	98.0
	44X-6, 55.0–56.0	338.54	56.6	17.8	5.53	1.02	2.14	8.94	3.10	1.48	0.72	0.83	7.5	98.2
	45X-3, 38.5–40.5	342.45	63.0	16.8	7.03	0.12	2.60	1.36	2.70	3.23	0.66	0.09	5.9	97.5
	46X-3, 39.0–41.0	347.09	65.1	16.3	6.24	0.11	2.47	1.09	2.56	3.29	0.66	0.08	5.0	98.0
	47X-4, 50.0–52.0	352.00	63.4	15.9	6.04	0.18	2.41	2.84	2.66	3.25	0.68	0.09	6.5	97.5
	47X-6, 115.0–117.0	353.22	66.2	15.6	4.99	0.10	1.80	3.72	3.49	1.91	0.51	0.09	4.3	98.4
	48X-3, 38.0–40.0	356.81	65.1	15.6	5.67	0.72	2.28	1.61	2.87	3.11	0.66	0.08	5.9	97.7
II	49X-3, 41.0–43.0	362.16	64.9	16.2	6.00	0.12	2.40	1.84	2.70	3.21	0.66	0.10	5.6	98.0
	50X-4, 56.0–58.0	369.18	69.4	13.9	4.22	0.08	1.55	3.88	3.10	1.67	0.48	0.08	2.8	98.4
	51X-1, 59.0–61.0	370.60	68.3	14.3	5.01	0.10	1.75	4.28	3.19	1.60	0.55	0.09	2.8	99.2
	52X-4, 37.0–39.0	378.94	61.6	17.0	6.43	0.17	2.71	3.42	2.46	3.28	0.68	0.10	7.3	97.9

LOI = loss on ignition.

Table T5. Distribution of calcareous nannofossils, Hole C0011C.

Age (Ma)	Core, section	Preservation	*Calcidiscus leptoporus*	*Ceratolithus rugosus*	*Coccolithus pelagicus*	*Gephyrocapsa muellerae*	*Gephyrocapsa oceanica*	*Gephyrocapsa parallela*	*Gephyrocapsa* spp. (<3.5 µm)	*Helicosphaera carteri*	*Helicosphaera inversa*	*Oolithotus fragilis*	*Phontosphaera japonica*	*Phontosphaera* sp.	*Pseudoemiliania lacunosa*	*Reticulofenestra* spp. (2.5–4 µm)	*Reticulofenestra* spp. (<2.5 µm)	*Rhabdosphaera clavigera*	*Rhabdosphaera stylifera*	*Scapholithus fossilis*	*Syracosphaera pulchra*	*Umberasphaera irregularis*	*Umbilicosphaera sibogae*
	333-C0011C-																						
0.291–0.436	1H-CC	W	R	+		R	C		A	R	+	+	+	R				+	+	+	R	+	R
0.436–0.90	2H-CC	M	R		+	C	C	C	A	C					C		+	+			+		+
	3H-CC	M	C	+	R	R	C	C	A	C			R	R	C	+	+	R	+		R		R

Preservation: M = moderate, W = well. Abundance: A = abundant, C = common, R = rare, + = present.

Table T6. Distribution of calcareous nannofossils, Hole C0011D.

Age (Ma)	Core, section	Preservation	*Amaurolithus* spp.	*Calcidiscus leptoporus*	*Calcidiscus macintyrei*	*Ceratolithus rugosus*	*Coccolithus pelagicus*	*Discoaster asymmetricus*	*Discoaster berggrenii*	*Discoaster brouweri*	*Discoaster challengeri*	*Discoaster pentaradiatus*	*Discoaster prepentaradiatus*	*Discoaster pseudovariabilis*	*Discoaster quinqueramus*	*Discoaster surculus*	*Discoaster tamalis*	*Discoaster variabilis*	*Discoaster* sp.	*Gephyrocapsa caribbeanica*	*Gephyrocapsa oceanica*	*Gephyrocapsa* spp. (<3.5 µm)	*Helicosphaera carteri*	*Helicosphaera granulata*	*Oolithotus fragilis*	*Phontosphaera japonica*	*Phontosphaera* sp.	*Pseudoemiliania lacunosa*	*Reticulofenestra asanoi*	*Reticulofenestra pseudoumbilicus*	*Reticulofenestra* spp. (6–7 µm)	*Reticulofenestra* spp. (5–6 µm)	*Reticulofenestra* spp. (4–5 µm)	*Reticulofenestra* spp. (2.5–4 µm)	*Reticulofenestra* spp. (<2.5 µm)	*Rhabdosphaera clavigera*	*Rhabdosphaera stylifera*	*Sphenolithus abies*	*Syracosphaera pulchra*	*Umbilicosphaera rotalia*	*Umbilicosphaera sibogae*
	333-C0011D-																																						
0.436–0.90	1H-CC	W		R			R															+	R				C	A			C	A	A	C	+	+		+		R
1.59–1.67	2H-CC	M		C		+	R													C	C	C	C			+	R	R				C	C	C	R	+		+		+
	3H-CC	W		R	R		R													C	C	C	R				+	R						C	C	+			+		R
1.67–2.06	4H-CC	M		R	R		R															R	R					R						C	C	R			+		+
2.06–2.50	5H-CC	M		R	R	+	R	+		R												+	R		+	+	R	R						C	C	R			R		R
	6H-CC	M		+	R		R	R		R									R				R				+	R						C	C						R
2.50–2.52	7H-CC	M			R		+	R		R		R							R				+					+						C	R						+
?	8H-CC	P		+	R		+																					+					R	R	R						
2.87–3.79	9H-CC	M		+	R		R	R		R		R				R	R		C				+			+	+	+					R	R	+				+		+
	10H-CC	W		+	C	+	R	R		R		R				R	R		C				+			+		R			R		R	C	C				+	+	+
	11H-CC	M		R	C		R	R		R		R				R	R		R				R			+					+	R	R	C	C				+	+	+
	12H-CC	W		R	R		R	R		R		R				R	R	+	C				R			+	+				+	R	C	A	A			+	R	R	+
	13H-CC	M			R	R	R	+		+		R				R	+	R	C				R				+						C	C	C			+	+	R	+
	14H-CC	M			R		+	+		+		R				R	+	+	C				+										C	C	C					+	
	15H-CC	M			R	R		+		+	+	R				+		R	C				+				+							C	A			R	+	+	
3.79–4.50	16H-CC	W			R	+	R	R		+	+	C				R		R	C				R			+	+			C		R	C	C	A			R	+	R	
	17H-CC	P			+		+												+											+								+			
	18H-CC	P			+																		+							+			+								
	19H-CC	M			R	+	R	+			+	+						+	C				+							C			R	C	C			C		+	
	20H-CC	P		+	R		+												R				+				+			R				+	+			R			
	21H-CC	VP																												+				+	C						
	22H-CC	M			R	+	R	+		+	+	R						R	C				R				+			C				C	C			R		+	
	23H-CC	M			R		R	+		+	R	R						R	C				R							R				C	C			R		+	
	24H-CC	M			R	+	R	+		+	R	R						R	C				R				+			R			R	C	C			R		R	
	25T-CC	M			R	+	R	R		+	R	R						R	C				R				+			R			R	C	C			R		R	
	26X-CC	M			R	+	R	+		+	R	R						R	C				+				+			C			R	C	C			R		R	
	27X-CC	M			R	+	R	+		+	+	R						R	C				R				+			C		C	C	C	C			R		R	
	28X-CC	M			R		R	+		+	+	R						R	C				R				+			C		C	C	C	C			R		R	
4.50–5.59	29X-CC	W	+		R	+	R	+			R	C					+	R	A				R	+			+			A		A	A	A	C	+		C	+	R	
	30X-CC	P			+														+											+				+							
	31X-CC	M			R		R	+		+	+	R		+				R	C				R							C		C	C	A	C			C	+	R	
	33X-CC	M	+		R		R	+		+	+	+						R	C				R							C		C	C	C	C			C	+	+	
	35X-CC	P			+																									+		+	+	+	R						
5.59–7.10	36X-CC	M			+		+	+		+	+	R			R			R	C				R				+			R		R	R	C	R			R	+	+	
	38X-CC	M	R		R		R	+		+	+	+			R			+	C				R							C		R	R	R	R			R	+	+	
	39X-CC	M	+		R		+	+		+	R	R			R			R	C				+				+			R		C	R	R	+			R			
	40X-CC	P			+		+	+							R				R														R	R				R			
	41X-CC	M			R		R			+	R		+		C	+		R	A											R		C	C	C	C			C	+	+	
	42X-CC	W			R		C		R		R				C			R	A				R				R						R	A	A			C	+	R	
	43X-CC	P								+					R			+	R															R	+						
	44X-CC	P																	+																+						
	45X-CC	W			R		R		R						R				C				R				+			C		R	C	A	A			R			
	46X-CC	P					+		+						+				R											+		+	+	+	+			+			
	47X-CC	M			+		R		R						R			R	R				+				+			R		+	+	R	+			R		+	
7.10–8.52	48X-CC	P							+									+	+															+	+				+		
	49X-CC	P							R									R	R				+												R	R			R			
	50X-CC	P							+										+																+	+						
?	52X-CC	P																	+																						

Preservation: VP = very poor, P = poor, M = moderate, W = well. Abundance: A = abundant, C = common, R = rare, + = present. Barren: 333-C0011D-32X-CC, 34X-CC, 37X-CC.

Table T7. Calcareous nannofossils events and absolute age, Holes C0011C and C0011D.

Calcareous nannofossil event	Age (Ma)				Hole, core, section		Depth (mbsf)			Sedimentation rate (cm/k.y.)
	Upper	Lower	Middle	Error	Top	Bottom	Top	Bottom	Middle	
					333-	333-				
FO *Pseudoemiliania lacunosa*	0.436	0.436	0.436	0	C0011C-1H-CC	C0011C-2H-CC	3.495	12.837	8.166	1.87
LCO *Reticulofenestra asanoi*	0.901	0.905	0.903	0.002	C0011D-1H-CC	C0011D-2H-CC	30.251	39.703	34.977	5.74
LO *Gephyrocapsa* spp. (>3.5 µm)	1.67	1.67	1.67	0	C0011D-3H-CC	C0011D-4H-CC	48.616	55.313	51.9645	2.21
LO *Discoaster brouweri*	2.06	2.06	2.06	0	C0011D-4H-CC	C0011D-5H-CC	55.353	64.952	60.1525	2.10
LO *Discoaster pentaradiatus*	2.393	2.512	2.453	0.0595	C0011D-6H-CC	C0011D-7H-CC	74.5	78.977	76.7385	4.23
LO *Discoaster tamalis*	2.87	2.87	2.87	0	C0011D-8H-CC	C0011D-9H-CC	81.498	90.446	85.972	2.21
LO *Reticulofenestra pseudoumbilicus*	3.79	3.79	3.79	0	C0011D-15H-CC	C0011D-16H-CC	143	149.952	146.476	6.58
FO *Amaurolithus* spp.	4.5	4.5	4.5	0	C0011D-28X-CC	C0011D-29X-CC	219.949	224.953	222.451	10.70
LO *Discoaster quinqueramus*	5.59	5.59	5.59	0	C0011D-35X-CC	C0011D-36X-CC	257.655	275.448	266.5515	4.05
PE *Reticulofenestra pseudoumbilicus* (>7 µm)	7.077	7.167	7.122	0.045	C0011D-47X-CC	C0011D-48X-CC	354.436	353.421	356.9285	5.90

Age based on Raffi et al. (2006). FO = first occurrence, LCO = last consistent occurrence, LO = last occurrence, PE = paracme end.

Table T8. Paleomagnetic age datums, Site C0011.

Datum	Boundary age (Ma)	Upper Core, section, interval (cm)	Upper Depth (mbsf)	Lower Core, section, interval (cm)	Lower Depth (mbsf)	Average depth (mbsf)	Note
Magnetic		333-C0011C-		333-C0011C-			
Brunhes/Matuyama	0.781	3H-5, 17.5–19.5	16.97	3H-5, 78–80	17.75	17.36	
		333-C0011D-		333-C0011D-			
Jaramillo top	0.988	1H-7, 85–87	27.51	1H-8, 25.5–27.5	28.08	27.80	
Jaramillo base	1.072	2H-2, 9.5–11.5	31.95	2H-2, 28–30	32.13	32.04	
Cobb Mountain	1.173–1.185						
Olduvai top	1.778	5H-2, 19–21	57.02	5H-2, 85–87	57.66	57.34	
Olduvai base	1.945	5H-6, 99–101	61.85	5H-7, 79–81	63.01	62.43	
Matuyama/Gauss	2.581	7H-2, 84–86	75.55	7H-3, 18–20	75.90	75.72	
Keana top	3.032	9H-2, 89–91	83.74	9H-5, 39–41	85.78	84.76	
Keana base	3.116	9H-7, 87–89	88.98	9H-8, 20–22	89.52	89.25	
Mammoth top	3.207	10H-4, 28–30	94.75	10H-6, 26–28	96.07	95.41	
Mammoth base	3.33	11H-3, 22–24	102.98	11H-6, 59.5–61.5	104.96	103.97	
Gauss/Gilbert	3.596	14H-2, 18–20	126.38	14H-2, 96–98	127.06	126.72	
Cochiti top	4.187	19H-6, 90–92	173.36	20H-3, 55–57	177.22	175.29	
Cochiti base	4.3	23T-2, 18–20	187.59	25T-1, 15–17	197.78	192.68	Relatively large error due to lack of data
Nunivak top	4.493	26X-4, 91–93	207.44	26X-6, 133–135	209.19	208.32	
Nunivak base	4.631	27X-5, 94–96	213.91	27X-CC, 2.5–4.5	214.79	214.35	
Sidufjall top	4.799	28X-4, 74–76	219.60	29X-2, 81–83	221.89	220.74	
Sidufjall base	4.896	30X-2, 40–42	226.80	30X-3, 127–129	228.90	227.85	Uncertain because of lack of data in the bottom
Thvera top	4.997	30X-3, 127–129	228.90	31X-1, 58–60	235.08	231.99	Uncertain because of lack of data in the top
Thvera base	5.235	33X-1, 94–96	247.37	33X-2, 85–87	248.57	247.97	
Gilbert/C3An.1n	6.033	37X-7, 22	281.78	38X-1, 132	283.82	282.80	
C3An.1n/C3An.1r	6.252	39X-3, 49	295.16	39X-4, 62	296.63	295.90	
C3An.1r/C3An.2n	6.436	40X-8, 22	309.53	41X-1, 86	311.86	310.70	
C3An.2n/C3Ar	6.733	41X-7, 135.5	319.54	42X-1, 84	320.80	320.17	
C3Ar/C3Bn	7.14	42X-7, 24	327.31	43X-4, 132	333.19	330.25	
C3Bn/C3Br.1r	7.212						
C3Br.1r/C3Br.1n	7.251						
C3Br.1n/C3Br.2r	7.285						
C3Br.2r/C3Br.2n	7.454						
C3Br.2n/C3Br.3r	7.489						
C3Br.3r/C4n.1n	7.528						
C4n.1n/C4n.1r	7.642						
C4n.1r/C4n.2n	7.695						
Tephra		333-C0011C-		333-C0011C-			
Azuki volcanic ash bed	0.85	3H-10, 10	21.10	3H-10, 27	21.26	21.18	
		333-C0011D-		333-C0011D-			
Pink volcanic ash bed	1.05	2H-1, 86	31.34	2H-1, 89	31.37	31.35	
Habutaki I volcanic ash bed	2.9	8H-2, 80	79.64	8H-CC, 8.5	81.48	80.56	Lower part is flow-in
Ohta volcanic ash bed	3.9	17H-9, 2	157.25	17H-9, 5	157.28	157.26	

Table T9. Moisture and density data on discrete samples, Site C0011. (Continued on next eight pages.)

Core, section, interval (cm)	Depth CSF (m)	Water content (wt%)	Density (g/cm^3)		Porosity (fractional)	Void ratio	Lithologic note
			Bulk	Grain			
333-C0011C-							
1H-1, 36	0.36	0.54	1.44	2.71	0.75	3.06	
1H-2, 20	0.83	0.45	1.50	2.43	0.66	1.94	
1H-3, 4	0.89	0.43	1.58	2.65	0.66	1.93	
1H-3, 44	1.29	0.41	1.59	2.60	0.64	1.78	
1H-3, 90	1.75	0.40	1.64	2.74	0.64	1.80	
1H-4, 19.5	2.06	0.47	1.49	2.49	0.68	2.13	
1H-5, 27	2.35	0.46	1.54	2.73	0.70	2.30	
1H-5, 75	2.83	0.49	1.48	2.58	0.71	2.39	
1H-5, 108.5	3.16	0.42	1.59	2.66	0.65	1.89	
2H-1, 24	3.74	0.42	1.60	2.70	0.66	1.92	
2H-1, 90	4.40	0.44	1.57	2.72	0.68	2.08	
2H-2, 19	4.87	0.47	1.52	2.70	0.70	2.36	
2H-3, 25	5.14	0.44	1.55	2.60	0.67	2.02	
2H-3, 106	5.95	0.43	1.55	2.56	0.66	1.92	
2H-4, 32	6.63	0.45	1.51	2.46	0.66	1.93	
2H-4, 104	7.35	0.44	1.54	2.61	0.67	2.04	
2H-5, 19.5	7.72	0.42	1.57	2.55	0.64	1.80	
2H-6, 26	8.00	0.43	1.55	2.55	0.65	1.89	
2H-6, 120	8.94	0.45	1.52	2.52	0.67	1.99	
2H-7, 15	9.30	0.43	1.57	2.59	0.65	1.87	
2H-7, 100	10.15	0.44	1.57	2.66	0.67	2.01	
2H-8, 19	10.54	0.44	1.55	2.62	0.67	2.01	
2H-9, 8	10.64	0.41	1.60	2.60	0.64	1.75	
2H-9, 38	10.94	0.44	1.55	2.59	0.66	1.95	
2H-9, 108	11.64	0.41	1.59	2.60	0.64	1.77	
2H-10, 20	11.96	0.42	1.58	2.57	0.64	1.78	
2H-11, 11	12.09	0.39	1.65	2.72	0.63	1.72	
2H-11, 88	12.86	0.42	1.56	2.54	0.65	1.82	
3H-1, 10	13.10	0.43	1.56	2.57	0.66	1.91	
3H-1, 47	13.47	0.39	1.61	2.50	0.61	1.54	
3H-1, 113	14.13	0.41	1.61	2.66	0.64	1.80	
3H-2, 40	14.81	0.41	1.62	2.72	0.65	1.86	
3H-2, 102	15.43	0.41	1.61	2.66	0.64	1.77	
3H-3, 14	15.96	0.39	1.61	2.55	0.61	1.59	
3H-3, 84	16.66	0.43	1.61	2.79	0.67	2.03	
3H-5, 13	17.18	0.42	1.60	2.69	0.66	1.92	
3H-6, 46	17.74	0.44	1.54	2.54	0.66	1.94	
3H-6, 104	18.32	0.39	1.65	2.69	0.63	1.67	
3H-7, 19	18.87	0.41	1.61	2.68	0.64	1.81	
3H-7, 77	19.45	0.41	1.61	2.66	0.64	1.81	
3H-8, 20	20.09	0.42	1.57	2.55	0.64	1.78	
3H-9, 20	20.31	0.42	1.60	2.68	0.66	1.90	
3H-9, 62	20.73	0.41	1.60	2.68	0.65	1.86	
3H-10, 21	21.73	0.36	1.62	2.41	0.57	1.35	Sand/Ash
3H-10, 85	22.37	0.40	1.61	2.61	0.63	1.73	
333-C0011D-							
1H-1, 31	21.31	0.43	1.56	2.60	0.66	1.92	
1H-1, 96	21.96	0.34	1.66	2.46	0.56	1.26	Sand/Ash
1H-2, 20	22.61	0.40	1.61	2.60	0.63	1.69	
1H-2, 91	23.32	0.39	1.61	2.56	0.62	1.62	
1H-3, 15	23.97	0.41	1.65	2.88	0.66	1.98	
1H-3, 53	24.35	0.41	1.59	2.55	0.63	1.70	
1H-3, 102	24.84	0.42	1.59	2.61	0.64	1.81	
1H-4, 20	25.43	0.40	1.65	2.75	0.64	1.76	
1H-5, 32	25.77	0.44	1.55	2.61	0.67	2.03	
1H-5, 92	26.37	0.42	1.57	2.52	0.64	1.76	
1H-6, 8	26.94	0.37	1.69	2.74	0.61	1.56	
1H-7, 25	27.33	0.41	1.58	2.57	0.64	1.78	
1H-7, 88	27.96	0.38	1.63	2.57	0.61	1.53	
1H-8, 27	28.54	0.37	1.63	2.50	0.59	1.43	
1H-8, 81	29.08	0.40	1.62	2.64	0.63	1.73	
1H-9, 21	29.90	0.42	1.57	2.56	0.65	1.83	
1H-9, 83	30.52	0.41	1.65	2.87	0.66	1.93	
2H-1, 25	30.75	0.39	1.65	2.74	0.63	1.74	
2H-1, 92	31.42	0.35	1.73	2.76	0.59	1.46	
2H-2, 20	32.10	0.41	1.61	2.67	0.65	1.84	
2H-2, 82	32.72	0.41	1.63	2.72	0.64	1.81	

Table T9 (continued). (Continued on next page.)

Core, section, interval (cm)	Depth CSF (m)	Water content (wt%)	Density (g/cm^3)		Porosity (fractional)	Void ratio	Lithologic note
			Bulk	Grain			
2H-2, 121	33.11	0.26	1.72	2.28	0.44	0.80	Sand/Ash
2H-5, 20	36.15	0.43	1.55	2.53	0.65	1.84	
2H-7, 20	36.60	0.39	1.59	2.49	0.61	1.58	
2H-7, 62	37.02	0.39	1.63	2.60	0.62	1.60	
2H-9, 44	39.35	0.38	1.65	2.63	0.61	1.57	
3H-1, 21	40.21	0.41	1.59	2.59	0.64	1.77	
3H-1, 78	40.78	0.41	1.60	2.66	0.65	1.82	
3H-2, 16	41.58	0.41	1.60	2.68	0.65	1.85	
3H-2, 110	42.52	0.39	1.63	2.60	0.62	1.61	
3H-3, 19	43.02	0.39	1.68	2.85	0.64	1.77	
3H-3, 61	43.44	0.39	1.62	2.62	0.62	1.66	
3H-3, 121	44.04	0.42	1.57	2.56	0.64	1.80	
3H-4, 35	44.60	0.39	1.63	2.65	0.63	1.68	
3H-5, 21.5	45.28	0.26	1.77	2.40	0.46	0.84	Sand/Ash
3H-6, 30	45.60	0.40	1.60	2.57	0.62	1.66	
3H-6, 87	46.17	0.40	1.62	2.63	0.63	1.72	
3H-7, 31	47.03	0.40	1.62	2.64	0.63	1.70	
3H-7, 60	47.32	0.38	1.64	2.59	0.61	1.56	
3H-8, 20	48.34	0.39	1.67	2.83	0.64	1.77	
3H-8, 43	48.57	0.40	1.59	2.50	0.62	1.62	
3H-8, 86.5	49.01	0.38	1.68	2.75	0.62	1.63	
4H-1, 21	49.21	0.39	1.61	2.56	0.62	1.62	
4H-1, 59	49.59	0.40	1.63	2.68	0.64	1.75	
4H-1, 111	50.11	0.39	1.62	2.57	0.61	1.58	
4H-2, 18	50.60	0.40	1.61	2.59	0.63	1.67	
4H-2, 84	51.26	0.40	1.63	2.68	0.63	1.71	
4H-2, 121	51.63	0.42	1.64	2.92	0.68	2.11	
4H-3, 20	52.04	0.40	1.63	2.64	0.63	1.69	
4H-3, 46	52.30	0.40	1.58	2.50	0.62	1.63	
4H-4, 17	52.63	0.40	1.61	2.61	0.63	1.70	
4H-5, 20.5	52.90	0.40	1.61	2.58	0.62	1.65	
4H-6, 38	53.30	0.40	1.63	2.71	0.64	1.78	
4H-6, 102	53.94	0.38	1.66	2.66	0.61	1.58	
4H-7, 25	54.36	0.40	1.61	2.59	0.63	1.68	
4H-7, 108	55.19	0.39	1.64	2.67	0.62	1.66	
4H-8, 56	56.09	0.37	1.67	2.64	0.60	1.50	
4H-8, 120	56.73	0.40	1.60	2.56	0.62	1.65	
5H-1, 26	55.76	0.41	1.60	2.59	0.63	1.73	
5H-1, 120	56.70	0.39	1.64	2.69	0.63	1.71	
5H-2, 5	56.96	0.39	1.64	2.67	0.63	1.68	
5H-2, 94	57.85	0.44	1.53	2.49	0.65	1.89	
5H-3, 10	58.42	0.39	1.60	2.52	0.62	1.60	
5H-3, 94	59.26	0.40	1.61	2.58	0.62	1.67	
5H-3, 124.5	59.56	0.42	1.62	2.79	0.66	1.97	
5H-4, 12	59.84	0.39	1.62	2.57	0.62	1.61	
5H-4, 88	60.60	0.40	1.60	2.58	0.63	1.70	
5H-5, 20	61.14	0.41	1.64	2.81	0.66	1.91	
5H-6, 35	61.51	0.41	1.57	2.50	0.63	1.71	
5H-6, 105	62.21	0.40	1.58	2.47	0.61	1.59	
5H-7, 13	62.70	0.37	1.65	2.55	0.59	1.45	
5H-7, 88	63.45	0.41	1.56	2.46	0.63	1.68	
5H-7, 119.5	63.77	0.41	1.58	2.52	0.63	1.71	
5H-8, 41	64.39	0.41	1.59	2.57	0.63	1.73	
5H-8, 95	64.93	0.45	1.55	2.68	0.68	2.13	
6H-1, 51	65.51	0.40	1.60	2.59	0.63	1.71	
6H-1, 132	66.32	0.39	1.61	2.54	0.61	1.58	
6H-2, 56	66.98	0.39	1.58	2.46	0.61	1.56	
6H-2, 130	67.72	0.41	1.59	2.60	0.64	1.79	
6H-3, 20	68.02	0.40	1.64	2.74	0.64	1.76	
6H-3, 50	68.32	0.41	1.59	2.57	0.63	1.71	
6H-4, 21.5	69.22	0.40	1.61	2.64	0.64	1.75	
6H-5, 4	69.28	0.42	1.55	2.45	0.63	1.71	
6H-5, 91	70.15	0.41	1.57	2.48	0.63	1.67	
6H-5, 124	70.48	0.43	1.57	2.61	0.66	1.90	
6H-6, 5	70.70	0.40	1.60	2.57	0.63	1.67	
6H-6, 106	71.71	0.41	1.59	2.56	0.63	1.73	
6H-7, 38	72.44	0.37	1.66	2.65	0.61	1.55	
6H-7, 104	73.10	0.39	1.63	2.63	0.62	1.66	
7H-1, 47	74.97	0.39	1.64	2.69	0.63	1.69	

Table T9 (continued). (Continued on next page.)

Core, section, interval (cm)	Depth CSF (m)	Water content (wt%)	Density (g/cm^3)		Porosity (fractional)	Void ratio	Lithologic note
			Bulk	Grain			
7H-1, 135	75.85	0.46	1.52	2.57	0.68	2.11	
7H-2, 30	76.20	0.40	1.61	2.62	0.63	1.74	
7H-2, 125	77.15	0.43	1.56	2.61	0.66	1.95	
7H-3, 31	77.62	0.44	1.56	2.61	0.66	1.97	
7H-3, 101	78.32	0.40	1.60	2.55	0.62	1.65	
7H-4, 20	78.92	0.40	1.64	2.73	0.64	1.76	
7H-5, 20	79.14	0.45	1.53	2.56	0.67	2.05	
7H-5, 74	79.68	0.44	1.58	2.76	0.68	2.11	
8H-1, 48	79.48	0.43	1.57	2.63	0.66	1.93	
8H-1, 114	80.14	0.47	1.53	2.74	0.71	2.41	
9H-1, 38	81.88	0.48	1.50	2.62	0.70	2.33	
9H-1, 96	82.46	0.47	1.51	2.61	0.69	2.27	
9H-2, 26	83.16	0.45	1.57	2.78	0.69	2.21	
9H-2, 93	83.83	0.43	1.56	2.61	0.66	1.96	
9H-3, 20	84.56	0.44	1.52	2.45	0.65	1.86	
9H-4, 18	84.76	0.42	1.56	2.51	0.64	1.77	
9H-4, 34	84.92	0.44	1.55	2.60	0.67	2.00	
9H-5, 45	85.94	0.46	1.50	2.51	0.68	2.13	
9H-6, 33	87.23	0.44	1.60	2.86	0.68	2.16	
9H-6, 80	87.70	0.43	1.56	2.55	0.65	1.85	
9H-7, 44	88.74	0.43	1.55	2.56	0.65	1.89	
9H-8, 30.5	89.82	0.44	1.56	2.61	0.66	1.98	
10H-1, 43	90.93	0.47	1.49	2.51	0.68	2.16	
10H-1, 68	91.18	0.45	1.53	2.57	0.67	2.05	
10H-1, 123	91.73	0.44	1.56	2.66	0.67	2.03	
10H-2, 40	92.28	0.42	1.58	2.65	0.65	1.90	
10H-2, 113	93.01	0.47	1.53	2.68	0.70	2.28	
10H-3, 38	93.68	0.45	1.53	2.55	0.67	2.02	
10H-3, 130	94.60	0.46	1.51	2.52	0.67	2.06	
10H-4, 22	94.91	0.46	1.52	2.60	0.69	2.18	
10H-4, 90	95.59	0.44	1.56	2.67	0.67	2.07	
10H-5, 21	96.09	0.45	1.52	2.50	0.66	1.97	
10H-6, 14	96.25	0.45	1.54	2.63	0.68	2.12	
10H-6, 101	97.12	0.45	1.54	2.65	0.68	2.15	
10H-7, 8	97.60	0.47	1.52	2.69	0.70	2.36	Sand/Ash
10H-7, 44	97.96	0.43	1.61	2.84	0.68	2.12	
10H-7, 52	98.04	0.45	1.54	2.61	0.67	2.08	
10H-7, 128	98.80	0.41	1.61	2.66	0.64	1.81	
10H-8, 22	99.15	0.44	1.57	2.68	0.67	2.06	
10H-8, 77	99.70	0.45	1.54	2.61	0.67	2.05	
11H-1, 33	100.33	0.44	1.55	2.60	0.67	2.00	
11H-1, 122	101.22	0.43	1.58	2.73	0.67	2.05	
11H-2, 25	101.67	0.44	1.59	2.80	0.68	2.15	
11H-2, 108	102.50	0.43	1.63	2.89	0.68	2.10	
11H-3, 41	103.25	0.44	1.54	2.56	0.67	1.99	
11H-3, 104.5	103.89	0.43	1.55	2.51	0.65	1.85	
11H-4, 12	104.17	0.45	1.51	2.52	0.67	2.05	
11H-5, 22	104.49	0.46	1.53	2.65	0.69	2.22	
11H-6, 24	104.75	0.45	1.55	2.64	0.68	2.09	
11H-6, 95	105.46	0.47	1.51	2.59	0.69	2.21	
11H-6, 121	105.72	0.46	1.53	2.63	0.69	2.20	
11H-7, 25	106.18	0.45	1.54	2.63	0.68	2.13	
11H-7, 103	106.96	0.44	1.54	2.54	0.66	1.97	
11H-8, 26	107.62	0.46	1.52	2.54	0.68	2.08	
11H-8, 90	108.26	0.46	1.53	2.68	0.69	2.25	
11H-9, 28	109.06	0.42	1.55	2.50	0.64	1.79	
12H-1, 40	109.90	0.42	1.51	2.32	0.62	1.66	
12H-1, 107	110.57	0.44	1.52	2.44	0.65	1.86	
12H-2, 103	111.90	0.46	1.53	2.68	0.69	2.27	
12H-2, 125	112.12	0.43	1.56	2.56	0.65	1.89	
12H-3, 43	112.71	0.49	1.46	2.41	0.69	2.22	
12H-3, 95	113.23	0.44	1.55	2.58	0.66	1.97	
12H-5, 20.5	114.69	0.44	1.54	2.53	0.66	1.94	
12H-6, 41	115.12	0.46	1.55	2.75	0.69	2.28	
12H-6, 117	115.88	0.43	1.56	2.60	0.66	1.94	
12H-7, 27	116.40	0.45	1.56	2.72	0.68	2.16	
12H-8, 20	117.79	0.45	1.55	2.66	0.68	2.09	
12H-8, 30	117.89	0.44	1.53	2.53	0.66	1.94	
13H-1, 31	119.31	0.44	1.52	2.45	0.65	1.85	

Table T9 (continued). (Continued on next page.)

Core, section, interval (cm)	Depth CSF (m)	Water content (wt%)	Density (g/cm^3)		Porosity (fractional)	Void ratio	Lithologic note
			Bulk	Grain			
13H-1, 91	119.91	0.47	1.48	2.47	0.68	2.15	
13H-2, 31	120.74	0.43	1.53	2.48	0.65	1.86	
13H-2, 83	121.26	0.47	1.52	2.65	0.69	2.25	
13H-2, 125	121.68	0.45	1.55	2.68	0.68	2.16	
13H-3, 31	122.15	0.46	1.54	2.68	0.69	2.23	
13H-3, 85	122.69	0.41	1.58	2.53	0.63	1.70	
13H-4, 51	123.36	0.45	1.56	2.70	0.68	2.15	
13H-5, 22.5	123.79	0.42	1.57	2.54	0.64	1.81	
13H-6, 16	123.97	0.43	1.57	2.65	0.67	1.99	
13H-6, 93	124.74	0.45	1.53	2.56	0.67	2.01	
13H-7, 30	125.53	0.43	1.56	2.54	0.65	1.84	
14H-1, 44	125.44	0.43	1.57	2.65	0.66	1.97	
14H-2, 32	126.73	0.44	1.55	2.64	0.67	2.06	
14H-2, 93	127.34	0.45	1.55	2.66	0.68	2.10	
14H-3, 15	127.97	0.42	1.61	2.74	0.66	1.92	
14H-3, 56	128.38	0.42	1.59	2.71	0.66	1.95	
14H-4, 20	129.43	0.42	1.59	2.63	0.65	1.86	
14H-5, 22	130.64	0.45	1.57	2.74	0.68	2.15	
14H-6, 36	131.02	0.46	1.51	2.49	0.67	2.04	
14H-6, 95	131.61	0.43	1.56	2.60	0.66	1.92	
14H-7, 22	132.32	0.43	1.57	2.66	0.67	1.99	
14H-7, 60	132.70	0.43	1.59	2.73	0.67	2.00	
14H-8, 20	133.71	0.43	1.57	2.61	0.66	1.92	
15H-1, 105	134.55	0.45	1.55	2.66	0.68	2.13	
15H-2, 23	135.15	0.46	1.53	2.63	0.68	2.15	
15H-3, 15	136.50	0.29	1.84	2.72	0.52	1.08	
15H-3, 36	136.71	0.44	1.55	2.60	0.66	1.98	
15H-4, 21.5	138.00	0.45	1.53	2.59	0.68	2.10	
15H-5, 26	138.28	0.44	1.54	2.53	0.66	1.95	
15H-5, 105	139.07	0.47	1.50	2.55	0.69	2.18	
15H-6, 31	139.75	0.44	1.55	2.58	0.66	1.96	
15H-7, 27	141.14	0.47	1.51	2.60	0.69	2.23	
15H-7, 125.5	142.12	0.46	1.57	2.93	0.71	2.47	
15H-8, 21	142.49	0.42	1.58	2.63	0.65	1.89	
15H-8, 63	142.91	0.46	1.57	2.83	0.70	2.33	
16H-1, 91	143.91	0.48	1.49	2.59	0.70	2.35	
16H-2, 10	144.41	0.44	1.59	2.81	0.68	2.15	
16H-3, 23	144.81	0.47	1.51	2.62	0.69	2.27	
16H-3, 92	145.50	0.43	1.57	2.64	0.66	1.98	
16H-4, 10	145.68	0.45	1.54	2.63	0.68	2.13	
16H-4, 71	146.29	0.43	1.60	2.76	0.67	2.04	
16H-5, 19	146.59	0.45	1.54	2.59	0.67	2.04	
16H-5, 92	147.32	0.45	1.54	2.58	0.67	2.04	
16H-6, 80	148.61	0.40	1.63	2.73	0.64	1.81	
17H-1, 120	151.20	0.39	1.63	2.64	0.63	1.68	
17H-2, 25	151.68	0.43	1.60	2.80	0.68	2.08	
17H-2, 111	152.54	0.40	1.63	2.72	0.64	1.80	
17H-3, 31	153.17	0.40	1.59	2.54	0.62	1.65	
17H-3, 100	153.86	0.42	1.59	2.67	0.66	1.91	
17H-4, 11	154.17	0.44	1.56	2.63	0.67	1.99	
17H-5, 20	154.51	0.44	1.56	2.65	0.67	2.04	
17H-5, 70	155.01	0.43	1.58	2.66	0.66	1.92	
17H-5, 134	155.65	0.45	1.55	2.65	0.68	2.10	
17H-6, 20.5	155.94	0.42	1.58	2.64	0.66	1.91	
17H-7, 31	156.27	0.45	1.55	2.66	0.68	2.10	
17H-7, 88	156.84	0.44	1.55	2.58	0.66	1.98	
17H-8, 30	157.47	0.43	1.54	2.49	0.65	1.86	
17H-8, 111	158.28	0.44	1.55	2.59	0.66	1.95	
17H-9, 41	158.99	0.44	1.56	2.61	0.66	1.98	
18H-2, 120	159.91	0.43	1.56	2.58	0.66	1.92	
18H-3, 30	160.42	0.45	1.54	2.62	0.67	2.08	
18H-3, 125	161.37	0.43	1.56	2.56	0.65	1.86	
18H-4, 21.5	161.74	0.46	1.51	2.52	0.68	2.08	
18H-5, 54	162.30	0.42	1.58	2.62	0.65	1.87	
18H-5, 124	163.00	0.42	1.61	2.72	0.66	1.91	
18H-6, 28	163.46	0.40	1.64	2.72	0.64	1.74	
18H-6, 126	164.44	0.43	1.57	2.64	0.66	1.97	
18H-7, 30	164.90	0.41	1.62	2.69	0.64	1.81	
18H-7, 110	165.70	0.43	1.57	2.58	0.65	1.86	

Table T9 (continued). (Continued on next page.)

Core, section, interval (cm)	Depth CSF (m)	Water content (wt%)	Density (g/cm^3)		Porosity (fractional)	Void ratio	Lithologic note
			Bulk	Grain			
18H-8, 30	166.31	0.43	1.57	2.65	0.66	1.95	
18H-8, 110	167.11	0.42	1.59	2.67	0.66	1.91	
18H-9, 20	167.61	0.43	1.60	2.75	0.67	2.02	
19H-1, 30	168.30	0.44	1.54	2.55	0.67	1.99	
19H-1, 80	168.80	0.45	1.52	2.53	0.67	2.01	
19H-2, 20	169.61	0.43	1.57	2.59	0.65	1.88	
19H-2, 102	170.43	0.45	1.52	2.51	0.67	1.99	
19H-3, 20	171.04	0.45	1.54	2.63	0.68	2.12	
19H-4, 23	171.29	0.43	1.58	2.71	0.67	2.03	
19H-4, 89	171.95	0.44	1.56	2.62	0.67	2.00	
19H-4, 127	172.33	0.45	1.56	2.69	0.68	2.13	
19H-5, 24	172.73	0.44	1.58	2.79	0.68	2.16	
19H-5, 89	173.38	0.44	1.55	2.61	0.67	2.00	
19H-5, 119	173.68	0.43	1.59	2.73	0.67	2.01	
19H-6, 22	174.11	0.42	1.57	2.59	0.65	1.86	
19H-6, 88	174.77	0.44	1.56	2.62	0.67	2.01	
20H-2, 23	175.64	0.44	1.54	2.57	0.67	1.99	
20H-2, 100	176.41	0.45	1.56	2.67	0.68	2.09	
20H-3, 20	177.03	0.43	1.57	2.61	0.66	1.90	
20H-3, 89	177.72	0.43	1.60	2.77	0.67	2.02	
20H-4, 20	178.21	0.45	1.57	2.77	0.69	2.21	
20H-5, 12	178.35	0.44	1.58	2.81	0.69	2.18	
20H-5, 83	179.06	0.41	1.60	2.66	0.65	1.83	
20H-6, 18	179.84	0.42	1.61	2.75	0.66	1.96	
21H-1, 25	180.75	0.42	1.59	2.63	0.65	1.82	
21H-1, 94	181.44	0.45	1.58	2.79	0.69	2.20	
21H-2, 21	182.11	0.42	1.59	2.68	0.66	1.92	
21H-2, 87	182.77	0.43	1.57	2.58	0.65	1.86	
21H-2, 120	183.10	0.38	1.66	2.66	0.61	1.58	
21H-3, 9	183.40	0.39	1.65	2.73	0.63	1.73	
21H-4, 20.5	183.74	0.41	1.61	2.66	0.64	1.79	
21H-5, 8	183.84	0.43	1.58	2.68	0.66	1.96	
21H-5, 20	183.96	0.45	1.53	2.58	0.67	2.07	
21H-5, 70	184.46	0.38	1.68	2.82	0.63	1.72	
21H-5, 95	184.71	0.41	1.61	2.69	0.65	1.83	
21H-6, 15	185.11	0.41	1.58	2.58	0.64	1.78	
22H-1, 40	184.90	0.42	1.59	2.70	0.66	1.95	
22H-1, 103	185.53	0.41	1.61	2.68	0.65	1.83	
22H-2, 16	186.06	0.43	1.55	2.51	0.64	1.81	
23T-2, 38	187.79	0.45	1.57	2.72	0.68	2.13	
23T-2, 126	188.67	0.45	1.56	2.72	0.69	2.19	
23T-3, 27.5	189.09	0.43	1.59	2.74	0.67	2.04	
23T-3, 103	189.85	0.43	1.59	2.71	0.67	2.00	
24T-1, 43	195.93	0.47	1.53	2.74	0.71	2.39	
24T-2, 108	197.50	0.51	1.39	2.22	0.69	2.27	
25T-1, 20	200.20	0.43	1.56	2.55	0.65	1.87	
25T-2, 29	201.15	0.45	1.55	2.68	0.68	2.14	
25T-3, 38	201.55	0.44	1.55	2.57	0.66	1.93	
25T-3, 118	202.35	0.44	1.57	2.67	0.67	2.02	
25T-4, 16	202.73	0.47	1.51	2.57	0.69	2.20	
25T-4, 61	203.18	0.44	1.57	2.70	0.68	2.09	
25T-4, 110	203.67	0.44	1.60	2.85	0.68	2.17	
26X-1, 42	205.42	0.47	1.53	2.70	0.70	2.30	
26X-1, 56	205.56	0.44	1.61	2.89	0.69	2.20	
26X-1, 92	205.92	0.43	1.57	2.59	0.65	1.89	
26X-1, 134	206.34	0.45	1.53	2.60	0.68	2.11	
26X-2, 40	206.81	0.34	1.62	2.32	0.54	1.19	
26X-2, 118	207.59	0.45	1.52	2.52	0.67	1.99	
26X-3, 30.5	208.13	0.47	1.51	2.58	0.69	2.20	
26X-4, 14	208.29	0.42	1.59	2.67	0.66	1.90	
26X-5, 23	209.46	0.43	1.57	2.65	0.66	1.97	
26X-5, 112	210.35	0.43	1.60	2.79	0.68	2.09	
26X-6, 27	210.91	0.48	1.52	2.70	0.71	2.40	
26X-6, 102	211.66	0.44	1.58	2.75	0.68	2.11	
26X-7, 24	212.28	0.45	1.55	2.64	0.68	2.09	
26X-7, 86	212.90	0.41	1.66	2.90	0.66	1.95	
27X-1, 107	211.07	0.41	1.60	2.64	0.64	1.79	
27X-2, 44	211.85	0.38	1.66	2.69	0.62	1.62	
27X-2, 105	212.46	0.40	1.68	2.92	0.65	1.89	

Table T9 (continued). (Continued on next page.)

Core, section, interval (cm)	Depth CSF (m)	Water content (wt%)	Density (g/cm^3)		Porosity (fractional)	Void ratio	Lithologic note
			Bulk	Grain			
27X-3, 30.5	213.15	0.47	1.49	2.49	0.68	2.15	
27X-4, 62	213.79	0.44	1.51	2.45	0.66	1.91	
27X-5, 37	214.64	0.39	1.63	2.62	0.62	1.65	
27X-5, 118	215.45	0.39	1.67	2.78	0.63	1.70	
27X-6, 21	215.89	0.42	1.60	2.66	0.65	1.85	
28X-1, 32	215.32	0.41	1.66	2.89	0.66	1.93	
28X-1, 97	215.97	0.43	1.51	2.34	0.63	1.71	
28X-2, 17	216.59	0.44	1.52	2.46	0.65	1.87	
28X-2, 36	216.78	0.39	1.65	2.66	0.62	1.64	
28X-3, 45	218.27	0.44	1.60	2.81	0.68	2.13	
28X-3, 124	219.06	0.41	1.64	2.87	0.66	1.98	
28X-4, 38	219.61	0.41	1.59	2.60	0.64	1.80	
29X-1, 46	220.46	0.46	1.50	2.45	0.67	2.01	
29X-1, 132	221.32	0.43	1.54	2.51	0.65	1.85	
29X-2, 35	221.76	0.39	1.64	2.70	0.63	1.72	
29X-2, 115	222.56	0.41	1.61	2.68	0.64	1.81	
29X-3, 25	223.07	0.46	1.50	2.47	0.67	2.02	
29X-4, 31	224.22	0.43	1.56	2.60	0.66	1.92	
29X-5, 40	224.64	0.42	1.59	2.65	0.65	1.85	
29X-5, 85	225.09	0.42	1.60	2.69	0.65	1.88	
30X-1, 75	225.75	0.44	1.59	2.77	0.68	2.09	
30X-2, 31	226.71	0.37	1.65	2.58	0.60	1.50	
30X-2, 103	227.43	0.44	1.59	2.83	0.69	2.18	
30X-3, 20	227.83	0.45	1.58	2.79	0.69	2.19	
30X-3, 128	228.91	0.44	1.59	2.75	0.67	2.07	
31X-1, 22	234.72	0.44	1.59	2.85	0.69	2.21	
31X-1, 58	235.08	0.45	1.57	2.79	0.69	2.24	
31X-2, 40	236.29	0.47	1.55	2.82	0.71	2.42	
31X-3, 45	237.75	0.25	2.16	3.41	0.52	1.10	
31X-4, 29	238.43	0.47	1.52	2.65	0.70	2.32	
31X-5, 20	238.65	0.45	1.54	2.60	0.67	2.04	
31X-5, 47	238.92	0.43	1.61	2.85	0.68	2.12	
31X-5, 76	239.21	0.46	1.56	2.79	0.69	2.27	
31X-5, 97	239.42	0.47	1.50	2.59	0.69	2.27	
31X-6, 32	240.18	0.44	1.56	2.67	0.67	2.04	
32X-1, 13	241.63	0.43	1.56	2.60	0.66	1.92	
32X-1, 98	242.48	0.49	1.47	2.57	0.71	2.44	
32X-2, 20	243.11	0.45	1.58	2.85	0.69	2.27	
32X-2, 100	243.91	0.43	1.55	2.57	0.66	1.91	
32X-3, 7	244.39	0.48	1.49	2.61	0.70	2.38	
32X-5, 22	245.13	0.47	1.52	2.69	0.70	2.37	
32X-5, 101	245.92	0.41	1.57	2.48	0.62	1.65	
32X-6, 23	246.55	0.43	1.65	3.05	0.69	2.26	
33X-1, 13	246.63	0.44	1.58	2.70	0.67	2.04	
33X-1, 91	247.41	0.48	1.49	2.59	0.70	2.37	
33X-2, 25	248.14	0.44	1.54	2.56	0.67	1.99	
33X-2, 83	248.72	0.44	1.55	2.60	0.67	2.02	
33X-3, 30.5	249.36	0.40	1.66	2.86	0.65	1.87	
33X-4, 22	249.60	0.47	1.49	2.50	0.68	2.13	
33X-4, 37	249.75	0.42	1.60	2.69	0.66	1.92	
33X-4, 100	250.38	0.46	1.51	2.54	0.68	2.13	
33X-5, 48	251.26	0.43	1.58	2.71	0.67	2.03	
34X-1, 24	251.74	0.39	1.68	2.82	0.64	1.74	
34X-1, 132	252.82	0.32	1.77	2.71	0.56	1.26	
34X-2, 76	253.67	0.31	1.78	2.68	0.55	1.20	
34X-2, 139	254.30	0.37	1.71	2.79	0.61	1.58	
34X-3, 21	254.53	0.33	1.73	2.64	0.56	1.29	
34X-3, 119	255.51	0.33	1.76	2.76	0.57	1.35	
34X-4, 34	256.11	0.33	1.74	2.68	0.57	1.30	
34X-5, 60	256.73	0.32	1.78	2.74	0.56	1.27	
34X-5, 113	257.26	0.33	1.76	2.76	0.57	1.35	
34X-6, 45	257.99	0.33	1.73	2.62	0.56	1.25	
34X-CC, 25	258.59	0.32	1.79	2.76	0.56	1.25	
35X-1, 13	256.63	0.32	1.76	2.68	0.55	1.25	
36X-1, 36	266.36	0.32	1.78	2.72	0.55	1.24	
36X-1, 122	267.22	0.32	1.77	2.71	0.55	1.24	
36X-2, 55	267.96	0.30	1.82	2.70	0.53	1.12	
36X-3, 32	269.15	0.30	1.82	2.76	0.54	1.17	
36X-3, 110	269.93	0.30	1.84	2.78	0.54	1.16	

Table T9 (continued). (Continued on next page.)

Core, section, interval (cm)	Depth CSF (m)	Water content (wt%)	Density (g/cm^3)		Porosity (fractional)	Void ratio	Lithologic note
			Bulk	Grain			
36X-4, 51	270.74	0.30	1.82	2.75	0.54	1.16	
36X-5, 34	271.62	0.31	1.80	2.75	0.55	1.23	
36X-6, 23	271.87	0.33	1.77	2.77	0.57	1.34	
36X-6, 110	272.74	0.30	1.78	2.63	0.53	1.11	
36X-7, 31	273.36	0.31	1.77	2.61	0.53	1.13	
36X-7, 110	274.15	0.31	1.79	2.70	0.54	1.17	
36X-8, 55	275.01	0.30	1.81	2.68	0.52	1.10	
36X-8, 93	275.39	0.34	1.72	2.67	0.57	1.35	
37X-1, 62	276.12	0.35	1.74	2.76	0.59	1.44	
37X-1, 111	276.61	0.31	1.81	2.73	0.54	1.17	
37X-2, 25	277.13	0.34	1.71	2.63	0.57	1.34	
37X-2, 97	277.85	0.33	1.77	2.71	0.56	1.28	
37X-3, 18	278.47	0.35	1.70	2.65	0.59	1.42	
37X-3, 50	278.79	0.30	1.83	2.77	0.54	1.16	
37X-3, 130	279.59	0.37	1.68	2.67	0.60	1.50	
37X-4, 32.5	280.03	0.32	1.75	2.63	0.55	1.22	
37X-5, 21	280.26	0.36	1.68	2.62	0.59	1.45	
37X-5, 66	280.71	0.35	1.71	2.69	0.58	1.41	
37X-6, 9	281.22	0.33	1.74	2.64	0.56	1.26	
37X-7, 38	282.51	0.36	1.66	2.57	0.59	1.41	
38X-1, 131	283.81	0.37	1.67	2.65	0.61	1.54	
38X-2, 50	284.41	0.29	1.86	2.76	0.52	1.08	
38X-2, 98	284.89	–0.14	2.42	2.08	–0.33	–0.25	
38X-3, 35	285.67	0.37	1.68	2.67	0.60	1.52	
38X-4, 47	286.16	0.30	1.81	2.74	0.54	1.17	
38X-5, 19	286.47	0.32	1.79	2.77	0.56	1.27	
38X-5, 38	286.66	0.31	1.79	2.66	0.53	1.15	
38X-5, 111	287.39	0.30	1.79	2.64	0.53	1.11	
38X-6, 74	288.42	0.35	1.72	2.72	0.59	1.43	
38X-7, 15	289.31	0.36	1.73	2.83	0.61	1.56	
39X-1, 19	292.19	0.29	1.81	2.61	0.51	1.03	
39X-1, 114	293.14	0.29	1.83	2.68	0.51	1.05	
39X-1, 126	293.26	0.26	1.91	2.76	0.49	0.96	
39X-2, 68	294.08	0.30	1.80	2.66	0.52	1.10	
39X-3, 48	295.29	0.29	1.82	2.66	0.52	1.07	
39X-3, 125	296.06	0.30	1.80	2.65	0.52	1.09	
39X-4, 60	296.81	0.27	1.90	2.80	0.51	1.04	
39X-5, 35	297.61	0.29	1.82	2.66	0.51	1.06	
39X-6, 74	298.37	0.33	1.76	2.75	0.57	1.33	
39X-7, 99	300.04	0.30	1.81	2.70	0.53	1.13	
39X-7, 124	300.29	0.31	1.74	2.54	0.53	1.12	
39X-8, 22	300.69	0.31	1.76	2.59	0.53	1.14	
39X-8, 36	300.83	0.30	1.75	2.52	0.51	1.06	
40X-1, 40	301.90	0.37	1.67	2.66	0.61	1.54	
40X-1, 111	302.61	0.29	1.83	2.72	0.53	1.11	
40X-2, 98	303.89	0.29	1.83	2.68	0.51	1.05	
40X-2, 125	304.16	0.32	1.78	2.69	0.55	1.21	
40X-3, 72	305.04	0.28	1.85	2.73	0.51	1.06	
40X-4, 62	306.35	0.30	1.78	2.59	0.52	1.06	
40X-5, 40	306.94	0.29	1.79	2.56	0.50	1.00	
40X-6, 67	307.63	0.31	1.78	2.66	0.54	1.17	
40X-7, 68	309.05	0.28	1.84	2.68	0.51	1.03	
40X-8, 18	309.96	0.27	1.89	2.77	0.51	1.02	
41X-2, 30	312.65	0.30	1.84	2.79	0.54	1.16	
41X-2, 133	313.68	0.28	1.86	2.68	0.50	0.99	
41X-3, 32	314.08	0.32	1.76	2.65	0.55	1.22	
41X-3, 102	314.78	0.29	1.85	2.77	0.52	1.10	
41X-4, 38	315.56	0.28	1.87	2.78	0.52	1.07	
41X-4, 106	316.24	0.32	1.76	2.66	0.55	1.21	
41X-5, 38.5	316.76	0.27	1.86	2.69	0.50	0.99	
41X-6, 71	317.49	0.31	1.77	2.64	0.54	1.16	
41X-6, 120	317.98	0.29	1.84	2.72	0.52	1.08	
41X-7, 43	318.62	0.29	1.83	2.67	0.51	1.05	
41X-7, 119	319.38	0.28	1.86	2.75	0.52	1.07	
42X-1, 83	320.83	0.30	1.81	2.69	0.53	1.13	
42X-2, 2	321.43	0.29	1.84	2.69	0.51	1.05	
42X-2, 89	322.30	0.28	1.87	2.78	0.51	1.06	
42X-3, 86	323.67	0.39	1.64	2.71	0.63	1.72	
42X-5, 36	324.98	0.32	1.80	2.85	0.57	1.34	

Table T9 (continued). (Continued on next page.)

Core, section, interval (cm)	Depth CSF (m)	Water content (wt%)	Density (g/cm^3)		Porosity (fractional)	Void ratio	Lithologic note
			Bulk	Grain			
42X-5, 108	325.70	0.28	1.86	2.74	0.51	1.05	
42X-6, 44	326.47	0.29	1.79	2.55	0.50	1.00	
42X-7, 23	327.67	0.27	1.83	2.61	0.49	0.96	
42X-8, 28	329.12	0.26	1.88	2.65	0.48	0.90	
43X-1, 33	329.83	0.31	1.82	2.80	0.55	1.22	
43X-1, 127	330.77	0.28	1.82	2.61	0.50	1.01	
43X-2, 29	331.17	0.29	1.79	2.56	0.50	1.02	
43X-2, 121	332.09	0.29	1.81	2.62	0.51	1.05	
43X-3, 35.5	332.65	0.30	1.77	2.60	0.52	1.10	
43X-4, 42	333.09	0.32	1.74	2.61	0.55	1.21	
43X-4, 133	334.00	0.31	1.82	2.77	0.55	1.20	
43X-5, 45	334.53	0.29	1.83	2.71	0.52	1.09	
43X-5, 105	335.13	0.30	1.76	2.56	0.52	1.10	
44X-1, 25	334.75	0.30	1.81	2.69	0.53	1.12	
44X-1, 69	335.19	0.29	1.82	2.68	0.52	1.09	
44X-1, 105	335.55	0.29	1.84	2.74	0.52	1.10	
44X-2, 63	336.54	0.30	1.75	2.52	0.52	1.08	
44X-3, 28	337.60	0.29	1.80	2.62	0.51	1.05	
44X-4, 20	337.92	0.29	1.81	2.67	0.52	1.07	
44X-4, 38	338.10	0.29	1.78	2.52	0.50	0.99	
44X-5, 19	338.31	0.32	1.79	2.75	0.56	1.26	
45X-1, 32	339.82	0.32	1.77	2.70	0.55	1.25	
45X-1, 128	340.78	0.29	1.85	2.76	0.53	1.11	
45X-2, 24	341.15	0.31	1.80	2.68	0.54	1.15	
45X-2, 121	342.12	0.31	1.82	2.77	0.55	1.20	
45X-3, 38.5	342.70	0.30	1.75	2.53	0.52	1.07	
45X-4, 90	343.62	0.26	1.91	2.78	0.49	0.97	
45X-5, 13	343.87	0.27	1.86	2.67	0.49	0.97	
45X-5, 45	344.19	0.33	1.77	2.73	0.56	1.30	
46X-1, 110	345.60	0.32	1.75	2.61	0.54	1.18	
46X-2, 33	346.23	0.29	1.83	2.70	0.52	1.07	
46X-2, 79	346.69	0.29	1.81	2.66	0.52	1.09	
46X-3, 39	347.30	0.29	1.80	2.60	0.51	1.03	
46X-4, 52	347.84	0.31	1.74	2.56	0.53	1.14	
46X-4, 97	348.29	0.33	1.73	2.65	0.56	1.28	Sand/Ash
46X-5, 25	348.98	0.30	1.79	2.66	0.53	1.14	Sand/Ash
47X-2, 1	350.89	0.21	2.03	2.76	0.42	0.72	
47X-2, 95	351.83	0.31	1.80	2.70	0.54	1.16	
47X-4, 24	352.53	0.31	1.76	2.61	0.54	1.15	
47X-6, 36	353.62	0.38	1.65	2.65	0.61	1.59	Sand/Ash
47X-6, 132	354.58	0.32	1.75	2.63	0.55	1.23	Sand/Ash
47X-7, 66	355.32	0.34	1.71	2.63	0.57	1.35	Sand/Ash
48X-1, 30	354.80	0.25	1.90	2.66	0.46	0.87	Sand/Ash
48X-1, 121	355.71	0.25	1.93	2.77	0.48	0.92	Sand/Ash
48X-2, 37	356.26	0.25	1.91	2.69	0.47	0.88	Sand/Ash
48X-2, 93	356.82	0.34	1.67	2.46	0.55	1.25	
48X-3, 38	357.29	0.31	1.80	2.74	0.55	1.20	
48X-4, 19	357.50	0.32	1.75	2.62	0.54	1.20	
48X-5, 81	358.53	0.24	2.54	4.84	0.60	1.52	Sand/Ash
48X-6, 18	359.30	0.26	1.84	2.59	0.48	0.91	Sand/Ash
49X-1, 93	360.43	0.32	1.79	2.75	0.55	1.24	
49X-1, 120	360.70	0.33	1.75	2.72	0.57	1.33	
49X-2, 14	361.03	0.29	1.77	2.54	0.51	1.03	
49X-2, 106	361.95	0.35	1.68	2.59	0.58	1.37	
49X-4, 35	363.14	0.33	1.77	2.75	0.57	1.30	
49X-4, 50	363.29	0.29	1.82	2.68	0.52	1.08	
49X-4, 71	363.50	0.26	1.82	2.52	0.47	0.87	
49X-4, 120	363.99	0.29	1.83	2.69	0.52	1.07	
49X-5, 59	364.79	0.38	1.64	2.62	0.62	1.60	
49X-5, 115	365.35	0.38	1.63	2.56	0.60	1.52	
49X-6, 5	365.66	0.33	1.70	2.53	0.55	1.23	
50X-1, 33	365.33	0.35	1.64	2.41	0.55	1.24	
50X-1, 130	366.30	0.35	1.68	2.54	0.57	1.32	
50X-2, 28	366.68	0.35	1.65	2.46	0.56	1.29	
50X-2, 103	367.43	0.40	1.59	2.53	0.62	1.66	
50X-3, 17	367.98	0.40	1.60	2.56	0.63	1.67	
50X-3, 115	368.96	0.31	1.73	2.53	0.53	1.12	
50X-4, 50	369.73	0.23	1.94	2.64	0.43	0.76	
51X-1, 30	370.30	0.24	1.95	2.70	0.45	0.81	Sand/Ash

Table T9 (continued).

Core, section, interval (cm)	Depth CSF (m)	Water content (wt%)	Density (g/cm^3)		Porosity (fractional)	Void ratio	Lithologic note
			Bulk	Grain			
51X-1, 110	371.10	0.23	1.94	2.61	0.43	0.74	
51X-2, 27	371.65	0.23	1.97	2.74	0.45	0.82	
51X-2, 81	372.19	0.25	1.91	2.68	0.47	0.87	
51X-3, 15	372.94	0.25	1.91	2.65	0.46	0.84	
51X-4, 17	373.41	0.21	2.01	2.69	0.41	0.69	
52X-1, 75	375.75	0.23	1.98	2.75	0.44	0.80	
52X-2, 89	377.29	0.29	1.82	2.63	0.51	1.03	
52X-3, 25	378.06	0.27	1.89	2.76	0.50	1.01	
52X-4, 37	378.93	0.27	1.88	2.70	0.49	0.95	

Table T10. *P*-wave velocity data for discrete samples, Hole C0011D. (Continued on next page.)

Core, section interval (cm)	Depth CSF (m)	Velocity (m/s)			α_{VPhor} (%)	α_{VPvert} (%)
		x-direction	*y*-direction	*z*-direction		
333-C0011D-						
28X-1, 62	215.62	1669	1753	1786	–4.91	–4.29
28X-2, 85	217.27	1687	1672	1674	0.89	0.33
28X-3, 66	218.48	1726	1670	1648	3.30	2.99
28X-4, 73	219.96	1735	1742	1720	–0.40	1.07
29X-1, 82	220.82	1669	1623	1648	2.79	–0.12
29X-2, 82	222.23	1674	1658	1667	0.96	–0.06
30X-1, 75	225.75	1672	1658	1671	0.84	–0.36
30X-3, 127	228.90	1698	1628	1712	4.21	–2.90
31X-1, 58	235.08	1653	1624	1603	1.77	2.19
31X-2, 27	236.16	1617	1636	1644	–1.17	–1.07
31X-5, 96	239.41	1621	1697	1684	–4.58	–1.50
32X-1, 101	242.51	1613	1574	1557	2.45	2.32
32X-2, 98	243.89	1669	1597	1645	4.41	–0.73
32X-5, 25	245.16	1644	1640	1626	0.24	0.98
33X-1, 94	247.44	1631	1593	1641	2.36	–1.78
33X-2, 85	248.74	1673	1734	1708	–3.58	–0.26
33X-4, 104	250.42	1706	1659	1633	2.79	2.99
33X-5, 52	251.30	1646	1700	1582	–3.23	5.59
34X-1, 61	252.11	1673	1650	1634	1.38	1.67
34X-1, 132	252.82	1735	1742	1727	–0.40	0.66
34X-2, 79	253.70	1707	1709	1683	–0.12	1.47
34X-3, 15	254.47	1680	1664	1634	0.96	2.30
35X-1, 68	257.18	1750	1711	1704	2.25	1.54
34X-5, 113	257.26	1680	1668	1669	0.72	0.30
36X-1, 51	266.51	1738	1682	1691	3.27	1.12
36X-2, 10	267.51	1725	1735	1691	–0.58	2.28
36X-3, 131	270.14	1716	1709	1695	0.41	1.03
36X-4, 30	270.53	1687	1692	1671	–0.30	1.10
36X-6, 58	272.22	1748	1751	1741	–0.17	0.49
36X-7, 62	273.67	1719	1634	1653	5.07	1.41
36X-8, 92	275.38	1696	1646	1656	2.99	0.90
37X-2, 97	277.85	1725	1692	1632	1.93	4.58
37X-3, 133	279.62	1674	1727	1652	–3.12	2.89
37X-5, 69	280.74	1636	1652	1657	–0.97	–0.79
37X-6, 16	281.29	1685	1743	1701	–3.38	0.76
37X-7, 22	282.35	1705	1663	1686	2.49	–0.12
38X-1, 132	283.82	1684	1624	1620	3.63	2.08
38X-2, 53	284.44	1692	1660	1689	1.91	–0.77
38X-4, 49	286.18	1719	1669	1646	2.95	2.87
38X-5, 113	287.41	1687	1646	1633	2.46	2.03
38X-6, 75	288.43	1664	1653	1644	0.66	0.88
38X-7, 15	289.31	1743	1674	1673	4.04	2.10
39X-1, 115	293.15	1792	1770	1661	1.24	6.97
39X-2, 69	294.09	1692	1696	1742	–0.24	–2.79
39X-3, 49	295.30	1763	1646	1638	6.86	3.98
39X-4, 62	296.83	1773	1697	1666	4.38	4.06
39X-6, 76	298.39	1768	1757	1742	0.62	1.17
39X-7, 99	300.04	1742	1736	1740	0.35	–0.06
39X-8, 99	301.46	1691	1704	1680	–0.77	1.04
40X-2, 96	303.87	1714	1732	1698	–1.04	1.46

Table T10 (continued).

Core, section interval (cm)	Depth CSF (m)	Velocity (m/s)			α_{VPhor} (%)	α_{VPvert} (%)
		x-direction	*y*-direction	*z*-direction		
40X-3, 64	304.96	1743	1746	1738	–0.17	0.37
40X-6, 68	307.64	1723	1720	1712	0.17	0.55
41X-1, 86	311.86	1726	1738	1699	–0.69	1.92
41X-2, 134	313.69	1744	1760	1705	–0.91	2.72
41X-3, 13	313.89	1747	1742	1728	0.29	0.95
41X-4, 38	315.56	1712	1676	1630	2.13	3.85
41X-6, 71	317.49	1734	1715	1678	1.10	2.73
41X-7, 36	318.55	1757	1731	1709	1.49	2.03
42X-1, 84	320.84	1675	1698	1648	–1.36	2.29
42X-2, 90	322.31	1693	1695	1665	–0.16	1.74
42X-3, 88	323.69	1732	1749	1719	–0.96	1.23
42X-5, 110	325.72	1688	1693	1673	–0.26	1.04
42X-7, 24	327.68	1712	1745	1682	–1.91	2.71
43X-1, 127	330.77	1686	1678	1671	0.49	0.66
43X-2, 121	332.09	1679	1667	1658	0.76	0.92
43X-4, 132	333.99	1693	1695	1663	–0.12	1.86
43X-5, 106	335.14	1675	1684	1655	–0.58	1.49
44X-1, 69.5	335.20	1724	1695	1724	1.65	–0.85
44X-2, 63	336.54	1703	1691	1702	0.67	–0.27
44X-3, 28	337.60	1697	1715	1665	–1.07	2.46
44X-5, 20	338.32	1699	1703	1678	–0.24	1.34
44X-6, 19	338.94	1703	1710	1672	–0.42	2.06
45X-1, 90	340.40	1725	1712	1711	0.75	0.45
45X-2, 24	341.15	1693	1694	1683	–0.06	0.64
45X-4, 90	343.62	1710	1685	1686	1.45	0.69
46X-2, 33	346.23	1727	1730	1697	–0.18	1.87
46X-4, 96	348.28	1730	1718	1723	0.73	0.06
46X-5, 25	348.98	2028	1989	2017	1.92	–0.42
47X-2, 1	350.89	2184	2161	2180	1.06	–0.34
47X-3, 4	351.93	1769	1792	1753	–1.31	1.58
47X-5, 29	353.15	1795	1832	1712	–2.02	5.75
48X-2, 73	356.62	1755	1757	1765	–0.11	–0.49
48X-4, 19	357.50	1884	1886	1881	–0.06	0.23
48X-5, 66	358.38	2203	2200	2188	0.12	0.61
49X-1, 120	360.70	1713	1721	1662	–0.50	3.26
49X-2, 106	361.95	1698	1692	1678	0.33	1.04
49X-4, 36	363.15	1713	1741	1670	–1.60	3.35
49X-5, 24	364.44	1877	1859	1799	0.99	3.78
51X-1, 50	370.50	1886	1885	1848	0.08	2.00
51X-3, 30	373.09	2141	2040	2218	4.79	–5.92
52X-1, 74.5	375.75	2359	2406	2333	–1.96	2.12
52X-2, 89	377.29	1709	1722	1688	–0.78	1.58
52X-3, 27	378.08	1737	1739	1706	–0.15	1.86
52X-5, 36	379.31	1749	1746	1738	0.22	0.55

Table T11. Electrical resistivity data for discrete samples, Hole C0011D. (Continued on next page.)

Core, section interval (cm)	Depth CSF (m)	Resistivity (Ωm)			α_{phor} (%)	α_{pvert} (%)
		x-direction	*y*-direction	*z*-direction		
333-C0011D-						
28X-1, 62	215.63	1.19	1.44	1.50	–19.10	–13.51
28X-2, 85	217.28	1.04	1.19	0.84	–14.10	28.19
28X-3, 66	218.49	1.10	0.96	0.79	13.43	26.52
28X-4, 73	219.97	0.97	0.76	0.78	24.26	9.62
29X-1, 82	220.83	0.74	0.71	0.76	3.77	–4.11
29X-2, 82	222.24	0.79	0.83	0.90	–4.68	–10.48
30X-1, 75	225.76	0.77	0.75	0.81	3.20	–5.94
30X-3, 127	228.91	0.72	0.77	0.75	–6.10	–0.13
31X-1, 58	235.09	0.66	0.62	0.63	6.26	1.62
31X-2, 27	236.17	0.61	0.59	0.61	2.81	–2.55
31X-5, 96	239.42	0.68	0.66	0.69	3.88	–3.37
32X-1, 101	242.52	0.71	0.74	0.70	–3.41	4.25
32X-2, 98	243.90	0.78	0.77	0.73	0.77	5.79
32X-5, 25	245.17	0.87	0.83	0.83	4.32	1.52
33X-1, 94	247.45	0.72	0.70	0.90	3.70	–24.01
33X-2, 85	248.75	0.74	0.74	0.73	0.37	1.14
33X-4, 104	250.43	0.82	0.78	0.76	5.60	4.85
33X-5, 52	251.31	0.76	0.74	0.77	2.70	–2.80
34X-1, 61	252.12	0.95	0.87	0.87	8.44	4.13
34X-1, 132	252.83	0.96	1.03	1.39	–7.36	–32.91
34X-2, 79	253.71	0.90	0.96	1.01	–6.39	–8.85
34X-3, 15	254.48	0.87	1.03	1.00	–16.17	–5.23
34X-4, 113	257.19	0.92	0.88	1.07	3.60	–17.17
35X-1, 68	257.27	0.92	0.89	1.03	3.72	–12.53
36X-1, 51	266.52	0.97	1.14	0.94	–15.98	12.13
36X-2, 10	267.52	1.02	0.94	1.07	8.00	–8.81
36X-3, 131	270.15	1.03	0.97	1.17	5.71	–15.17
36X-4, 30	270.54	1.07	1.17	1.04	–8.49	7.60
36X-6, 58	272.23	1.02	0.98	1.04	3.90	–3.99
36X-7, 62	273.68	1.01	1.01	1.11	0.10	–9.71
36X-8, 92	275.39	0.97	0.97	1.09	–0.19	–11.43
37X-2, 97	277.86	1.01	1.09	1.18	–7.66	–11.21
37X-3, 133	279.63	1.06	1.07	1.13	–0.32	–5.99
37X-5, 69	280.75	1.18	1.09	1.18	8.06	–4.07
37X-6, 16	281.30	1.19	1.21	2.14	–1.08	–56.36
37X-7, 22	282.36	1.09	1.11	1.26	–1.76	–13.66
38X-1, 132	283.83	1.07	1.05	1.11	1.49	–4.33
38X-2, 53	284.45	1.21	1.14	1.30	5.41	–9.79
38X-4, 49	286.19	1.02	0.99	1.10	3.02	–9.23
38X-5, 113	287.42	1.02	1.01	1.10	1.42	–7.70
38X-6, 75	288.44	1.02	0.98	1.06	3.90	–5.46
38X-7, 15	289.32	1.00	0.97	1.07	3.06	–7.94
39X-1, 115	293.16	1.10	1.08	1.19	2.07	–8.67
39X-2, 69	294.10	1.14	1.28	1.08	–11.54	10.81
39X-3, 49	295.31	1.04	1.05	1.19	–1.67	–13.24
39X-4, 62	296.84	1.13	1.16	1.29	–2.40	–11.68
39X-6, 76	298.40	1.21	1.04	1.15	14.96	–2.84
39X-7, 93	300.05	1.24	1.13	1.76	9.37	–38.83
39X-8, 99	301.47	1.14	1.09	1.50	4.79	–29.81
40X-2, 96	303.88	1.10	0.99	1.17	10.13	–11.05
40X-3, 64	304.97	1.04	0.99	1.06	5.36	–4.64
40X-6, 68	307.65	1.24	1.09	1.17	13.32	–0.54
41X-1, 86	311.87	1.10	1.17	1.24	–6.46	–8.71
41X-2, 134	313.70	1.13	1.11	1.22	1.68	–8.34
41X-3, 13	313.90	1.04	1.05	1.17	–0.73	–10.96
41X-4, 38	315.57	1.04	0.98	1.19	5.44	–16.28
41X-6, 71	317.50	0.91	1.29	1.34	–34.05	–19.47
41X-7, 36	318.56	1.00	1.02	1.23	–2.01	–19.56
42X-1, 84	320.85	1.10	1.10	1.25	–0.44	–12.87
42X-2, 90	322.32	1.14	1.03	1.21	10.20	–10.48
42X-3, 88	323.70	0.83	0.78	0.84	7.15	–3.85
42X-5, 110	325.73	1.10	1.06	1.21	2.81	–11.40
42X-7, 24	327.69	1.10	1.36	1.36	–20.46	–9.73
43X-1, 127	330.78	1.11	1.06	1.31	5.20	–19.17
43X-2, 121	332.10	1.10	1.10	1.35	–0.55	–20.20
43X-4, 132	334.00	1.06	1.05	1.17	0.84	–10.63
43X-5, 106	335.15	1.04	1.03	1.27	0.93	–20.22

Table T11 (continued).

Core, section interval (cm)	Depth CSF (m)	Resistivity (Ωm)			α_{phor} (%)	α_{pvert} (%)
		x-direction	*y*-direction	*z*-direction		
44X-1, 69.5	335.21	1.09	1.08	1.37	1.74	–23.37
44X-2, 63	336.55	1.01	1.11	1.22	–9.40	–14.22
44X-3, 28	337.61	1.01	1.01	1.39	–0.30	–31.82
44X-5, 20	338.33	1.03	0.99	1.28	4.15	–23.28
44X-6, 19	338.95	0.85	0.86	1.18	–1.46	–31.42
45X-1, 90	340.41	1.02	0.99	1.19	3.11	–16.76
45X-2, 24	341.16	1.01	1.00	1.20	1.31	–17.77
45X-4, 90	343.63	1.07	1.09	1.26	–2.16	–15.70
46X-2, 33	346.24	0.97	1.04	1.23	–6.42	–20.11
46X-4, 96	348.29	0.97	0.93	1.00	3.70	–5.67
46X-5, 25	348.99	1.32	1.27	1.30	4.40	–0.47
47X-2, 1	350.90	1.78	1.65	1.67	7.55	2.68
47X-3, 4	351.94	0.96	0.95	1.12	0.57	–16.51
47X-5, 29	353.16	1.09	0.95	1.55	13.55	–40.64
48X-2, 73	356.63	1.01	0.94	1.16	7.51	–17.30
48X-4, 19	357.51	1.09	1.08	1.26	0.33	–14.88
48X-5, 66	358.39	1.70	1.79	1.32	–4.71	28.03
49X-1, 120	360.71	0.88	0.89	1.39	–0.79	–44.62
49X-2, 106	361.96	0.97	0.94	1.10	3.15	–14.46
49X-4, 36	363.16	0.97	0.94	1.55	2.87	–47.23
49X-5, 24	364.45	1.03	1.03	1.21	–0.41	–16.02
51X-1, 50	370.51	1.61	1.53	1.69	5.18	–7.33
51X-3, 30	373.10	1.62	1.64	2.60	–1.14	–45.92
52X-1, 74.5	375.76	1.97	1.93	2.00	2.14	–2.45
52X-2, 89	377.30	1.08	1.10	1.41	–2.29	–25.66
52X-3, 27	378.09	1.16	1.08	1.34	7.51	–18.01
52X-5, 36	379.32	1.23	1.19	1.39	3.27	–13.90

Table T12. Interstitial water geochemistry (raw data), Holes C0011C and C0011D. (Continued on next page.)

Core, section	Whole-round length (cm)	Depth (mbsf)	pH	Alkalinity (mM)	Salinity	Chlorinity (mM)	Na^+ (mM)	NH_4^+ (mM)	Si (μM)	Ca^{2+} (mM)	Mg^{2+} (mM)	Sr (μM)	Li (μM)	K^+ (mM)	PO_4^{3-} (μM)	SO_4^{2-} (mM)	Mn (μM)	Br^- (mM)
333-C0011C-																		
1H-2	20	0.6	7.54	2.93	35.6	553	263	0.02	465	10.8	52.3	82	42	12.6	6.19	28.09	4.2	0.83
1H-4	19.5	1.8	7.43	3.64	35.4	551	323	0.05	513	10.7	51.6	81	39	12.2	6.91	27.41	9.6	0.83
2H-2	19	4.6	7.49	4.22	35.3	556	435	0.13	652	10.3	50.0	85	36	12.7	6.08	24.90	13.6	0.85
2H-5	19.5	7.4	7.36	4.89	35.3	555	434	0.20	629	10.2	48.9	84	35	12.6	8.29	23.09	15.8	0.88
2H-8	19	10.1	7.40	5.16	35.1	556	444	0.26	627	9.9	48.0	82	35	12.7	8.51	21.47	15.4	0.84
2H-10	20	11.4	7.71	4.96	35.1	559	471	0.30	616	9.2	45.3	80	40	13.5	8.02	20.63	14.6	0.85
3H-8	20	19.5	7.79	6.70	34.8	563	475	0.43	677	8.9	42.8	82	38	11.3	9.81	16.17	16.0	0.86
333-C0011D-																		
1H-4	20	25.0	7.71	7.17	34.5	564	473	0.53	786	8.4	40.6	81	42	12.7	9.96	13.50	12.0	0.87
2H-5	20	35.8	7.59	8.94	34.1	563	468	0.66	728	8.4	38.2	85	45	11.2	12.48	9.52	11.0	0.86
3H-5	21.5	44.8	7.58	9.67	33.9	564	469	0.76	683	8.3	35.7	87	48	10.6	11.16	6.91	9.7	0.89
4H-5	20.5	51.9	7.69	9.54	33.4	564	473	0.84	728	7.7	32.8	86	55	10.5	7.39	5.08	6.6	0.91
5H-5	20	60.7	7.75	9.77	33.4	564	475	0.92	715	7.7	30.9	85	59	10.4	5.67	3.56	4.7	0.90
6H-4	21.5	68.8	7.75	9.74	33.2	563	473	0.97	715	7.8	29.9	87	62	10.2	4.66	2.55	4.1	0.90
7H-4	20	76.5	7.89	11.10	33.2	563	472	0.98	698	8.9	28.7	91	64	9.8	4.86	2.18	5.7	0.91
9H-3	20	84.3	7.96	9.84	33.4	561	472	0.99	642	9.1	28.1	90	66	9.9	3.85	2.04	5.4	0.86
10H-5	21	95.6	7.88	8.86	33.1	563	478	1.05	688	9.3	26.4	89	72	10.1	2.93	1.84	6.7	0.89
11H-5	22	104.2	7.83	9.89	33.2	564	476	1.00	728	10.9	26.1	94	77	9.1	4.26	1.78	10.9	0.91
12H-5	20.5	114.3	7.63	9.24	33.0	563	476	0.98	784	11.4	25.2	91	79	8.5	3.56	1.87	11.2	0.89
13H-5	22.5	121.7	7.66	9.33	33.4	563	475	0.99	811	12.6	24.5	91	84	8.2	3.73	1.76	16.8	0.92
14H-5	22	129.7	7.59	9.10	33.4	563	476	0.96	785	13.1	23.9	97	88	7.8	3.07	1.71	18.8	0.90
15H-4	21.5	137.5	7.77	9.27	33.1	562	476	0.97	805	13.9	22.8	97	91	7.7	3.26	1.66	20.7	0.90
17H-6	20.5	154.8	7.64	8.13	33.1	565	482	0.96	911	14.9	20.7	95	103	7.4	2.78	1.56	26.4	0.91
18H-4	21.5	161.4	7.74	8.68	33.1	564	479	0.97	831	16.1	20.5	99	106	7.1	2.61	1.55	28.2	0.88
19H-3	20	170.2	7.66	8.22	33.3	564	481	0.99	852	16.7	19.5	98	110	6.4	1.86	1.55	30.7	0.97
20H-4	20	177.8	7.64	6.77	33.2	563	482	1.00	827	16.8	18.7	97	118	6.9	2.15	1.44	27.2	0.90
21H-4	20.5	182.7	7.66	6.96	33.1	564	484	0.97	807	17.3	17.8	101	122	6.6	2.08	1.35	30.4	0.91
25T-2	29	200.9	7.62	4.58	33.0	560	487	0.97	863	17.9	17.6	102	137	6.4	1.36	3.35	24.8	0.91
26X-3	30.5	206.7	7.42	5.16	33.0	561	486	0.97	851	18.7	16.7	114	142	5.8	0.97	2.51	32.6	0.89
27X-3	30.5	212.1	7.83	5.24	33.1	564	488	0.95	765	19.2	16.7	118	146	6.0	1.25	2.74	32.5	0.91
29X-4	31	223.3	7.66	5.11	32.8	564	489	1.01	799	19.9	15.0	119	156	5.7	1.49	1.86	25.9	0.90
31X-4	29	238.1	7.28	3.99	32.8	560	489	0.92	914	20.0	14.7	118	164	4.9	1.20	2.34	34.2	0.89
32X-4	28.5	244.3	7.39	4.03	32.8	560	488	0.94	836	21.1	14.2	121	161	4.8	1.47	2.54	34.7	0.89
33X-3	30.5	248.9	7.55	3.95	32.8	563	491	0.96	714	21.2	13.0	120	166	4.8	1.27	1.75	29.4	0.89
34X-4	34	254.4	7.53	4.09	32.5	556	480	0.83	485	22.6	13.7	128	169	4.0	1.40	2.03	35.8	1.02
36X-5	34	271.0	7.57	1.94	32.5	557	487	0.82	262	23.4	13.4	132	166	3.7	0.83	3.16	25.4	0.87
37X-4	32.5	279.3	7.93	1.83	32.4	551	479	0.79	234	24.5	11.4	136	164	3.3	1.31	1.51	22.0	0.89
38X-3	35	285.3	8.15	1.21	32.5	552	482	0.91	120	24.5	12.8	134	163	3.5	0.78	3.79	16.0	0.87
39X-5	35	297.0	7.71	Invalid	32.1	551	482	0.74	227	25.2	9.7	136	174	2.8	1.26	1.03	29.9	0.90
40X-5	40	306.3	8.06	0.61	32.2	556	490	0.89	103	24.4	8.7	134	169	3.2	0.69	1.30	17.6	0.89
41X-5	38.5	316.4	7.98	Invalid	31.8	546	477	0.79	132	25.9	8.8	135	166	2.7	0.90	1.10	20.0	0.87
42X-4	39	324.0	7.81	1.39	33.5	553	483	0.76	246	26.1	8.0	136	168	2.6	1.29	0.85	38.5	0.87
43X-3	35	331.8	7.82	1.36	31.9	543	473	0.79	208	26.6	9.5	132	153	2.7	1.14	2.62	37.7	0.87
44X-4	38	337.2	7.70	1.03	32.6	555	486	0.81	254	26.0	10.9	130	150	2.9	0.87	3.51	44.2	0.89
45X-3	38.5	342.1	7.82	1.94	32.3	555	484	0.81	304	27.3	9.2	133	150	2.8	0.80	2.49	46.5	0.87
46X-3	39	346.7	7.85	2.01	32.4	554	484	0.84	383	27.4	8.8	131	151	2.8	0.72	2.69	44.9	0.89
48X-3	38	356.5	7.74	1.61	32.2	555	486	0.97	512	27.0	6.6	129	152	2.8	1.36	0.96	40.1	0.87
49X-3	41	361.8	7.72	1.16	32.1	551	483	0.85	490	27.3	6.9	134	149	2.6	1.02	1.23	42.0	0.87
52X-4	37	378.6	7.71	2.09	31.9	548	477	0.70	406	28.2	6.6	142	149	2.2	1.34	0.89	51.5	0.87

ND = not detected.

Table T12 (continued).

Core, section	Whole-round length (cm)	Depth (mbsf)	Ba (μM)	B (μM)	Fe (μM)	V (nM)	Cu (nM)	Zn (nM)	Rb (nM)	Mo (nM)	Cs (nM)	Pb (nM)	U (nM)
333-C0011C-													
1H-2	20	0.6	0.6	480	9.7	44.3	1279	1620	1884	119	4.3	1.5	24.7
1H-4	19.5	1.8	0.6	462	8.5	33.5	1171	2020	1641	108	2.5	0.7	1.2
2H-2	19	4.6	0.6	473	7.7	36.2	214	770	1728	111	3.6	0.5	4.3
2H-5	19.5	7.4	0.5	462	15.8	34.2	1186	1763	1720	73	3.3	0.9	1.8
2H-8	19	10.1	0.6	425	15.2	43.5	865	1591	1757	111	3.5	0.6	7.3
2H-10	20	11.4	0.6	414	2.6	56.0	1510	1180	1864	213	3.7	1.7	6.7
3H-8	20	19.5	0.6	422	13.9	48.6	2631	1454	1486	49	3.0	0.9	3.1
333-C0011D-													
1H-4	20	25.0	0.8	402	2.7	58.9	3024	1056	1604	118	3.1	1.3	5.4
2H-5	20	35.8	0.9	368	7.0	50.8	587	908	1336	27	2.8	0.4	3.7
3H-5	21.5	44.8	1.0	343	16.8	40.3	2194	1427	1364	61	3.2	0.9	1.6
4H-5	20.5	51.9	1.3	331	7.9	48.0	3521	1563	1309	30	3.2	0.5	3.3
5H-5	20	60.7	1.8	301	1.3	49.0	1267	1449	1312	51	3.2	0.4	3.3
6H-4	21.5	68.8	2.4	291	1.3	53.0	1876	961	1286	20	3.7	0.5	3.7
7H-4	20	76.5	3.1	257	1.2	45.9	1437	894	1171	38	3.1	0.9	2.5
9H-3	20	84.3	3.4	238	1.2	56.8	1015	797	1167	64	3.2	2.2	3.7
10H-5	21	95.6	3.8	251	1.3	69.0	2488	1321	1241	113	3.1	6.0	7.2
11H-5	22	104.2	3.8	244	1.7	52.9	1661	1470	1064	29	2.7	3.0	3.8
12H-5	20.5	114.3	3.8	261	1.8	51.8	1742	1584	988	71	2.3	2.3	3.7
13H-5	22.5	121.7	4.0	268	9.9	36.3	2066	1685	929	19	2.2	0.6	1.2
14H-5	22	129.7	4.1	244	2.4	34.2	1727	2307	828	47	2.0	0.8	5.6
15H-4	21.5	137.5	4.6	215	1.7	39.2	168	890	812	73	1.8	3.5	2.3
17H-6	20.5	154.8	5.0	227	1.8	36.0	1701	1998	838	31	1.9	1.8	2.4
18H-4	21.5	161.4	5.3	202	1.8	40.7	2283	2057	771	66	1.8	2.3	3.6
19H-3	20	170.2	5.6	215	1.9	35.8	635	1624	799	42	2.1	1.7	1.4
20H-4	20	177.8	6.1	215	2.1	37.6	1270	1142	808	91	2.4	6.1	8.5
21H-4	20.5	182.7	6.4	203	1.6	34.7	2172	1732	775	67	2.3	3.4	3.0
25T-2	29	200.9	7.0	200	1.5	33.3	4276	1843	783	145	2.8	2.6	5.7
26X-3	30.5	206.7	7.8	245	3.1	30.1	1411	1463	744	86	2.6	1.2	1.7
27X-3	30.5	212.1	8.4	246	0.9	32.9	ND	717	843	93	3.1	3.4	9.7
29X-4	31	223.3	9.1	222	0.9	36.6	1038	1815	781	136	2.9	9.1	2.6
31X-4	29	238.1	9.1	259	7.0	32.6	2369	2644	662	119	2.8	0.9	1.9
32X-4	28.5	244.3	10.0	240	5.6	32.0	2107	1746	676	152	3.1	0.8	1.6
33X-3	30.5	248.9	10.8	207	ND	31.5	654	732	703	161	3.6	1.5	3.3
34X-4	34	254.4	11.3	223	ND	30.1	3760	5071	507	125	2.4	2.2	3.3
36X-5	34	271.0	13.1	201	ND	30.7	1632	2445	454	183	2.0	3.4	2.3
37X-4	32.5	279.3	17.3	178	ND	28.6	554	287	380	156	1.8	2.4	6.3
38X-3	35	285.3	14.5	161	ND	32.8	628	1494	437	243	2.1	1.8	2.3
39X-5	35	297.0	27.4	280	ND	25.7	1949	1853	298	125	1.4	1.0	1.2
40X-5	40	306.3	30.4	202	ND	25.4	1177	396	400	184	1.9	1.0	0.3
41X-5	38.5	316.4	45.8	234	ND	25.6	892	476	314	139	1.3	1.4	1.4
42X-4	39	324.0	62.6	341	ND	23.6	967	639	346	104	1.6	1.1	2.4
43X-3	35	331.8	40.0	267	0.8	27.8	2465	1135	382	152	1.8	1.7	2.8
44X-4	38	337.2	30.2	288	ND	25.5	3140	607	459	118	2.4	1.2	1.7
45X-3	38.5	342.1	45.9	274	ND	27.4	2543	491	457	77	2.7	2.6	5.8
46X-3	39	346.7	39.6	281	ND	23.3	834	196	565	84	4.2	1.0	5.2
48X-3	38	356.5	85.8	300	0.8	29.2	2092	271	541	180	3.7	1.5	1.8
49X-3	41	361.8	86.9	308	ND	28.5	2717	812	466	95	2.6	2.1	1.7
52X-4	37	378.6	95.8	372	ND	23.3	1196	628	336	75	2.1	2.1	5.1

Table T13. Interstitial water geochemistry (corrected data), Holes C0011C and C0011D.

Core, section	Whole-round length (cm)	Depth (mbsf)	pH	Alkalinity (mM)	Salinity	Chlorinity (mM)	Na^+ (mM)	NH_4^+ (mM)	Si (µM)	Ca^{2+} (mM)	Mg^{2+} (mM)	Sr (µM)	Li (µM)	K^+ (mM)	PO_4^{3-} (µM)	SO_4^{2-} (mM)	Mn (µM)	Br^- (mM)	Ba (µM)	B (µM)	Fe (µM)
333-C0011C-																					
1H-2	20	0.6	7.54	2.93	35.6	553	263	0.02	465	10.8	52.3	82	42	12.6	6.19	28.09	4.2	0.83	0.6	480	9.7
1H-4	19.5	1.8	7.43	3.64	35.4	551	323	0.05	513	10.7	51.6	81	39	12.2	6.91	27.41	9.6	0.83	0.6	462	8.5
2H-2	19	4.6	7.49	4.22	35.3	556	435	0.13	652	10.3	50.0	85	36	12.7	6.08	24.90	13.6	0.85	0.6	473	7.7
2H-5	19.5	7.4	7.36	4.89	35.3	555	434	0.20	629	10.2	48.9	84	35	12.6	8.29	23.09	15.8	0.88	0.5	462	15.8
2H-8	19	10.1	7.40	5.16	35.1	556	444	0.26	627	9.9	48.0	82	35	12.7	8.51	21.47	15.4	0.84	0.6	425	15.2
2H-10	21	11.4	7.71	4.96	35.1	559	471	0.30	616	9.2	45.3	80	40	13.5	8.02	20.63	14.6	0.85	0.6	414	2.6
3H-8	21	19.5	7.79	6.70	34.8	563	475	0.43	677	8.9	42.8	82	38	11.3	9.81	16.17	16.0	0.86	0.6	422	13.9
333-C0011D-																					
1H-4	20	25.0	7.71	7.17	34.5	564	473	0.53	786	8.4	40.6	81	42	12.7	9.96	13.50	12.0	0.87	0.8	402	2.7
2H-5	20	35.8	7.59	8.94	34.1	563	468	0.66	728	8.4	38.2	85	45	11.2	12.48	9.52	11.0	0.86	0.9	368	7.0
3H-5	21.5	44.8	7.58	9.67	33.9	564	469	0.76	683	8.3	35.7	87	48	10.6	11.16	6.91	9.7	0.89	1.0	343	16.8
4H-5	20.5	51.9	7.69	9.54	33.4	564	473	0.84	728	7.7	32.8	86	55	10.5	7.39	5.08	6.6	0.91	1.3	331	7.9
5H-5	20	60.7	7.75	9.77	33.4	564	475	0.92	715	7.7	30.9	85	59	10.4	5.67	3.56	4.7	0.90	1.8	301	1.3
6H-4	21.5	68.8	7.75	9.74	33.2	563	473	0.97	715	7.8	29.9	87	62	10.2	4.66	2.55	4.1	0.90	2.4	291	1.3
7H-4	20	76.5	7.89	11.10	33.2	563	472	0.98	698	8.9	28.7	91	64	9.8	4.86	2.18	5.7	0.91	3.1	257	1.2
9H-3	20	84.3	7.96	9.84	33.4	561	472	0.99	642	9.1	28.1	90	66	9.9	3.85	2.04	5.4	0.86	3.4	238	1.2
10H-5	21	95.6	7.88	8.86	33.1	563	478	1.05	688	9.3	26.4	89	72	10.1	2.93	1.84	6.7	0.89	3.8	251	1.3
11H-5	22	104.2	7.83	9.89	33.2	564	476	1.00	728	10.9	26.1	94	77	9.1	4.26	1.78	10.9	0.91	3.8	244	1.7
12H-5	20.5	114.3	7.63	9.24	33.0	563	476	0.98	784	11.4	25.2	91	79	8.5	3.56	1.87	11.2	0.89	3.8	261	1.8
13H-5	22.5	121.7	7.66	9.33	33.4	563	475	0.99	811	12.6	24.5	91	84	8.2	3.73	1.76	16.8	0.92	4.0	268	9.9
14H-5	22	129.7	7.59	9.10	33.4	563	476	0.96	785	13.1	23.9	97	88	7.8	3.07	1.71	18.8	0.90	4.1	244	2.4
15H-4	21.5	137.5	7.77	9.27	33.1	562	476	0.97	805	13.9	22.8	97	91	7.7	3.26	1.66	20.7	0.90	4.6	215	1.7
17H-6	20.5	154.8	7.64	8.13	33.1	565	482	0.96	911	14.9	20.7	95	103	7.4	2.78	1.56	26.4	0.91	5.0	227	1.8
18H-4	21.5	161.4	7.74	8.68	33.1	564	479	0.97	831	16.1	20.5	99	106	7.1	2.61	1.55	28.2	0.88	5.3	202	1.8
19H-3	20	170.2	7.66	8.22	33.3	564	481	0.99	852	16.7	19.5	98	110	6.4	1.86	1.55	30.7	0.97	5.6	215	1.9
20H-4	20	177.8	7.64	6.77	33.2	563	482	1.00	827	16.8	18.7	97	118	6.9	2.15	1.44	27.2	0.90	6.1	215	2.1
21H-4	20.5	182.7	7.66	6.96	33.1	564	484	0.97	807	17.3	17.8	101	122	6.6	2.08	1.35	30.4	0.91	6.4	203	1.6
25T-2	29	200.9	7.62	4.88	32.8	561	487	0.97	955	18.9	12.7	103	152	5.8	1.14	3.35	28.0	0.92	8.0	171	1.5
26X-3	30.5	206.7	7.42	5.43	32.8	562	486	0.97	916	19.5	13.1	117	153	5.3	0.78	2.51	35.6	0.90	8.5	229	3.1
27X-3	30.5	212.1	7.83	5.55	32.9	564	488	0.95	828	20.1	12.7	121	159	5.5	1.06	2.74	35.9	0.92	9.3	228	0.9
29X-4	31	223.3	7.66	5.30	32.7	565	489	1.01	842	20.6	12.3	121	165	5.3	1.39	1.86	27.6	0.91	9.7	208	0.9
31X-4	29	238.1	7.28	4.14	32.6	561	489	0.92	980	20.8	11.2	120	176	4.4	1.05	2.34	37.2	0.89	9.9	246	7.0
32X-4	28.5	244.3	7.39	4.19	32.6	561	488	0.94	901	22.1	10.3	123	174	4.2	1.32	2.54	38.0	0.90	11.0	223	5.6
33X-3	30.5	248.9	7.55	4.06	32.6	563	491	0.96	750	21.9	10.4	122	175	4.4	1.16	1.75	31.3	0.90	11.4	193	ND
34X-4	34	254.4	7.53	4.23	32.3	555	480	0.83	510	23.5	10.6	131	180	3.6	1.28	2.03	38.5	1.03	12.1	208	ND
36X-5	34	271.0	7.57	1.90	32.2	557	487	0.82	275	25.0	8.3	137	183	2.9	0.56	3.16	28.6	0.88	14.6	174	ND
37X-4	32.5	279.3	7.93	1.80	32.3	551	479	0.79	238	25.2	9.0	138	171	2.9	1.22	1.51	23.2	0.89	18.3	165	ND
38X-3	35	285.3	8.15	1.04	32.1	551	482	0.91	113	26.6	6.5	141	184	2.5	0.44	3.79	18.4	0.88	16.6	123	ND
39X-5	35	297.0	7.71	NA	32.0	551	482	0.74	229	25.7	8.1	138	180	2.5	1.20	1.03	31.0	0.90	28.4	275	ND
40X-5	40	306.3	8.06	0.53	32.1	556	490	0.89	101	25.1	6.6	137	176	2.9	0.58	1.30	18.5	0.89	31.8	191	ND
41X-5	38.5	316.4	7.98	NA	31.7	545	477	0.79	131	26.5	7.0	137	172	2.4	0.81	1.10	20.8	0.87	47.6	226	ND
42X-4	39	324.0	7.81	1.36	33.5	552	483	0.76	248	26.6	6.6	138	173	2.3	1.24	0.85	39.6	0.88	64.5	339	ND
43X-3	35	331.8	7.82	1.26	31.6	542	473	0.79	213	28.2	5.0	137	165	1.9	0.96	2.62	41.4	0.88	43.9	253	0.8
44X-4	38	337.2	7.70	0.85	32.2	554	486	0.81	267	28.2	4.9	136	167	1.8	0.58	3.51	50.3	0.90	34.3	270	ND
45X-3	38.5	342.1	7.82	1.90	32.0	554	484	0.81	317	28.9	5.0	137	162	2.1	0.59	2.49	50.9	0.88	50.2	261	ND
46X-3	39	346.7	7.85	1.98	32.2	554	484	0.84	406	29.1	4.1	135	163	2.0	0.48	2.69	49.5	0.90	43.7	267	ND
48X-3	38	356.5	7.74	1.59	32.1	554	486	0.97	524	27.6	4.9	130	156	2.5	1.30	0.96	41.5	0.87	88.7	296	0.8
49X-3	41	361.8	7.72	1.11	32.0	551	483	0.85	504	28.0	4.8	136	154	2.2	0.93	1.23	43.9	0.87	90.7	303	ND
52X-4	37	378.6	7.71	2.09	31.9	547	477	0.70	414	28.7	5.1	144	153	1.9	1.29	0.89	53.1	0.88	98.8	371	ND

NA = not applicable, ND = not determined.

Table T14. Headspace methane concentration, Holes C0011C and C0011D.

Core, section, interval (cm)	Depth (mbsf)	Methane (ppmv)
333-C0011C-		
1H-1, 58.5–62.5	0.6	0.0
2H-1, 114–118	4.6	0.0
3H-1, 137–141	14.4	2.8
333-C0011D-		
1H-1, 137–141	22.4	3.0
2H-1, 135.5–139.5	31.9	3.0
3H-1, 137.5–141.5	41.4	2.8
4H-1, 137.5–141.5	50.4	2.7
5H-1, 136.5–141.5	56.9	0.0
6H-1, 137.5–141.5	66.4	0.0
7H-1, 135.5–139.5	75.9	0.0
8H-1, 137–141	80.4	0.0
9H-1, 136–141	82.9	0.0
10H-1, 134–138	91.8	2.8
11H-1, 138–142	101.4	2.7
12H-1, 132.5–136.5	110.8	2.7
13H-1, 138.5–142.5	120.4	2.6
14H-1, 136.5–140.5	126.4	2.6
15H-1, 138–142	134.9	2.8
16H-1, 126.5–130.5	144.3	0.0
17H-1, 139–143	151.4	0.0
18H-2, 136.5–140.5	160.1	0.0
19H-1, 136.5–140.5	169.4	2.9
20H-2, 138–142	176.8	0.0
21H-1, 136–140	181.9	2.9
22H-1, 136–140	185.9	2.6
23T-1, 136.5–140.5	187.4	2.6
24T-1, 87.5–91.5	196.4	0.0
25T-1, 81.5–85.5	200.8	0.0
26X-1, 137–141	206.4	0.0
27X-1, 136.5–140.5	211.4	2.5
28X-1, 137.5–141.5	216.4	0.0
29X-1, 136.5–140.5	221.4	2.8
30X-2, 118.5–122.5	227.6	3.3
31X-1, 134.5–138.5	235.8	0.0
32X-1, 136.5–140.5	242.9	2.7
33X-1, 134.5–138.5	247.8	3.1
34X-1, 136.5–140.5	252.9	5.5
36X-1, 136.5–140.5	267.4	37.0
37X-1, 134–138	276.8	83.8
38X-1, 137–141	283.9	72.5
39X-1, 136–140	293.4	93.9
40X-1, 136.5–140.5	302.9	127.1
41X-1, 131–135	312.3	138.4
42X-1, 136.5–140.5	321.4	145.8
43X-1, 134–138	330.8	463.7
44X-1, 137–141	335.9	366.1
45X-1, 136.5–140.5	340.9	230.6
46X-1, 136–140	345.9	391.3
47X-1, 134–138	350.8	314.1
48X-1, 135–139	355.9	693.5
49X-1, 135–139	360.9	288.5
50X-1, 136–140	366.4	635.1
51X-1, 133–137	371.3	299.5
52X-1, 135.5–139.5	376.4	873.6

Methane is set to 0.0 when below detection.

Table T15. Bulk sediment calcium carbonate and elemental analyses data, Holes C0011C and C0011D. (Continued on next two pages.)

Core, section, interval (cm)	Depth (mbsf)	$CaCO_3$ (wt%)	TOC (wt%)	TN (wt%)	TOC/TN_{at}	TS (wt%)
333-C0011C-						
1H-2, 20–22	0.8	2.37	0.47	0.05	9.2	0.06
1H-4, 20–22	2.0	8.23	0.22	0.04	5.7	0.06
1H-5, 108.5–110.5	3.1	17.66	0.42	0.05	8.0	0.04
2H-2, 19–21	4.8	3.89	0.32	0.05	6.8	0.09
2H-5, 20–22	7.6	7.03	0.32	0.05	7.0	0.08
2H-8, 19–20	10.3	10.29	0.36	0.05	7.9	0.10
2H-9, 8–9	10.4	7.18	0.40	0.05	7.6	0.04
2H-10, 20–22	11.6	9.18	0.43	0.05	8.0	0.05
333-C0011D-						
3H-1, 47–48	13.5	5.61	0.28	0.03	10.5	0.07
3H-8, 20–22	19.7	7.80	0.43	0.06	7.7	0.07
3H-9, 20–21	19.9	13.33	0.38	0.05	7.0	0.07
1H-3, 15–16	23.8	14.57	0.47	0.06	7.6	0.06
1H-4, 20–22	25.2	2.88	0.38	0.05	7.1	0.04
2H-2, 121–122	33.1	0.69	0.10	0.02	6.5	0.20
2H-5, 20–22	36.0	4.15	0.31	0.05	5.8	0.09
2H-7, 20–21	36.4	12.12	0.37	0.05	7.6	0.06
3H-3, 121–122	43.9	8.94	0.30	0.05	6.0	0.07
3H-5, 22–24	45.0	0.55	0.05	0.01	5.1	0.10
3H-8, 43–44	48.2	16.25	0.52	0.06	8.1	0.06
4H-1, 59–60	49.6	2.60	0.28	0.05	5.9	0.11
4H-2, 121–122	51.3	11.00	0.32	0.05	6.4	0.04
4H-3, 46–47	51.7	0.34	0.29	0.05	6.1	0.08
4H-5, 21–23	52.1	6.62	0.26	0.04	6.1	0.06
5H-3, 125–126	59.4	2.01	0.33	0.05	6.1	0.06
5H-5, 20–22	60.9	6.43	0.35	0.05	6.7	0.04
5H-7, 120–121	63.5	8.24	0.31	0.05	6.0	0.05
6H-3, 20–21	67.9	13.10	0.36	0.05	8.1	0.03
6H-4, 22–24	69.0	10.66	0.24	0.04	5.8	0.08
6H-5, 124–125	70.3	6.13	0.33	0.05	6.2	0.04
7H-2, 125–126	76.4	3.33	0.38	0.06	6.8	0.04
7H-4, 20–22	76.7	1.02	0.26	0.05	5.7	0.03
7H-5, 20–21	76.8	1.44	0.28	0.05	5.8	0.06
9H-3, 20–22	84.5	0.80	0.35	0.06	5.9	0.22
9H-4, 34–35	84.8	0.38	0.37	0.06	6.2	0.97
9H-6, 33–34	87.1	2.36	0.28	0.05	5.3	0.07
10H-1, 68–69	91.2	5.10	0.27	0.05	5.6	0.28
10H-5, 21–23	95.8	1.76	0.35	0.06	6.3	0.21
10H-7, 8–9	97.2	0.91	0.42	0.06	7.1	0.14
10H-7, 44–45	97.6	1.15	0.45	0.07	6.8	0.19
11H-3, 105–106	103.8	0.35	0.44	0.07	6.7	0.30
11H-5, 22–24	104.4	0.85	0.39	0.06	6.5	0.34
11H-6, 121–122	105.6	1.41	0.37	0.06	5.8	0.13
12H-2, 125–126	112.1	8.66	0.47	0.06	7.3	0.16
12H-5, 21–23	114.5	1.14	0.34	0.06	6.1	0.27
12H-8, 20–21	114.7	3.82	0.44	0.06	6.8	0.20
13H-2, 125–126	121.1	4.59	0.36	0.06	6.1	0.13
13H-3, 85–86	121.5	13.31	0.44	0.05	8.1	0.14
13H-5, 23–25	121.9	0.70	0.25	0.05	5.4	0.10
14H-3, 15–16	127.6	4.01	0.31	0.05	6.0	0.12
14H-5, 22–24	129.9	0.79	0.40	0.06	6.1	0.13
14H-7, 60–61	131.8	5.57	0.45	0.07	6.8	0.16
15H-4, 22–24	137.7	3.15	0.38	0.06	6.0	0.17
15H-5, 105–106	138.8	3.12	0.28	0.05	5.3	0.22
15H-7, 126–127	141.7	1.17	0.30	0.05	5.5	0.11
15H-8, 63–64	142.4	1.22	0.34	0.06	5.7	0.26
16H-4, 52–54	146.0	6.60	0.29	0.05	5.4	0.09
16H-6, 99–101	148.6	6.32	0.09	0.02	4.2	0.16
17H-5, 20–21	153.8	3.47	0.43	0.07	6.2	0.12
17H-6, 21–23	155.0	2.40	0.35	0.06	5.9	0.14
17H-7, 88–89	155.9	0.35	0.43	0.07	6.4	0.18
18H-4, 22–24	161.6	1.08	0.38	0.07	5.7	0.18
18H-6, 126–127	164.2	1.52	0.39	0.06	6.3	0.24
18H-9, 20–21	167.2	3.44	0.39	0.06	6.1	0.13
19H-3, 20–22	170.4	2.16	0.37	0.06	5.9	0.16
19H-4, 127–128	171.7	4.29	0.36	0.06	6.0	0.29

Table T15 (continued). (Continued on next page.)

Core, section, interval (cm)	Depth (mbsf)	$CaCO_3$ (wt%)	TOC (wt%)	TN (wt%)	TOC/TN_{at}	TS (wt%)
19H-5, 119–120	172.7	2.47	0.34	0.06	5.4	0.31
20H-3, 20–21	176.9	2.45	0.29	0.06	5.1	0.16
20H-4, 20–22	178.0	3.50	0.35	0.06	5.8	0.14
21H-2, 120–121	182.7	0.86	0.43	0.07	6.1	0.10
21H-4, 21–23	182.9	1.10	0.35	0.06	5.6	0.26
21H-5, 70–71	183.1	1.40	0.37	0.07	5.7	0.27
21H-5, 70–71	183.6	1.60	0.35	0.06	5.7	0.19
22H-1, 54–56	185.0	1.19	0.29	0.06	4.6	0.12
23T-2, 69–71	188.1	2.47	0.30	0.06	5.0	0.17
24T-1, 39–40	195.9	1.89	0.33	0.06	5.4	0.22
25T-2, 29–31	201.1	1.76	0.38	0.07	5.7	0.22
25T-4, 61–62	203.2	2.94	0.33	0.06	5.4	0.30
26X-1, 56–57	205.6	0.89	0.35	0.07	5.3	0.24
26X-1, 92–93	205.9	2.30	0.24	0.04	5.7	0.17
26X-1, 134–135	206.3	2.61	0.35	0.06	5.4	0.19
26X-3, 31–33	207.0	4.51	0.33	0.06	5.4	0.20
26X-6, 27–28	208.7	1.18	0.37	0.07	5.5	0.33
27X-3, 31–33	212.4	1.31	0.34	0.06	5.5	0.14
27X-4, 62–63	213.0	1.13	0.34	0.06	5.5	0.25
27X-6, 21–22	214.5	1.72	0.37	0.06	6.0	0.09
28X-1, 97–98	216.0	8.48	0.21	0.05	4.0	0.35
28X-2, 17–18	216.5	6.75	0.22	0.05	4.3	0.12
29X-1, 46–47	220.5	4.15	0.28	0.06	4.7	0.26
29X-3, 25–26	222.6	2.54	0.38	0.06	6.5	0.18
29X-4, 31–33	223.6	3.90	0.29	0.05	5.3	0.35
30X-1, 85–87	225.9	1.38	0.29	0.05	5.6	0.09
31X-4, 29–31	238.4	9.12	0.27	0.07	3.8	11.86
31X-5, 47–48	238.9	13.92	0.23	0.04	5.3	0.27
31X-5, 76–77	239.2	7.54	0.21	0.05	4.4	0.04
32X-4, 29–31	244.6	6.49	0.25	0.05	4.7	0.87
32X-5, 82–83	245.4	3.92	0.24	0.05	4.6	0.06
32X-6, 23–24	246.0	3.68	0.26	0.06	4.6	0.06
33X-3, 31–33	249.2	2.12	0.17	0.04	4.2	0.07
33X-4, 37–38	249.5	2.89	0.26	0.06	4.4	0.05
33X-5, 58–59	251.1	17.11	0.14	0.04	3.4	0.54
34X-2, 76–77	253.2	24.51	0.19	0.04	5.1	0.02
34X-4, 34–36	254.8	3.78	0.21	0.05	3.9	0.02
34X-5, 60–61	255.3	1.35	0.26	0.06	4.3	0.04
34X-6, 45–46	256.1	14.61	0.20	0.05	4.1	0.06
36X-2, 55–56	267.9	4.37	0.26	0.05	4.8	0.06
36X-2, 110–111	268.4	10.92	0.22	0.05	4.4	0.23
36X-5, 34–36	271.3	7.57	0.26	0.06	4.4	0.07
36X-8, 55–56	274.5	2.44	0.27	0.06	4.7	0.06
37X-1, 111–112	276.6	4.98	0.21	0.05	3.9	0.04
37X-3, 50–51	278.6	0.98	0.28	0.06	4.5	0.07
37X-4, 33–35	279.7	2.98	0.24	0.06	4.2	0.06
38X-2, 98–99	284.9	1.73	0.31	0.06	4.9	0.12
38X-3, 35–37	285.7	1.14	0.23	0.06	4.0	0.06
38X-5, 38–39	286.7	1.89	0.27	0.06	4.4	0.04
39X-1, 126–127	293.3	1.31	0.28	0.06	4.5	0.07
39X-5, 35–37	297.4	4.63	0.21	0.06	3.7	0.06
39X-7, 124–125	300.0	1.91	0.29	0.06	4.8	0.28
39X-8, 22–23	300.3	3.94	0.30	0.06	5.0	0.19
40X-1, 40–41	301.9	11.59	0.23	0.05	4.7	0.12
40X-2, 125–126	304.1	8.40	0.24	0.05	4.6	0.12
40X-3, 72–73	304.9	17.36	0.16	0.05	3.6	0.05
40X-5, 40–42	306.7	6.07	0.21	0.05	4.1	0.12
41X-3, 32–33	314.1	11.73	0.19	0.05	3.8	0.06
41X-4, 106–107	316.2	10.84	0.25	0.05	4.7	0.14
41X-5, 39–41	316.8	2.51	0.17	0.06	3.1	0.18
41X-6, 120–121	318.0	7.50	0.26	0.05	4.8	0.15
41X-7, 43–44	318.6	5.19	0.28	0.06	4.6	0.09
42X-6, 36–38	321.7	3.10	0.30	0.06	4.8	0.20
43X-1, 33–34	329.8	2.14	0.20	0.06	3.4	0.11
43X-3, 36–38	332.2	1.22	0.26	0.06	4.0	0.21
44X-1, 25–26	334.8	2.42	0.25	0.06	3.9	0.09
44X-1, 105–106	335.6	1.36	0.26	0.06	4.3	0.12
44X-4, 38–40	337.6	3.70	0.27	0.06	4.2	0.19
45X-1, 128–129	340.8	1.84	0.30	0.06	4.7	0.12

Table T15 (continued).

Core, section, interval (cm)	Depth (mbsf)	$CaCO_3$ (wt%)	TOC (wt%)	TN (wt%)	TOC/TN_{at}	TS (wt%)
45X-3, 39–41	342.5	1.25	0.42	0.07	5.7	0.39
45X-5, 13–14	343.5	1.94	0.31	0.07	4.5	0.12
45X-5, 45–46	343.8	0.75	0.28	0.06	4.6	0.24
46X-3, 39–41	347.1	0.81	0.33	0.07	4.6	0.16
47X-4, 50–52	352.1	3.87	0.37	0.07	5.5	0.20
47X-6, 115–117	353.5	0.97	0.15	0.02	6.2	0.23
48X-2, 93–94	356.6	0.94	0.20	0.05	4.5	0.14
48X-3, 38–40	356.9	2.18	0.26	0.06	4.2	0.04
49X-1, 93–95	360.4	1.74	0.35	0.06	5.4	0.28
49X-3, 41–43	362.2	1.97	0.33	0.06	5.1	0.18
49X-4, 50–51	362.7	0.25	0.53	0.07	7.9	0.11
49X-4, 71–72	362.9	1.56	0.11	0.06	1.9	0.17
49X-4, 120–121	363.4	0.72	0.28	0.06	4.4	0.10
49X-5, 59–60	363.9	1.75	0.31	0.04	8.3	0.28
50X-4, 56–58	371.9	0.64	0.09	0.02	5.4	0.11
51X-2, 81–82	377.2	1.25	0.06	0.01	5.2	0.10
52X-3, 56–57	378.4	2.20	0.28	0.06	5.0	0.05
52X-4, 37–39	378.9	4.91	0.56	0.08	7.2	0.26

TOC = total organic carbon, TN = total nitrogen, TS = total sulfur.

Table T16. Rock-Eval pyrolysis data, Holes C0011C and C0011D.

Core, section, interval (cm)	Depth (mbsf)	S1 (mg HC/g sediment)	S2 (mg HC/g sediment)	T_{max} (°C)	Hydrogen index (mg HC/g TOC)	Production index
333-C0011C-						
1H-2, 20–22	0.8	0.08	0.14	336	30	0.36
1H-5, 108.5–110.5	3.2	0.03	0.16	380	39	0.18
333-C0011D-						
1H-3, 15–16	24.0	0.03	0.14	397	31	0.15
3H-8, 43–44	48.6	0.02	0.29	398	62	0.07
7H-2, 125–126	77.2	0.01	0.11	323	28	0.09
12H-8, 20–21	117.8	0.06	0.13	400	28	0.33
14H-7, 60–61	132.7	0.04	0.19	399	41	0.17
17H-5, 20–21	154.5	0.04	0.15	409	32	0.21
20H-4, 20–22	178.2	0.07	0.20	366	57	0.25
31X-5, 76–77	239.2	0.01	0.03	406	14	0.3
34X-6, 45–46	256.1	0.00	0.04	382	20	0.06
44X-4, 38–40	337.6	0.00	0.05	410	19	0.01
45X-3, 38.5–40.5	342.7	0.03	0.17	401	39	0.14
49X-3, 41–43	362.8	0.02	0.08	414	26	0.19
52X-4, 37–39	378.9	0.01	0.21	411	38	0.06

HC = hydrocarbon, TOC = total organic carbon.